MARINE TECHNOLOGY COMPETENCE CENTER

KURESSAARE COLLEGE

TAL TECH

NUMERICAL ASSESSMENT OF BOTTOM CONTACT OF MV ESTONIA

Tallinn, 2023

Main authors

K. Tabri

Tallinn University of Technology, School of Engineering, Marine Technology Competence Center MARTE, Estonia

M. Heinvee

MEC Insenerilahendused, Estonia

Contributing project partners

H. Naar, A. Šults

Tallinn University of Technology, School of Engineering, Marine Technology Competence Center MARTE, Estonia

M. Mäesalu

MEC Insenerilahendused, Estonia

S. Varushkin, M. Kaldoja

Foreship, Estonia

Consulting external partners

J. Matusiak

Aalto University Professor Emeritus, Finland

M. Jakobsson, M. O'Regan

Stockholm University, Department of Geological Sciences

Client:

Estonian Safety Investigation Bureau

Tartu mnt. 85, 10115, Tallinn

Telephone: +372 625 6314

E-post: info@ojk.ee

Contract no.:

1.9-8/22-457-1 (30.08.2022)

Revision no.:

Rev. 1.

Revision history:

Rev. 0 (31.08.2023) is initial revision.
Rev. 1 (20.09.2023) includes minor revisions.

TABLE OF CONTENT

1. INTRODUCTION

This report describes the numerical assessment of the bottom contact of MV Estonia- a passenger ferry that sank on 28th of September 1994. While extensive investigation was conducted in 1994-1997, recent underwater surveys have revealed damages of the hull in form of at least two openings and an indented area of the vessel midship. A new investigation has been started by accident investigation authorities of Estonia, Sweden and Finland to study the cause of these hull damages and to provide additional information for the accident.

The report presents a part of the new investigation and describes the simulations conducted with the aim to explain whether the new reported damage openings can be due to the bottom contact.

The initial flooding of the vessel, list development and the capsizing of the vessel are not in the scope of this assessment. Here, the assessment starts from a condition, where the ship aft is in immediate vicinity of the sea bottom, see Figure 1. The subsequent ship motions are dominated by angular motion as the ship falls towards the sea bottom. The report focuses on the simulation of the angular motions and on the contact description between the ship and the sea bottom.

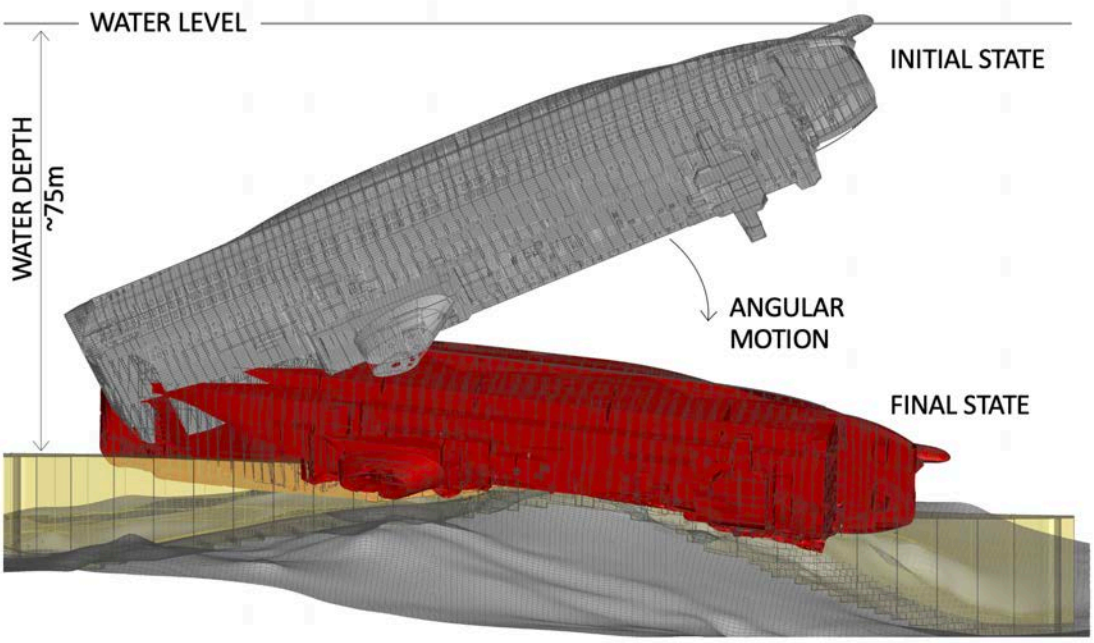

Figure 1. Scope of the simulations.

Report addresses several challenges in simulating the ship grounding to a deformable sea bottom at water depth of about 80 meters:

1. Establishing the initial conditions of the ship (position, orientation and loading conditions). The initial conditions for the analysis are constructed based on the earlier foundering simulations conducted during the so-called Vinnova study (Krüger, 2007, 2008; Jasinowski and Vassalos, 2008).
2. Simulation of the sinking dynamics of the ship- contemporary flooding calculators do not focus on the situations, where the whole ship is already under the water. An approach based on computational fluid dynamics (CFD) is too time consuming for practical applications. Thus, a simplified approach is proposed, that allows to evaluate sinking dynamics of a fully underwater ship. The aim of this model is to evaluate the angular velocity of the ship descending towards the sea bottom.

3. Simulation of the seabed geology and behaviour. The seabed under the ship consists of rigid bedrock and of deformable bottom (till, glacial clay and silt, and soft postglacial clay/muds). Soft sediment covers the bedrock and, in some regions, the sediment is compressed several meters before the ship becomes to contact with the rigid bedrock. A numerical approach based on Multi-Material Arbitrary Lagrangian Eulerian (MMALE) approach is developed to model the sediment behaviour and the contact between the ship.
4. Detailed numerical simulation, where fully modelled deformable ship protrudes into MMALE mesh and becomes to contact with the rigid bedrock. This approach uses the input angular velocity from the simplified approach to approximate the contact dynamics.

Report describes the models and presents the outcomes of the simulations. The simulation results in a form of ship position and structural deformations are compared to the known position of the ship and to its structural damages.

Report also addresses the buckling of ship bottom plating discovered from the photogrammetric data of the shipwreck.

2. CONCEPT FOR THE ASSESSMENT

Assessment is divided into three stages that establish the initial conditions and the simulation models (Figure 2):

S1. Initial conditions

First stage of the sinking, where the ship is filled with water through the open bow ramp is out of the scope of the current assessment and thus, not simulated. Here, the assessment starts from the final position of the vessel as established in VINNOVA study [1]. The VINNOVA study defined the ship loading condition and position until the instant, where the aft of the ship was in the vicinity of the sea bottom while the small part of the ship bow is still above the sea surface. This data is used to construct the initial conditions for this analysis (Chapter 3). The uncertainties in the input data are discussed in Chapter 4.

S2. Sinking simulations using simplified model

A simplified model is proposed to simulate the ship motions from the initial position until the full contact with the sea bottom (Chapter 5). Ship motions are limited to single degree of freedom angular motion. Ship mass, centre of gravity (COG), centre of buoyancy (COB) and the forces that act are described as precisely as the available information and the level of simplicity allows. The main outcome of the simulations with simplified model is the angular velocity of the ship, when it is approaching towards the sea bottom. This model considers the influence of the inertial and hydromechanical forces acting at the vessel.

S3. Detailed numerical simulations

For detailed bottom contact assessment, the ship and the sea bottom are modelled, and dynamic numerical simulations are conducted (Chapter 6). The ship and the rigid sea bottom are modelled using Lagrangian model while the soft deformable bottom is modelled using Multi-Material Arbitrary Lagrangian Eulerian (MMALE) approach. The hydromechanics loads acting at the ship are not directly included in the simulation and the simulations are conducted under the angular velocity as evaluated with the simplified model S2 defined in the stage 2. The outcomes of the dynamic simulations are compared to the current position and reported damages of the shipwreck of MS Estonia (Chapter 7)

In addition, the buckling dent discover at the flat bottom of the shipwreck is studied and the process leading to the buckling damage is described (Chapter 8).

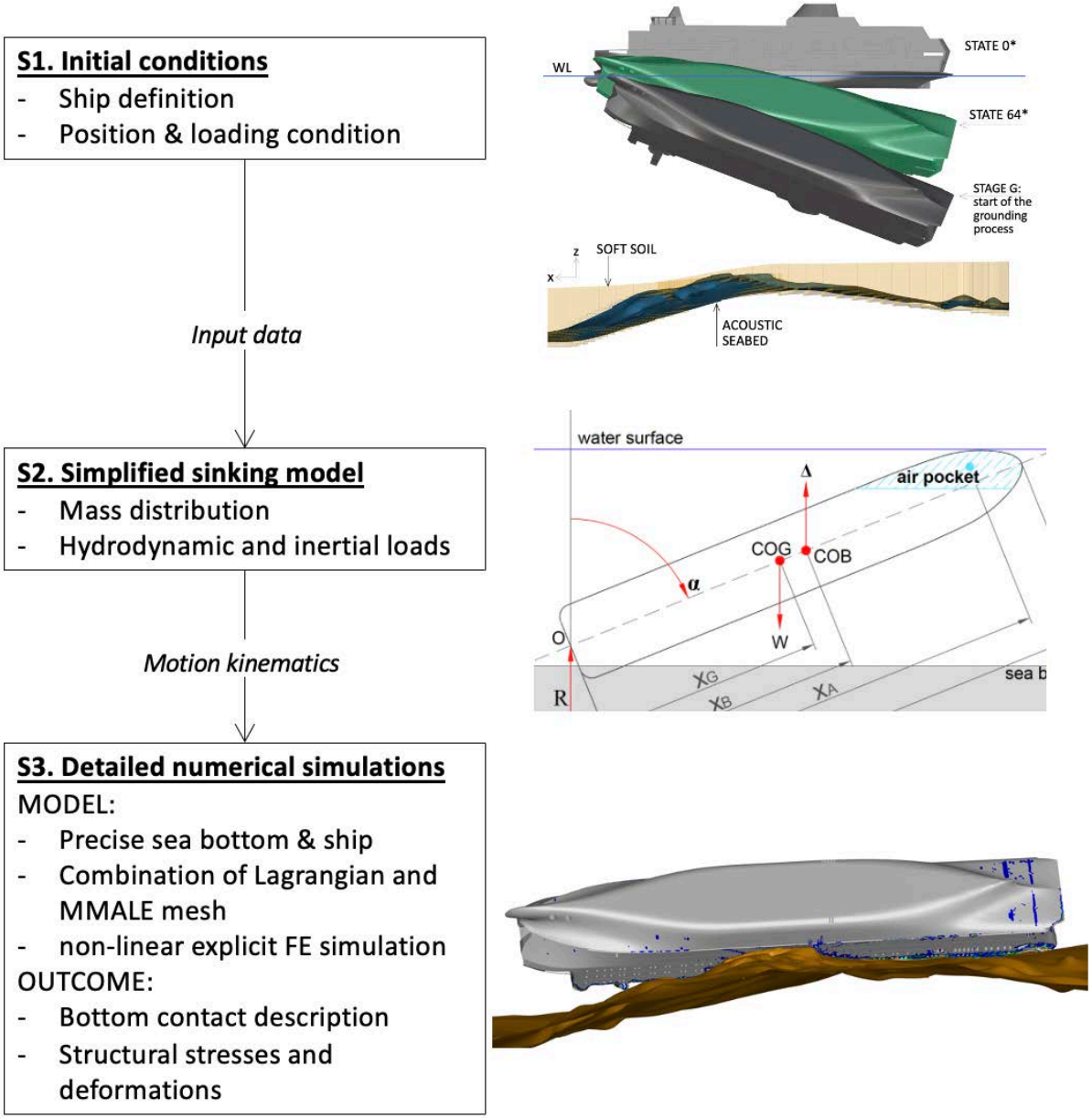

Figure 2. Concept for the assessment.

3. INITIAL CONDITIONS

For the numerical contact assessment the ship motion dynamics prior the bottom contact are of interest. The initial water inflow and the full foundering process is not simulated and the findings from earlier studies are used to construct the initial conditions. The initial conditions are defined in means of ship loading condition, position, and orientation.

The main particulars of MV Estonia are given in Table 1. The lightship mass excludes the mass of the bow visor. Water density 1004 kg/m^3 is assumed.

Table 1. MV Estonia, ship particulars (Krüger, 2008), (Kehren, 2009).

LPP	137.4 m
LOA	155.4 m
B	24.2 m
Draught mean	5.39 m
Trim	0.435 m to aft
GM	1.17 m
KG	10.62 m
Displacement at surface	11 930 m3
Lightship mass*	9 673 t
Deadweight**	2 306 t

* Lightship mass excludes the mass of the bow visor of 60 tonne (Kehren, 2009)
** From (Kehren, 2009)

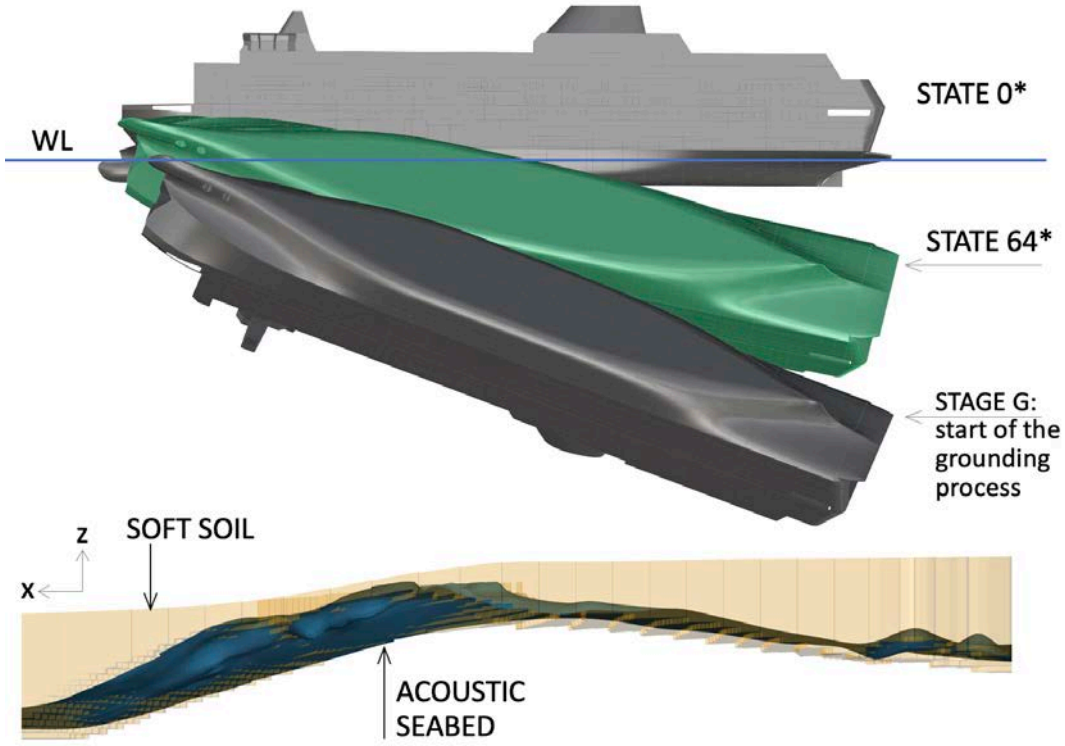

Figure 3. Ship orientation during the sinking (* State 0 & 64 are from Krüger, 2008).

3.1 Orientation and loading condition

The loading condition is defined in means of ship mass m, displacement Δ, centres of gravity and buoyancy. During the flooding and foundering of the ship, these values are constantly changing. Earlier studies have simulated the foundering process during the stage where the aft trim was increasing as the ship aft was sinking towards the bottom. A final fully reported stage calculated by (Krüger, 2008) is visualized in Figure 3 as State 64. This state corresponds to a trim angle of 12.6° and to a list of 121° to starboard. However, at this stage the ship is still away from the sea bottom. Valanto & Friesch (2008) suggest that the ship will reach to the sea bottom at a trim angle of 22° and list of 133° to starboard. This orientation is visualized in in Figure 3 with dark grey and denoted as State G. The corresponding trim and list angles are used as the initial orientation for the assessment.

Detailed data for the loading condition is only given for the State 64 in (Krüger, 2008). Required initial conditions for state G prior the bottom contact are not available from earlier studies and are to be constructed. The following assumptions are made while defining the initial loading conditions just prior to the bottom contact (state G):

- A1. The ship is fully submerged, buoyancy Δ has achieved maximum value and remains constant;
- A2. At the beginning of the simulations, the ship weight mg is equal to its buoyancy Δ;
- A3. Ship's longitudinal centre of gravity LCG coincides with the longitudinal centre of buoyancy LCB in global reference frame as the ship is in quasi-static equilibrium;
- A3. Water ingress continues to increase the ship mass m and shifts the LCG forward and away from LCB;
- A4. Increasing distance between the LCG and LCB, and the increasing ship mass m results in trimming moment that starts to submerge the ship bow.

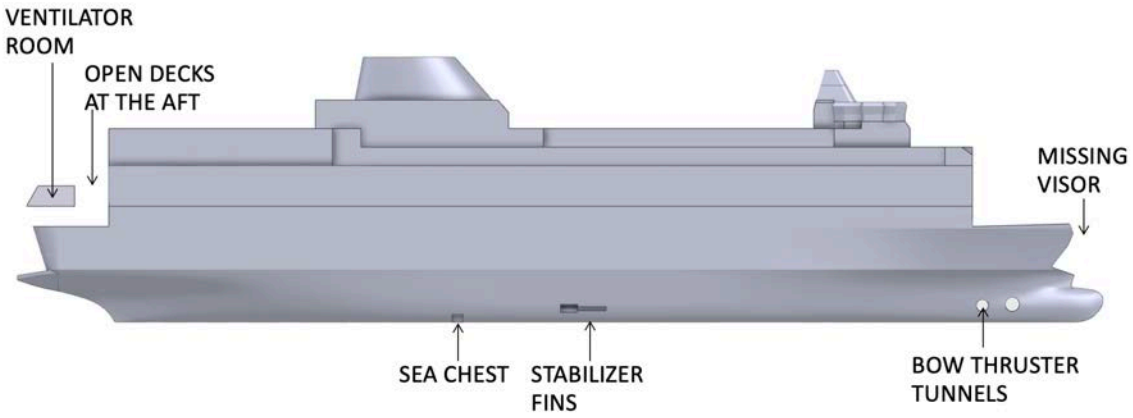

Figure 4. Ship volume definition.

The volume of the fully sunken ship is defined from the hydrostatic model presented in Section 6.3. This volume includes the full ship excluding the open deck areas at the aft of the ship, boxes for stabilizer fins, sea chests, bow thruster tunnels and the visor volume, see Figure 4. The ventilator room in the open deck area at the aft is included. Total volume of the sunken ship is 75 343 m^3 resulting in buoyancy of 75 644 t. Shell plating factor 1.007 and water density 1.004 t/m^3 is assumed. The centre of buoyancy of this volume, and thus also the centre of gravity according to the assumption A3 above, locates at $x_B=x_G$=62.1m; $y_B=y_G$=-0.0m; $z_B=z_G$=13.62 m.

Table 2. Load condition (component distribution and mass values from Kehren, 2009).

Mass component	Mass [t]	Equiv. density [t/m^3]	Vol-ume [m^3]
Lightship	9 673	7,8	1240
Deadweight	2306	1,26	1830
HFO	255	0,9	283
MDO	34	0,9	38
Gas oil	10	0,85	12
Ballast water	359	1,004	358
Fresh water	273	1	273
Vehicles (incl. 200 tons of timber)	1100	1,89	580
Crew and passen-gers, luggage	100	0.9	111
Misc liquids	50	1	50
Pool	25	1	25
Misc	100	1	100
TOTAL	**11 979**		**3 070**

Considering the loading condition of the ship as defined in (Kehren, 2009), the volume of the steel structure, equipment, cargo and liquids onboard totals roughly in 3 070 m^3 (Table 2). Thus, the amount of water that could flood the ship is 75 343-3 070=72 273 m^3 or 72 562 t. The total mass of the ship consists of lightship mass, deadweight and of the mass of flooded water is 84 541 t. Taking into account the buoyancy of 75 644 t , the remaining ship mass in water i.e. the apparent mass is 84 541-75 644 =8 897 t (Table 3). As in stage *G* the ship mass is assumed equal to its maximum buoyancy, the ship mass can still increase by 8 897 tonnes from stage G until the situation the is fully flooded and has achieved the the maximum mass of 84 541 t.

Table 3. Ship mass and buoyancy at state *G*

Item	Weight (t)	Comment
Lightship mass w/o visor	9 673	Equiv. volume 1240 m^3
Deadweight	2 306	Equiv. volume 1830 m^3.
Mass of flooded water	72 562	Equiv. volume 72 273 m^3 (ρ=1.004 t/m3)
Mass of fully flooded ship	84 541	Lightship + deadweight + flooded water; (9673+2306+72562= 84541 t)
Buoyancy of fully sunken ship	75 644	Equiv. volume 75343 m^3 (ρ=1.004 t/m^3, plating factor 1.007)
Apparent mass of the ship	8 897	Total mass - buoyancy; (84541-75644= 8897 t)

In the analysis of (Krüger, 2008) the flooding rate from stage 63 to stage 64, i.e. the final simulated stages, is q_{64}=63.7·10^3 kg/s, i.e. about 64 tons of water was entering the ship at every second. The shifts in the centre of gravity per unit mass of flooding water between the stages 63 and 64 are evaluated from the reported data in (Krüger, 2008):

$$\frac{dLCG}{dm} = 4.5 \cdot 10^{-7} \left[\frac{m}{kg}\right]$$

$$\frac{dVCG}{dm} = 4.7 \cdot 10^{-8} \left[\frac{m}{kg}\right] \quad (1)$$

$$\frac{dTCG}{dm} = 2.35 \cdot 10^{-9} \left[\frac{m}{kg}\right]$$

It is assumed that the same flow rate and the shifts in COG position apply also for the constructed state *G*.

3.2 Ship position with respect to the sea bottom

Photogrammetric image of the wreck is used to position the ship with respect to the sea bottom, Figure 5. The wreckage geometry created from the photogrammetry data is only used to position the ship in the horizontal XY plane. It should be noted also that the soft seabed and the bedrock at the ship wreckage are modelled based on the photogrammetry data, see Section 3.3. The ship wreckage, the surface of the reconstructed soft seabed and the bedrock are correctly located with respect to each other as their corresponding photogrammetry data is recorded in the same coordinate system. This ensures, that the ship model, which is positioned with respect to the wreckage, is also in correct location with respect to the topologies of the bedrock and of the soft seabed. It is agreed that in the analysis the initial position of the ship is translated in Y direction by approximately 4 meters to compensate for the ship's shift along the sea bottom over the years. However, different displacement values are tested as well as discussed in Sections 4.3 and Table 7. In X direction the corner points of the ship model and the wreckage roughly match. In vertical direction the ship model is positioned as close to the soft seabed as possible to assure the minimal gap and thus, reduce the required simulation time.

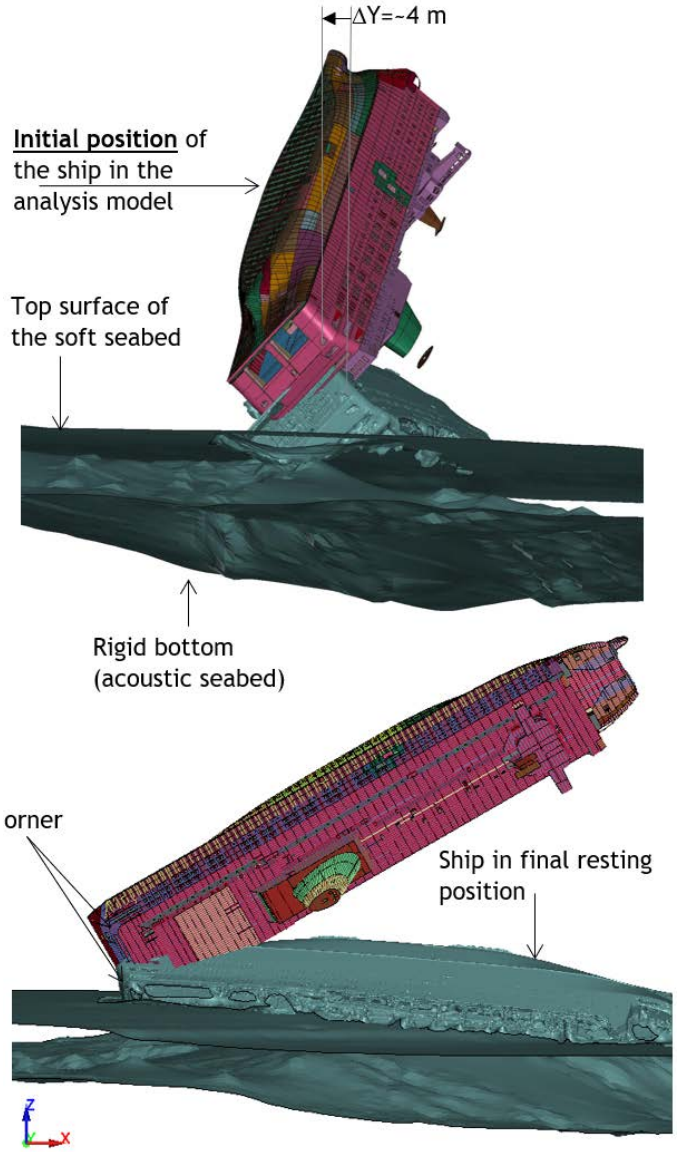

Figure 5. Ship position at the onset of the simulations.

3.3 Seafloor and sub-bottom geology

Stockholm University carried out geophysical mapping and geological coring at the MV *Estonia* wreck site between 8th and 15th of June, 2021, with research vessel RV *Electra* (Jakobsson *et al.*, 2021). The main purposes were to establish the present position of MV *Estonia* on the seafloor and map the seafloor topography (bathymetry) and geology of the wreck site.

A sediment thickness model based on the acquired data from 2021, as well as previously gathered geological information from the wreck site, was presented in the report by (Jakobsson *et al.*, 2021). An important input to this model were ROV (Remote Operated Vehicle) camera inspections that revealed outcropping bedrock near the ship hull side damage opening found in MV *Estonia*. The sediment thickness model revealed a ridge that appears to rise up beneath MV *Estonia*, while there are soft and rather thick sediment layers surrounding the wreck along the eastern, western and southern sides (Figure 6, Figure 7).

Bottom surface around and below the ship contains glacial clay, post-glacial clay, till and bedrock, see Figure 7.

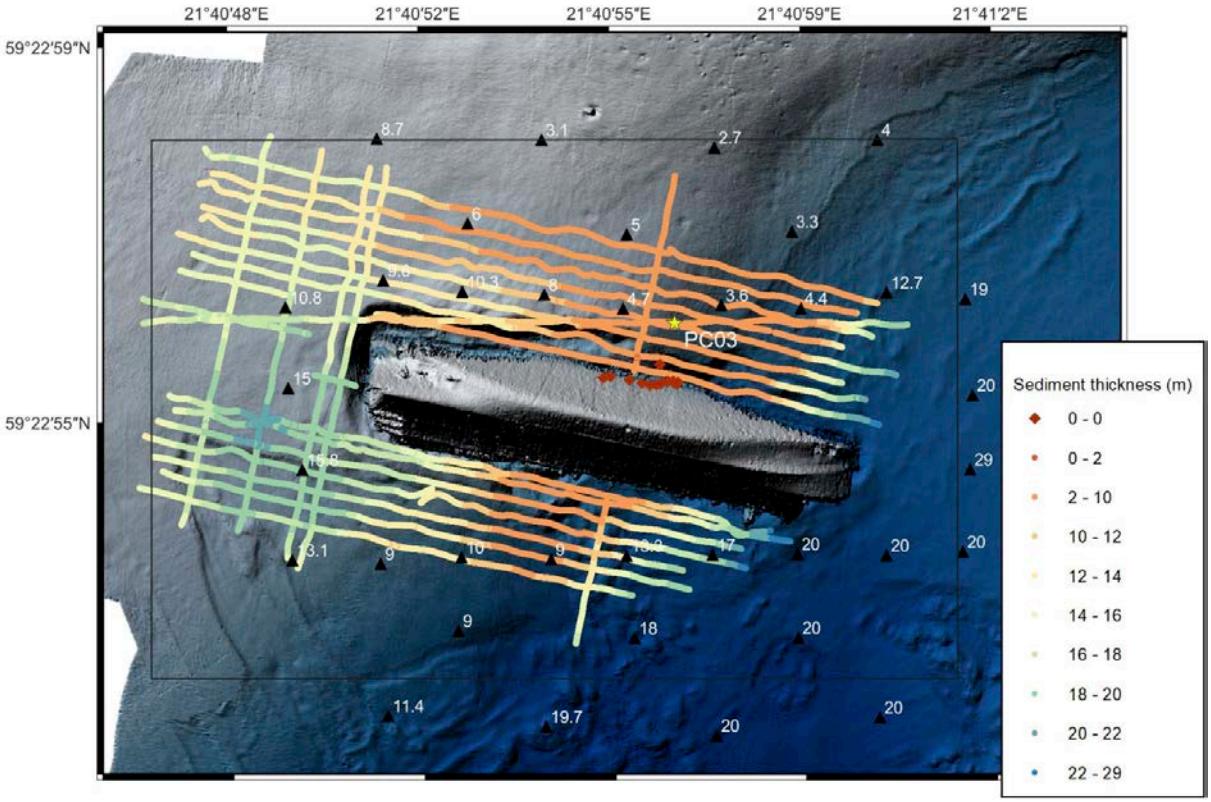

Figure 6. Source data used to construct the sediment thickness model of the MV Estonia wreck site.

The ridge (Figure 8 and Figure 9) was proposed to most likely be composed of bedrock, although the sub-bottom profiles acquired with RV *Electra* did not permit to distinguish if parts of it consists of till. In 2022, the companies Ocean Discovery AB and JD-Contractor A/S were contracted to carry a photogrammetric documentation of the wreck and its contact with the seafloor and acquire addition sub-bottom profiles to further constrain the sediment thickness at the wreck site. New ROV inspections were included in 2022 where the arm of the ROV was used to "probe" where bedrock had been found to outcrop from visual inspection during 2021. It was confirmed that the seafloor along the northern side of MV *Estonia* close to the two holes was comprised of hard rock.

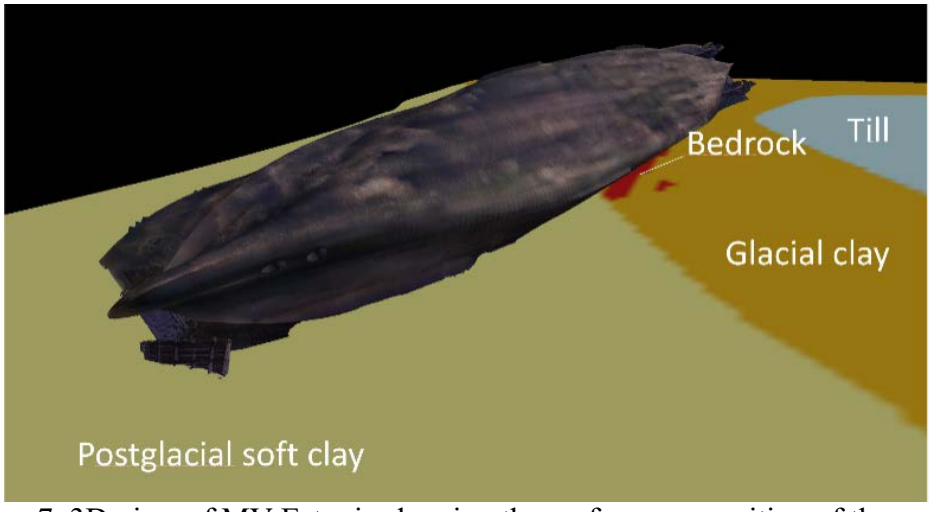

Figure 7. 3D view of MV Estonia showing the surface composition of the seabed.

The updated sediment thickness model based on data both from 2021 and 2022 is here used as a basis for the numerical bottom contact modelling. Figure 6 presents the different data sources. These include sediment thickness values derived from the sub-bottom depths to the acoustic basement comprised of till or bedrock, interpreted in the sub-bottom profiles from 2022 (coloured dots), Cone Penetration Tests made by Delft Geotechnics in 1996 (black triangles), and the observations of outcropping bedrock from the ROV inspections in 2021/2022 and the photogrammetric mosaic (red squares). The sediment core PC03 from the investigation by Stockholm University in 2021 is shown as a reference as it bottomed in bedrock (yellow star).

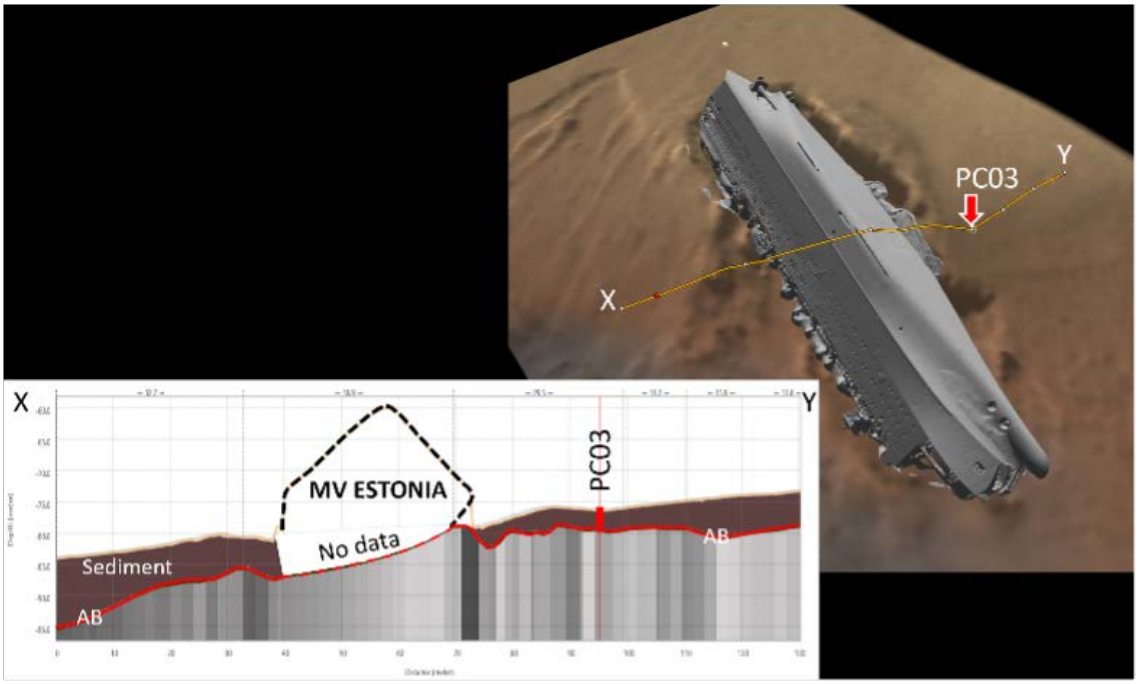

Figure 8. Profile across MV Estonia showing how the acoustic basement (AB), comprised of till or bedrock, forms a ridge below the wreck and outcrops near the two holes in the hull. The location of sediment core PC03 is shown, which bottomed in bedrock.

The bathymetry at the wreck site has been restored to simulate the conditions before MV *Estonia* impacted with the seafloor. It is important to note that there is no information regarding the shape of the acoustic bottom directly under the ship, see the dashed line in Figure 8. Two different bottom shapes are modelled as presented in Section 4.1. Figure 9 present the constructed acoustic basement and the exposed bedrock.

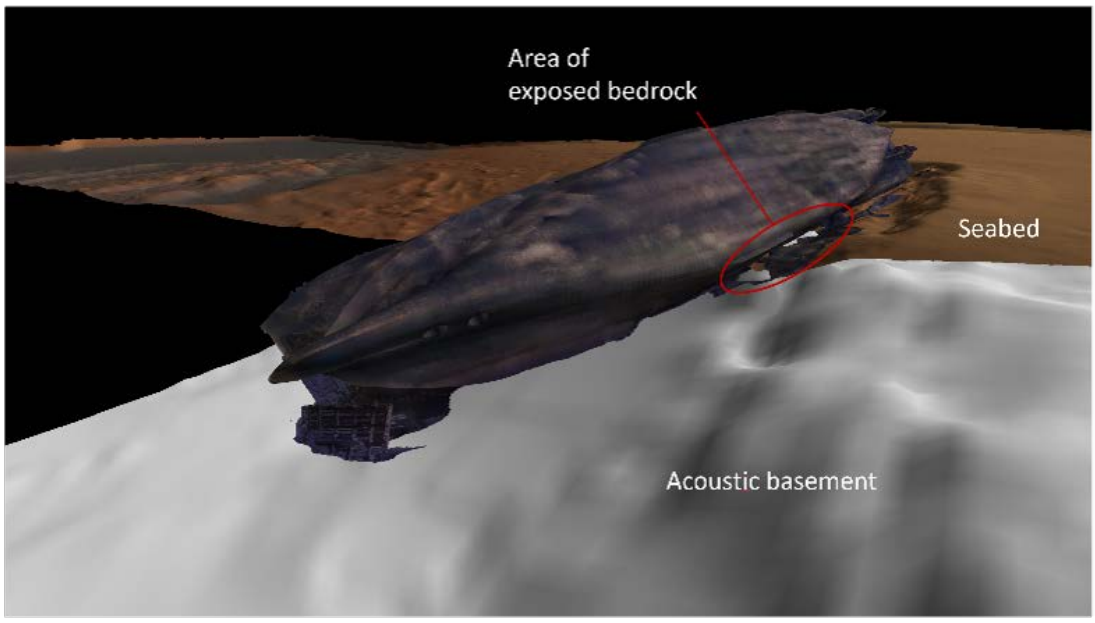

Figure 9. 3D view of MV Estonia and the reconstructed acoustic basement.

4. MAIN UNCERTAINITIES

There are several uncertainties involved in the assessment process. Only the uncertainties having a considerable influence on the simulation results are discussed here.

4.1 Shape of the acoustic bedrock under the ship

One of the biggest uncertainties concern the shape of the acoustic sea bottom under the ship hull as indicated by the dashed line in Figure 8. The acoustic basement has a role in defining the character and extent of the local contact between the sea bottom and the ship. The shape also has the influence on the ship motions along the bottom.

Figure 8a indicates the source data and the initial assumption for the shape of the acoustic bedrock. With this initial assumption very smooth surface is generated under the ship, referred to as V1 and depicted at Figure 8b. However, as seen from Figure 8a, the measured regions around the ship indicate much less even shape of the acoustic bottom. Therefore, a bottom shape V3 was generated by lowering the smooth surface to generate a sharper ridge under the ship, see Figure 8c. This sharper shape is also supported by the underwater images of exposed bedrock next to the hull damage of MS Estonia observed in the Discovery+ documentary by Henrik Evertsson, see Figure 11. These underwater images reveal rather rapidly changing acoustic bottom instead of very smooth bottom. (Additional acoustic bottom shape V2 was generated, but it is not reported and presented here.)

a) source data

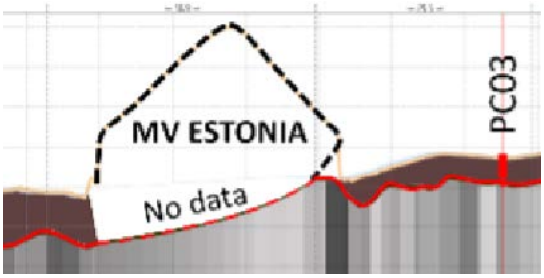

b) V1: smooth acoustic bottom

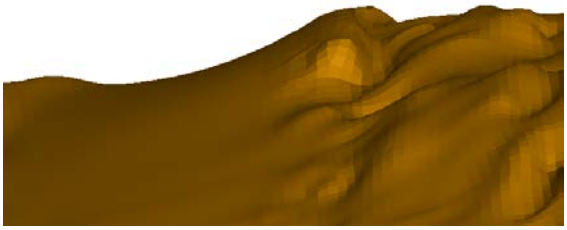

c) V3: sharp acoustic bottom

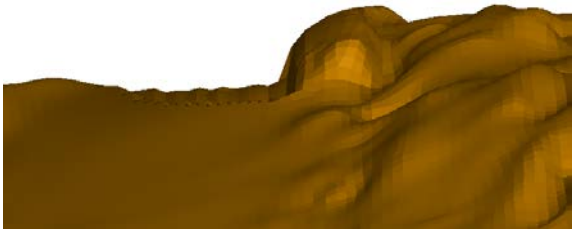

Figure 10. Assumed shapes of the acoustic basement.

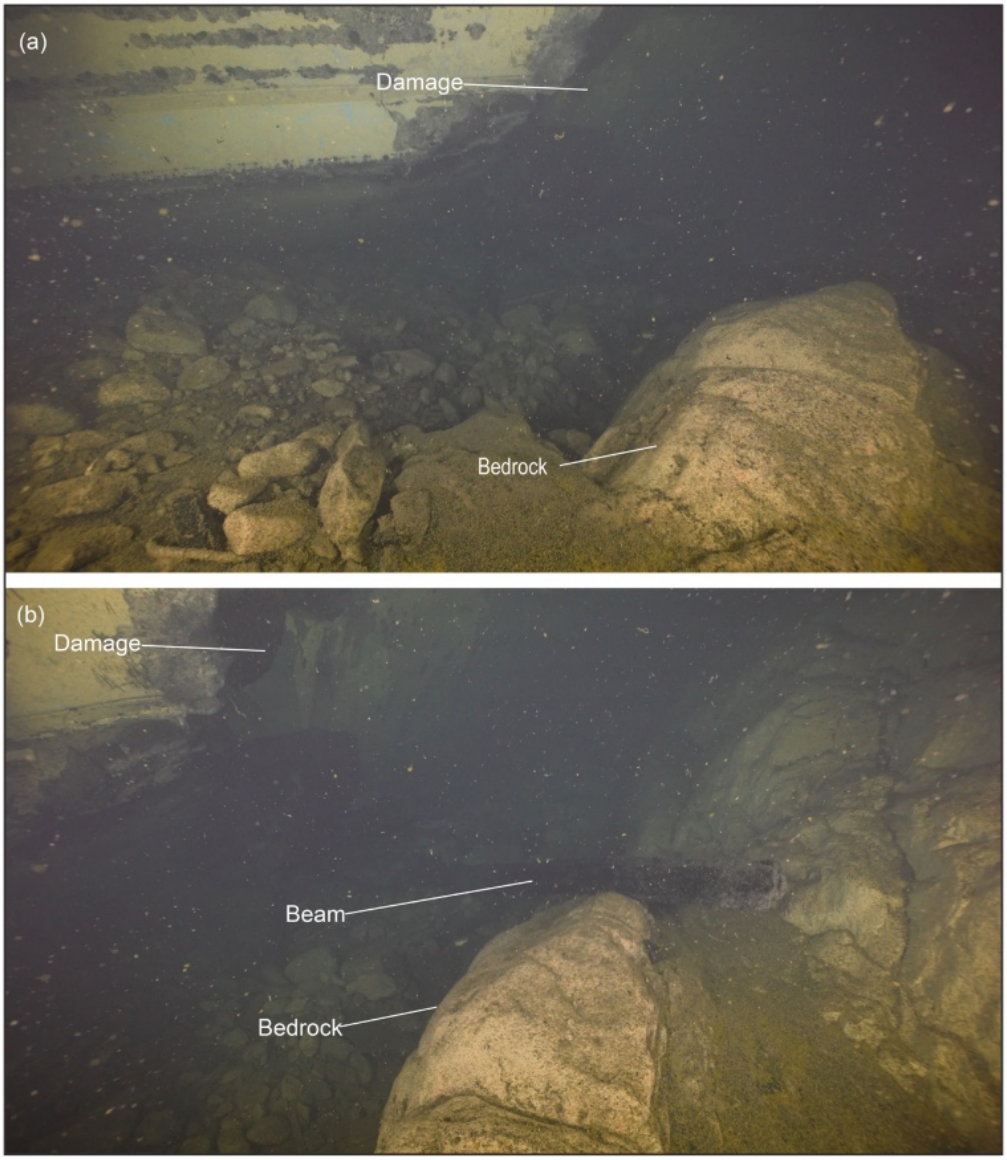

Figure 11. Bedrock exposed next to the damage in the hull of MS Estonia first observed in the *Discovery+* documentary by Henrik Evertsson. (Figure reproduced from Jakobsson *et al.*, 2021).

4.2 Mechanical properties of the soft sea bottom

Second major uncertainty concerns the numerical characterization of the soft sections of the sea bottom. Numerical modelling of the soft sea bottom sections consisting of glacial and post-glacial clay are discussed in Section 6.1. With limited data available about the mechanical characteristics of the soft sea bottom, there is a considerable uncertainty regarding the response of the soft soil as it gets compressed. To assess this uncertainty, the parameters defining the response of the soft sea bottom were varied as shown in Figure 17.

4.3 Ship position with respect to the sea bottom

As already discussed in Section 3.2, there is uncertainty regarding the exact falling position of the ship. The current registered position of the vessel is not necessarily its initial position as the ship has shifted and rolled at the bottom over the years. Two different sideways positions are tested according to Table 6.

4.4 Change in ship angular position during sinking

Significant uncertainty is involved in the exact angular position of the vessel when it collides with the sea bottom. Simplified simulation model presented in Section 5 assumes fixed roll angle, and due to its simplified nature, the possible change in roll angle during the falling phase cannot be evaluated. Thus, the main assumption of the roll angle of 133 deg is based on the constructed initial conditions according to Section 3.1. However, the roll angle of 113 deg is simulated as well to see its effect on ship's final position and structural damage (Figure 12). With smaller roll angle, the ship falls flatter on the protruding ridge and thus, larger local deformations are expected.

a) roll angle 133 deg

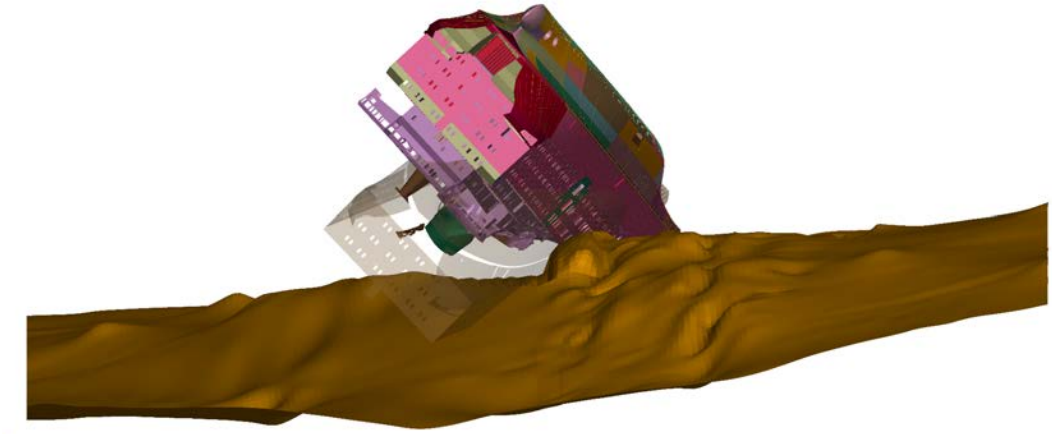

b) roll angle 113 deg

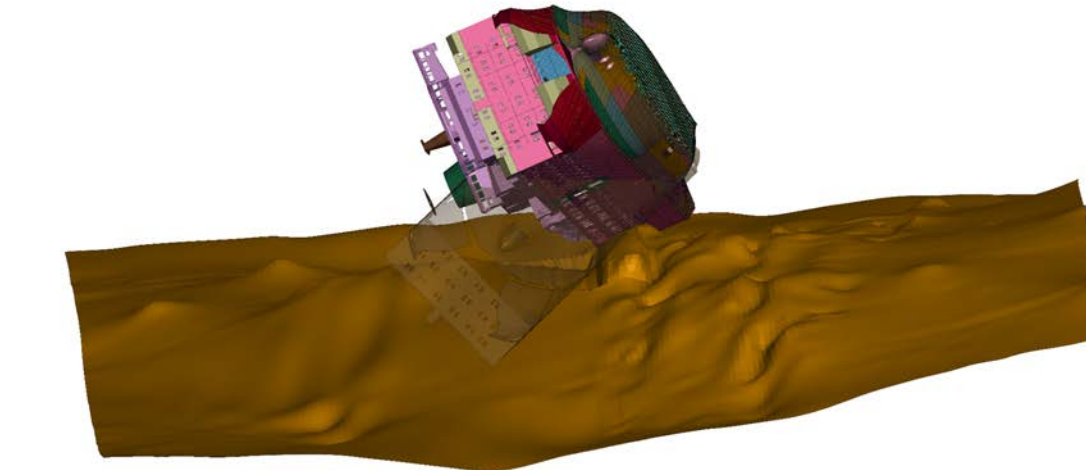

Figure 12. Angular positions of the ship assumed in numerical simulations. Current position of the ship wreck is indicated by transparent model.

4.5 Flooding rate & change in loading condition

Uncertainty is associated with the flooding rate of the ship and the shifts in the centre of gravity due to the water mass. Two different simplified flooding model are used, and various flooding rates are simulated with the simplified model presented in Chapter 5. The influence of flooding model and flooding rates on the sinking dynamics are presented in Figure 14.

4.1 Structural deterioration in time

Last uncertainties are associated with slow processes that have taken place over the time period of 29-years the ship wreckage has been at the sea bottom. While only modest dynamic loads are expected to act at the ship hull, they still could contribute to further propagation of structural damages due to fatigue.

In addition to modest dynamic loads, the stressed structures experience creep. Creep is the tendency of a solid material to undergo slow deformation while subject to persistent mechanical stresses. Creep occurs as a result of long-term exposure to high levels of stress that are still below the yield strength of the material. Creep could contribute to further deformations of the ship hull and to the crack propagation.

5. SINKING DYANAMICS: SIMPLIFIED MODEL

The aim of the simplified model is to simulate the ship's final sinking stage, where ship comes to full contact with the sea bottom. The focus is on the situation that starts when the ship aft touches the sea bottom and ship starts to fall towards the sea bottom as the trim angle increases due to the distance between the centre of gravity (COG) and the centre of buoyancy (COB).

5.1 Theory

As detailed flooding simulations are not withing the scope of the study, several simplifications are done. Significant simplification concerns ship geometry. Ship is idealized by a circular cylinder having a diameter equal to ship breadth B and length L equal to ship length between perpendiculars, that is $L = L_{pp}$. Ship stern is in contact with sea bottom while the ship bow is marginally below the water surface (stage G in Figure 3). There is an increasing ground reaction force R acting at ship stern being in contact with the sea bottom. However, it is assumed that this force is small compared to the gravity and the buoyance that are in approximate equilibrium at the beginning of the last stage of the sinking process.

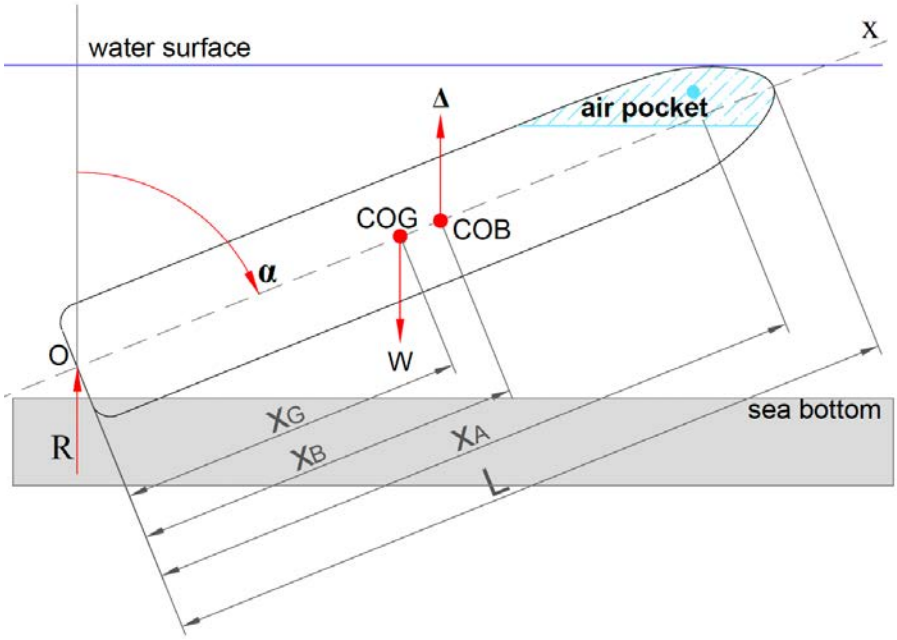

Figure 13. Simplified sinking model.

Principle of the simplified model is depicted in Figure 13. Ship's total weight, including the flooded water, acts at COG and is denoted by $W=mg$ and its longitudinal location is defined by x_G. Buoyancy is defined as $\Delta = \rho g \nabla$ and it acts at COB. Volumetric buoyancy ∇ includes entire ship structure, except the non-watertight parts as discussed in Section 3.1. Ship has an air pocket, which centre of volume in longitudinal direction is denoted by x_A.

The initial angular position of the ship is given by α_0 as defined in Section 3.1. The situation presented above can be regarded as the initial condition for the last stage of the sinking simulations.

Final phase of descending of the vessel can be described by a single-degree-of-freedom system with the angular position of the ship α being the variable to be solved. The proposed model can be considered as the inverse pendulum.

5.2 Inertia and drag

Apart the statically acting forces, there are loads associated with the velocity and acceleration of descent. These are inertia of the hull and that of the added mass, inertia and flux of the flooding water and drag.

Inertia moment of the hull can be expressed as follows

$$M_I = -\left(I_z + x_{\mathrm{G}}^2 \frac{W}{\mathrm{g}}\right)\ddot{\alpha} \qquad (2)$$

with I_Z being mass moment of inertia of ship, which can be approximated by $I_Z = W/\mathrm{g} * (L/4)^2$. Similarly, moment due to the radiation effects can be presented as

$$M_{IA} = -I_{\mathrm{added}}\ddot{\alpha} \qquad (3)$$

Added moment of inertia of the immersed cylinder can be approximated by

$$I_{\mathrm{added}} = \rho\pi B^2 L^3/12 \qquad (4)$$

Flow resistance is evaluated using the so-called cross-flow drag model. In this model local drag $D(x)$ per unit length at section x is given by

$$D(x) = -\frac{1}{2}\rho C_{\mathrm{D}}(x) B v(x)|v(x)| \qquad (5)$$

where C_{D} is local drag coefficient and $v(x)$ flow velocity normal to the section x. The drag coefficient is taken as C_D=1.14.

Assuming constant value of drag coefficient and integrating local drag along ship length results in motion resisting moment

$$M_D = \int_0^L D(x)dx = -\frac{1}{8}\rho C_{\mathrm{D}} B L^4 \dot{\alpha}|\dot{\alpha}| \qquad (6)$$

5.3 Water inflow

In stage *G*, the ship is in quasi-static equilibrium and as both the gravity and buoyancy located at the same point, i.e. COG=COB, there is no external moment applied to the ship. As the ship is fully sunken, the maximum buoyancy has been achieved and the COB is fixed with respect to the ship throughout the subsequent sinking. However, the ship still has an air pocket that could fit 8 897 tonnes of water (Table 3). As this air pocket gets filled, the ship mass starts to exceed the buoyancy and the COG shifts towards the bow. This generates a trimming moment, and the ships starts to turn towards the sea bottom as the trim angle decreases. The water inflow plays a crucial role in defining the sinking dynamics in this final stage.

Precise simulation of water inflow would require the detailed information about the air-pocket sizes, locations and inflow rates that depend on the cross-sectional area of the inflow orifices and pressure levels. Provided the above data, the inflow can in principle be solved with Torricelli Theorem. However, the magnitude of such simulations and the required amount of data exceeds the scope of this assessment. Thus, a simplified approaches are developed to approximate the water inflow.

As a first approach, the water inflow is defined as a decayed flow in time. Initial inflow rate is assumed to be $q_{64}=q_G$=63.68 ton/sec and the shifts in COG as a function of mass increase are defined by eq. (1), see also Section 3.1 and (Krüger, 2008). Inflow rate in time is approximated as

$$q(t) = e^{-bt} q_G \left[\frac{kg}{s}\right] \qquad (7)$$

where b is a decay coefficient. With b=0, there is no decay, and the ship is flooded at constant rate q_G until fully filled. With $b>0$, the flow is decayed in time.

It is obvious and demonstrated with the black curves in Figure 14 that the decay coefficient has a strong influence on the sinking dynamics. However, there is no simple physical model to define an appropriate decay coefficient. To provide a more physical meaning for flooding of a compartment having entrapped air, as a second approach we use Boyle-Mariotte gas law that describes the compressibility of the air as a function of pressure. By an isothermal assumption of the situation during the sinking of the MV Estonia, the volume decreases proportionally to the increasing pressure, with:

$$\mathrm{V}_i = \mathrm{V}_{i-1} \frac{p_{i-1}}{p_i} \; [m^3] \qquad (8)$$

where V_{i-1} and p_{i-1} are the volume and pressure of entrapped air at the time integration step i-1 (simulation time $t=(i-1)dt$, where dt is time integration increment); in time step i ($t=idt$) the pressure increases to p_i due to the descent of the ship bow and the entrapped air is compressed to volume V_i.

Inflow rate per time can be calculated from the change in volume as

$$q(t) = \frac{\mathrm{V}_i - \mathrm{V}_{i-1}}{dt} \rho \left[\frac{kg}{s}\right] \qquad (9)$$

where ρ is water density.

We assume that the air lock position is defined by x_A, which is also used to define the height of the water column and thereby the pressure p. The ship trim angle is decreasing as the ship rotates around the point O (Figure 13), the air lock falls deeper, the pressure increases, and the air gets compressed making space for flooding water to enter.

In each integration timestep the ship mass m is updated by the mass increase

$$m_i(t) = m_{i-1} + dm_i = m_{i-1} + q(t)dt \qquad (10)$$

and the longitudinal centre of gravity is updated according to the coefficients in eq. (1) as

$$LCG_i(t) = LCG_{i-1} + \frac{dLCG}{dm} dm_i. \qquad (11)$$

To start the air compression process, an initial imbalance between the buoyancy and ship mass is generated by allowing a small amount of water to flood into the ship in the first calculation step. The influence of this initial imbalance, measured in proportion to initial inflow q_G, is shown in Figure 14. The figure also presents the effect of the location of the air-lock that is defined by x_A.

5.1 Equation of motion

Summing up all the terms and rearranging them so that the acceleration term is left on the LHS, the final form of the equation of ship descent to sea bottom is obtained as

$$\ddot{\alpha} = \frac{\left[(Wx_{\mathrm{G}} - \Delta x_{\mathrm{B}})\sin\alpha - \frac{1}{8}\rho C_{\mathrm{D}} B L^4 \dot{\alpha}|\dot{\alpha}|\right]}{\frac{W}{\mathrm{g}}\left[x_{\mathrm{G}}^2 + \left(\frac{L}{4}\right)^2\right] + \frac{\rho\pi B^2 L^3}{12}} \tag{12}$$

Equation of descending motion is a second order non-linear differential equation. Equation is linearized within a time increment *dt* assuming that the changes in the angular coordinate and its time derivatives are small within the time increment. Furthermore, all the forces were assumed constant during *dt*. Under these assumptions, the solution at the time t_i is found if the solution at the time t_{i-1} is given. Equations are solved using 4th order Runge-Kutta method.

5.1 Sinking dynamics

Results of the simplified model are exemplified in Figure 14 that presents the development of trim angle over the time. In the left of Figure 14 the trim angle prior the bottom contact is shown based on the data from (Krüger, 2008). This initial stage ends with the state *G*, when the ship's aft becomes to contact with the sea bottom. At the right of Figure 14 the trim angle development beyond the state *G i*s presented under different modelling assumptions. The trim angle decreases as the ship bow sinks. When the trim angle reaches to zero, the ship is horizontal and the simulation ends.

The effect of the inflow decay coefficient (eq.7) is exemplified with black lines. If the flow remains constant throughout the sinking (*b*=0), the trim angle decreases fast and the ship becomes to full contact with the sea bottom in about 40 seconds. With very strong decay (*b*=1) the increase in ship mass slows down rapidly and the final sinking stage takes more than 250 seconds.

From the simulations, where the inflow is controlled by air compression (eq. 8), interesting conclusions can be drawn. The initial imbalance between the mass and the buoyancy (described via inflow in the first step: $1q_G$, $0.1q_G$, $0.01q_G$, $0.005q_G$) delays the start of the sinking process as with smaller imbalance, e.g. with 0.005 q_G, it takes more time for the ship to start descending. However, after a critical imbalance and the shift in COG has been achieved, the descent follows the similar pattern independent of initial imbalance.

The location of the air lock (x_A=50, 75, 125 m) has similar influence. When the air lock is closer to the bow (x_A=125 m), the change in trim angle results in larger vertical shift of the air lock compared to the air lock more towards aft (x_A=50 m). Larger vertical shift means larger pressure difference and largerwater inflow, thus resulting is quicker descend toward the sea bottom.

Thick pink lines in Figure 14 present the equivalent acceleration field that are applied to the apparent ship mass to achieve the descent dynamics comparable to those achieved by the simplified model. The equivalent acceleration field ranges from 0.12*g* for a sinking process lasting about 40 seconds to 0.005*g* for a sinking process lasting about 250 seconds (*g* is gravitational constant *g*=9.81 m/s).

In numerical simulations reported in subsequent sections, it is assumed that the angular motion lasts about 40 seconds i.e. the equivalent acceleration field 0.12g is assumed. This corresponds to angular velocity of about 0.6 deg/sec.

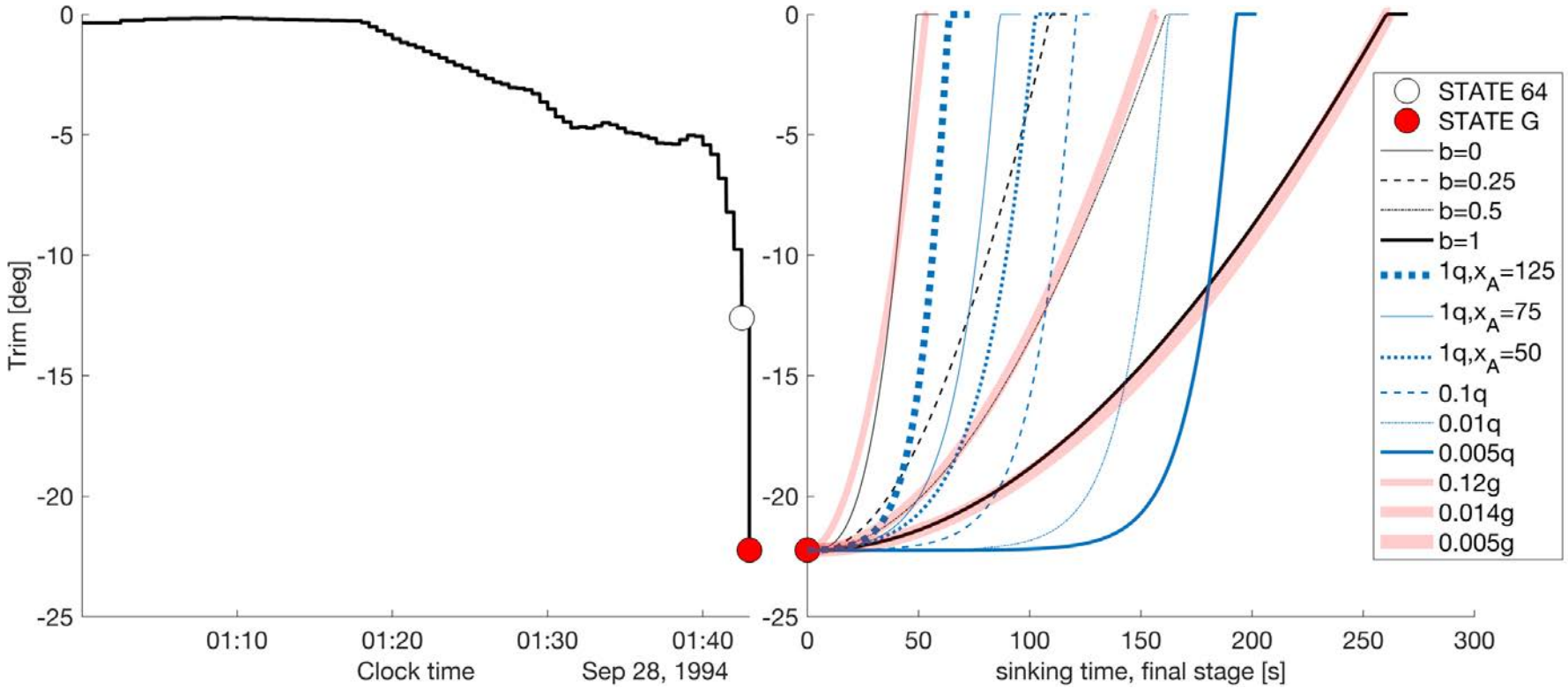

Figure 14. Trim development in time under different assumption (*left:* trim angle before the first bottom contact (Krüger, 2008); *right:* trim angle after the bottom contact. Black lines present the sensitivity to the inflow decay coefficient, blue lines present the sensitivity to initial imbalance between the buoyancy and the ship mass, and to the location of the air lock. Thick pink lines present the simulations with equivalent gravity and the apparent ship mass).

6. NUMERICAL MODEL

Detailed numerical model consists of the sea bottom model and of ship model. Water around the ship and flooding is not modelled and the results of the simplified sinking model in the form of equivalent acceleration are used to define the sinking dynamics. Numerical simulations are conducted in LS-Dyna using explicit time integration. Ship and the acoustic bedrock are modelled using mainly shell elements and the soft sea bottom is modelled using solid elements and Multi Material Arbitrary Lagrangian Eulerian (MMALE) approach.

6.1 MMALE approach for the soft sea bottom

In the sea bottom modelling the main challenge is on the description of deformation process of the soft seabed. MMALE approach is used to describe the behaviour of soft soil and its interaction with the ship.

MMALE approach allows the materials to undergo very large deformations, that is required to model the compression of the soft sea bottom. It can handle the contact with the rigid (acoustic sea bottom) and deformable objects (ship), and allows tracking of free surface between two different MMALE domains- water and soft soil in this case. Both soil and water can be present in the same volume element, which improves the computational stability in the case of large deformations and the surface between the materials is tracked. However, in these simulations the water domain is left void for computational efficiency. In that way, the void has a sole role of providing the space for the soil to move upwards. The effect of omitting the water domain in tracking the free surface of the deforming soil is assumed negligible.

The multi-material arbitrary Eulerian formulation is applied to the soil and void domain, and the Lagrangian formulation for the ship and the acoustic bedrock surface (Figure 15). MMALE principle and advantages for the problems with large displacements and deformations are well summarized in (Bakroon *et al.*, 2018).

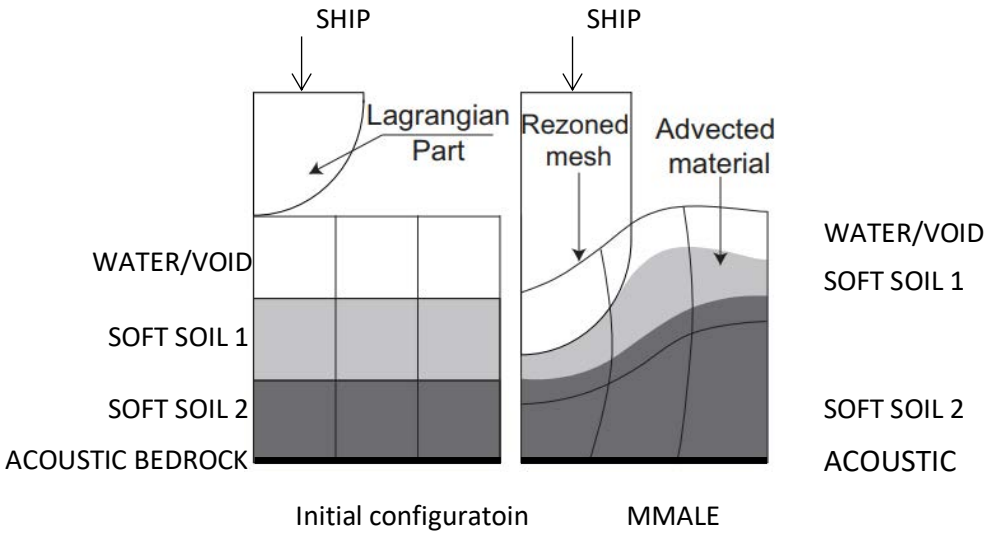

Figure 15. Schematic diagram of Multi Material Arbitraty Lagrangian Eulerian (MMALE) approach used to model the interaction between the ship, soft soil and acoustic bedrock. Figure modified from (Bakroon *et al.*, 2018)

The core of the MMALE method is Arbitrary Lagrangian Eulerian (ALE) algorithm, that is a computational method consisting of both Lagrangian and Eulerian formulations that applies conservation equations in the finite element analysis. To prevent large distortions, the mesh in the ALE method can update its position according to related parameters, see Figure 15 for the principle. This results in more stable calculations, where the mesh distortions are reduced as the mesh gets rezoned. This rezoning is possible due to three main characteristics of the method: the Lagrangian mesh can travel into the Eulerian mesh, the same volume element can include different materials and the material mass inside the element does not have to remain constant.

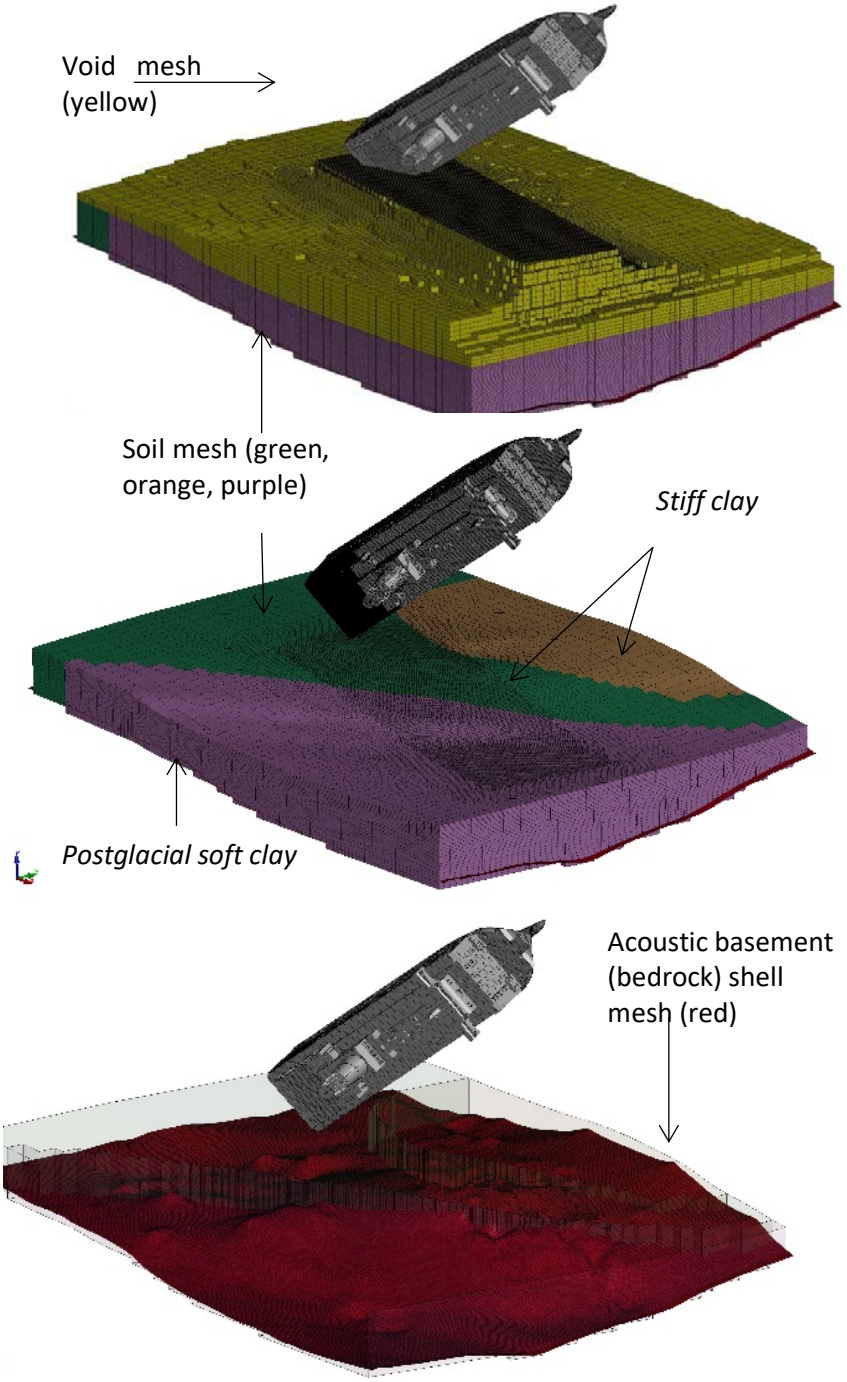

Figure 16. FE model of the seabed: void and soft soil is modelled with solid elements, and acoustic basement with shell element.

In this method, the calculation in each time step is separated into two parts. First, the Lagrangian phase is carried out, in which the ship mesh moves with the soil particles and the changes in velocity, pressure, and internal energy caused by external and internal forces are computed. As there is no material flow through the element boundary, the calculation satisfies mass conservation. Accordingly, the equilibrium equations of the velocity and energy can be calculated. In the second step, called the transport or advection phase, the transportation of mass, momentum, internal and external energies of materials across the elements' boundaries are computed. Velocity and displacement of each node are updated accordingly.

In soil-structure interaction problems, coupling between structural and solid domains is a challenging task and may affect the accuracy of the results. The coupling between the domains occurs at their shared interface, where the soil pressure is transferred to the structure while the nodal velocities of the soil are constrained to be equal to the nodal velocities of the structure. There is continuity of velocity and stress normal components on both sides of the shared boundary. In the Euler-Lagrange coupling, the structure is embedded in Eulerian mesh, which is rezoned, if required, for the convergence and computational stability. The Eulerian mesh contains the Lagrangian structure and MMALE soil, which flows across the mesh using the advection strategy to update velocity and history variables. For structural domain, the MMALE approach poses no limitations to the configurations to be analysed with Lagrangian approach.

The MMALE volume element mesh consists of the soil mesh and the void mesh (Figure 16) which serves only as a space where the soil material can expand into during the deformation. The soft seabed is modelled with hexahedron solid elements. In the region where the ship is expected to hit the soil a finer mesh with an element size of 1000 mm is used. Away from that region the mesh gradually increases being largest at the boundaries of the seabed, where the element lengths can reach up to 5 m.

Below the soft seabed is the acoustic basement (bedrock), which is modelled as rigid undeformable surface with quadrilateral shell elements with typical element size of 1000 mm, see the red surface in the bottom of Figure 16.

In the analysis model, the nodes on the sides of the solid mesh boundaries are constrained sideways meaning that the material cannot escape out of the boundaries in X and Y directions. Acoustic bottom is fixed in space in all the directions.

A fluid-structure contact (FSI) is applied between the ship and the soil. For the contact between the soil mesh and the rigid acoustic bottom, the FSI contact is not used even though it would be appropriate. However, due to very large contact area this contact would be computationally very expensive. Instead, in depth direction the soil geometry extends up to the bedrock surface and the translations of the bottom nodes are constrained. Contact between the ship and the rigid bedrock is modelled via penalty-based contact.

6.2 Mechanical properties of the soil

The material behaviour of the soft and the stiff clay are modelled using LS-Dyna material model MAT_SOIL_AND_FOAM (MAT005), where the material behaviour is described with pressure-volumetric strain curve and pressure independent yield strength. The compression curves for both clays are constructed based on compression index, initial void ratio and preconsolidation pressure, see Figure 17. The yield surface is determined by the coefficients a_0, a_1 and a_2 which according to (Wright, 2012) can be calculated based on soil undrained shear strength c and internal friction angle φ as

$$a_0 = \frac{4c^2}{3}$$
$$a_0 = \frac{8\tan\varphi}{3} \quad (13)$$
$$a_0 = \frac{4\tan^2\varphi}{3}$$

The shear strength of both clays is controlled by undrained shear strength, see in Figure 18. The geotechnical parameters of the soils are taken from (Rudebeck and Kennedy, 2021; Jakobsson, 2023) and are presented in Table 4. Appendix A provides further insight into the definition of mechanical properties for soft soil.

(a)

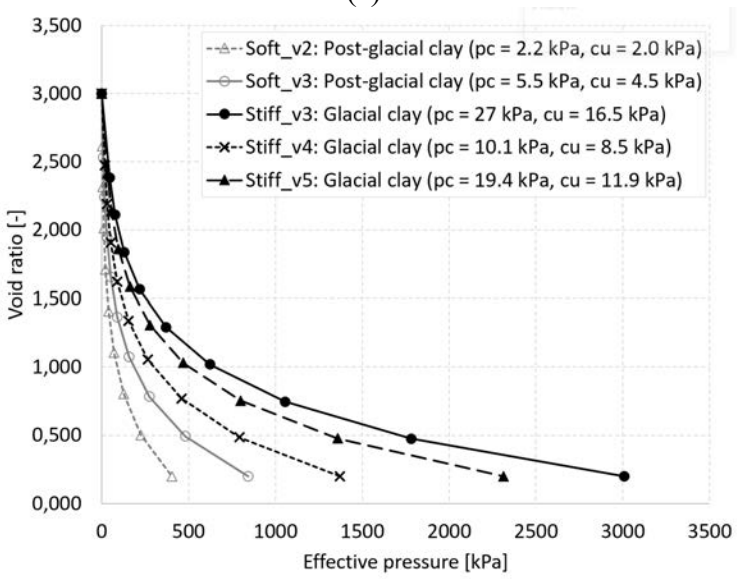

(b)

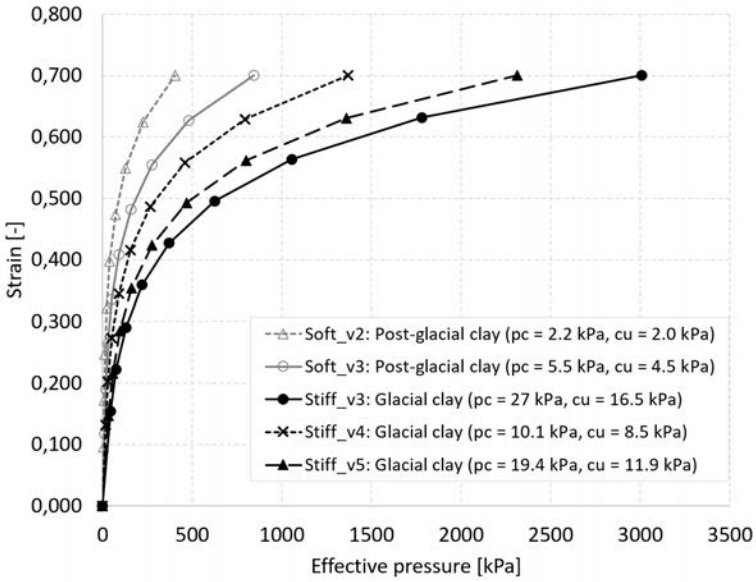

Figure 17. Constructed compression curves for soft clay and stiff clay: (a) compression curve presented as effective pressure vs void ratio, (b) compression curve presented as effective pressure vs strain.

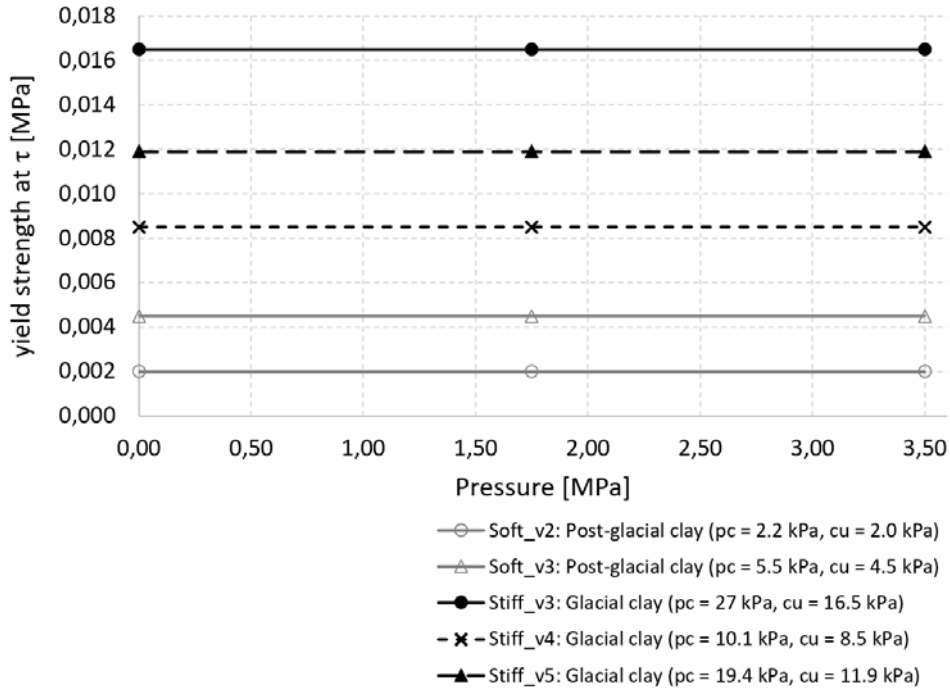

Figure 18. Yield strength of soft clay and stiff clay in LS-dyna material model MAT005.

Table 4. Geotechnical parameters of the soil materials.

Parameter	Value		Unit
	Soft clay (post glacial clay)	Stiff clay (glacial clay)	
Density, ρ	1400	1550	kg/m^3
Initial void ratio, *e0*	3.0	3.0	-
Compression index	1.2	1.2	-
Undrained shear strength, *cu*	2.2-5.5	10.1-27.0	kPa
Preconsolidation pressure, *pc*	2.2-5.5	10.1-27.0	kPa

6.3 Geometry and hydrostatic model

The ship model is made with NAPA software. NAPA package incorporates state of the art hull surface and 3D model definition with advanced hydrodynamic, stability and structural design software tools. The hull form and structural model are developed from scanned copies of original shipyard drawings provided by Estonian Safety Investigation Bureau. Geometric definition of retrofitted ducktail was approximated from 3D model of the ship available on Estonian Safety Investigation Bureau website.

The geometry model is developed with appropriate structural idealization to generate global finite element model with finer mesh as described (DNV, 2020, 2021).

The plate structures are modelled as surface objects. Primary supporting members are generally modelled with line elements with exception of web frames below car deck, which are

modelled with surface objects due to varying cross section. Deck longitudinals, bulkhead stiffeners, ice frames and ordinary frames are modelled with line elements. The openings larger than 400 mm in double bottom structures, decks, bulkheads and shell are included in the model.

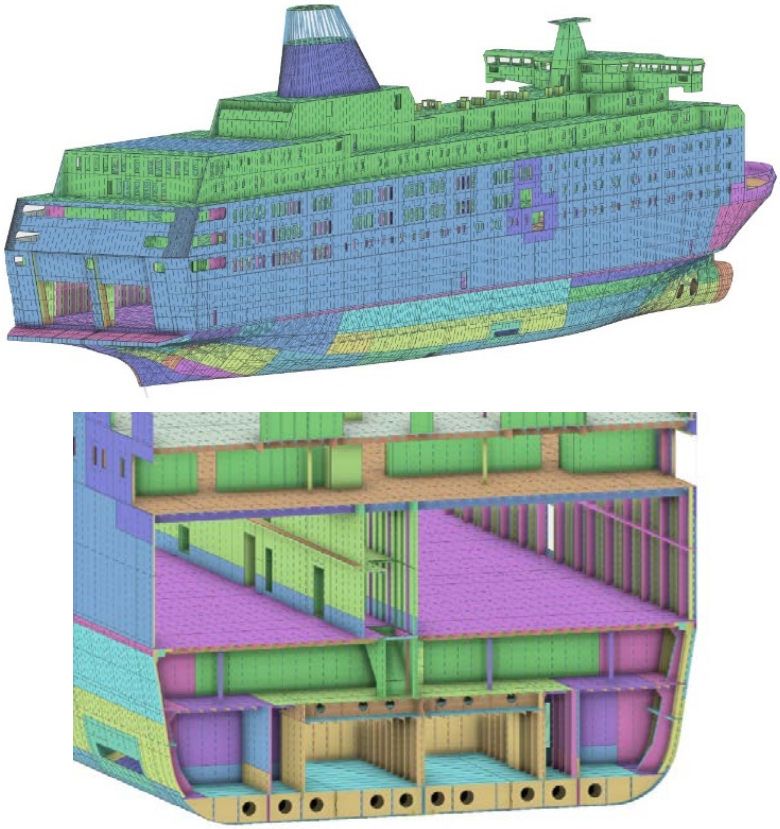

Figure 19. Geometry model of MV Estonia

Hoistable car decks and ramps are excluded from structural and geometry model. The ducktail structures are modelled assuming arrangement with transverse floors at every 3rd frame and longitudinal girders at every longitudinal. The structures of bow visor are excluded from the model.

The volume of the fully sunken ship is defined from the hydrostatic model prepared in NAPA. This volume includes the full ship excluding the open deck areas at the aft of the ship, boxes for stabilizer fins, sea chests, bow thruster tunnels and the visor volume, see Figure 4. The ventilator room in the open deck area at the aft is included. Total volume of the sunken ship is 75 343 m^3 resulting in buoyancy of 75 644 t. Shell plating factor 1.007 and water density 1.004 t/m^3 is assumed. The centre of buoyancy of this volume, and thus also the centre of gravity according to the assumptions above, locates at x_B=x_G=62.1m; y_B=y_G=-0.0m; z_B=z_G=13.62 m.

6.1 Structural assessment model

The ship hull is almost entirely made of steel S235 except the main deck structure, which is made of steel S355, see Figure 20. The ship hull and its main load carrying components are modelled in detail. The visor and the bow ramps are excluded from the model. Mass of the ramps is included. Interior fittings, cars, trucks and other deadweight components are not explicitly modelled, but are included in the analysis via structural added mass. The windows are not modelled as structural elements as they do not contribute to the strength of the ship, but

they are included in the analysis model only to improve the performance of the ship to soil interaction.

The structural model is discretized into finite element model using two different mesh resolutions, Figure 21 and Figure 22. Global coarse finite element model is first generated in NAPA steel with 300 mm mesh size. The webs of the web frames and girders are modelled with shell elements, while their flanges are approximated with beam elements. Side stiffeners and deck longitudinals are also approximated via beam elements, see Figure 22.

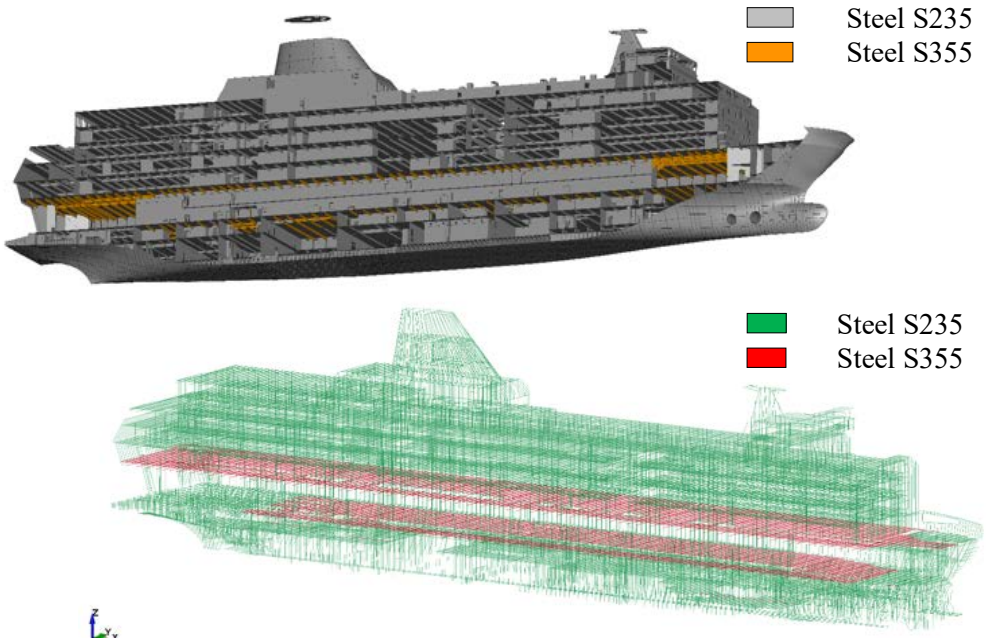

Figure 20. Different materials used in modelling (*above*: plate structures; *below:* stiffening elements).

This coarse mesh is checked for undesired element shapes is Siemens FEMAP, which is also used to refine the areas prone to material damage into finer local mesh with resolution of 20-35 mm. For the finer mesh regions also the flanges of the web frames, side stiffeners and deck longitudinals are modelled using shell elements, see Figure 22. Two different fine mesh models are generated, see Figure 21. In the first model the finer mesh is located only at the starboard side at the amidship region, while in the second model the fine mesh zone extends further aft and also the upper decks in the aft of the ship are modelled using fine mesh throughout the whole cross-section. However, the simulations with fine mesh model 2 are still to be conducted.

Plate structures are meshed with four-noded quadrilateral Belytschko-Lin-Tsay shell elements with five integration points through their thickness. Triangular elements are prevented as much as possible, even though these are still used in some regions. For the global coarse mesh the primary supporting members are modelled with shell elements for webs and beam element for flanges. Ordinary frames, ice frames, deck longitudinals, bulkhead stiffeners and pillars are modelled with beam elements. Brackets at the end of stiffeners are omitted.

For fine mesh regions also the smaller stiffening elements are modelled using shells, while the flanges are still modelled using beam elements. Brackets at the ends of stiffeners are included in the model, see Figure 22.

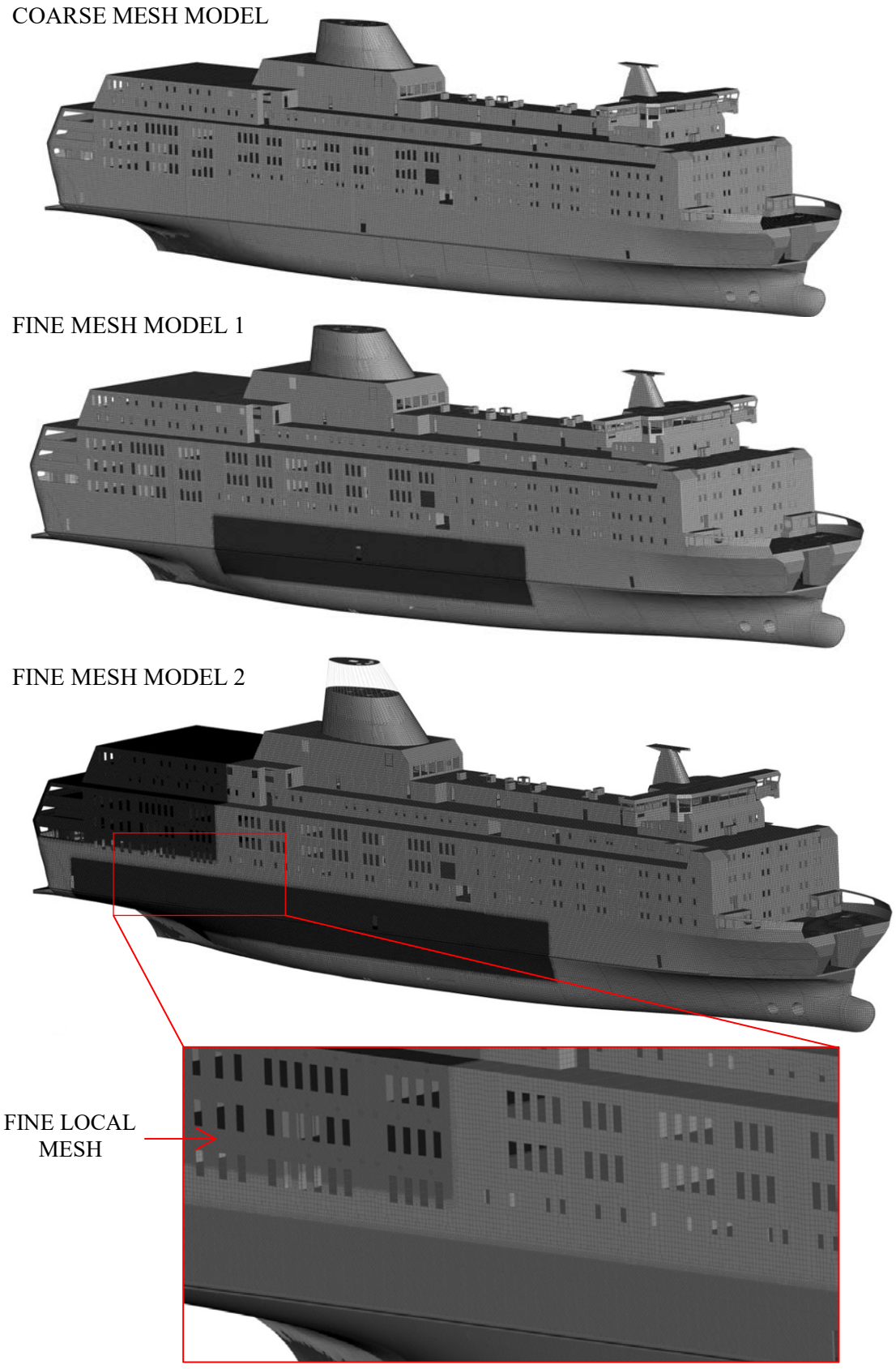

Figure 21. FE models of MV Estonia

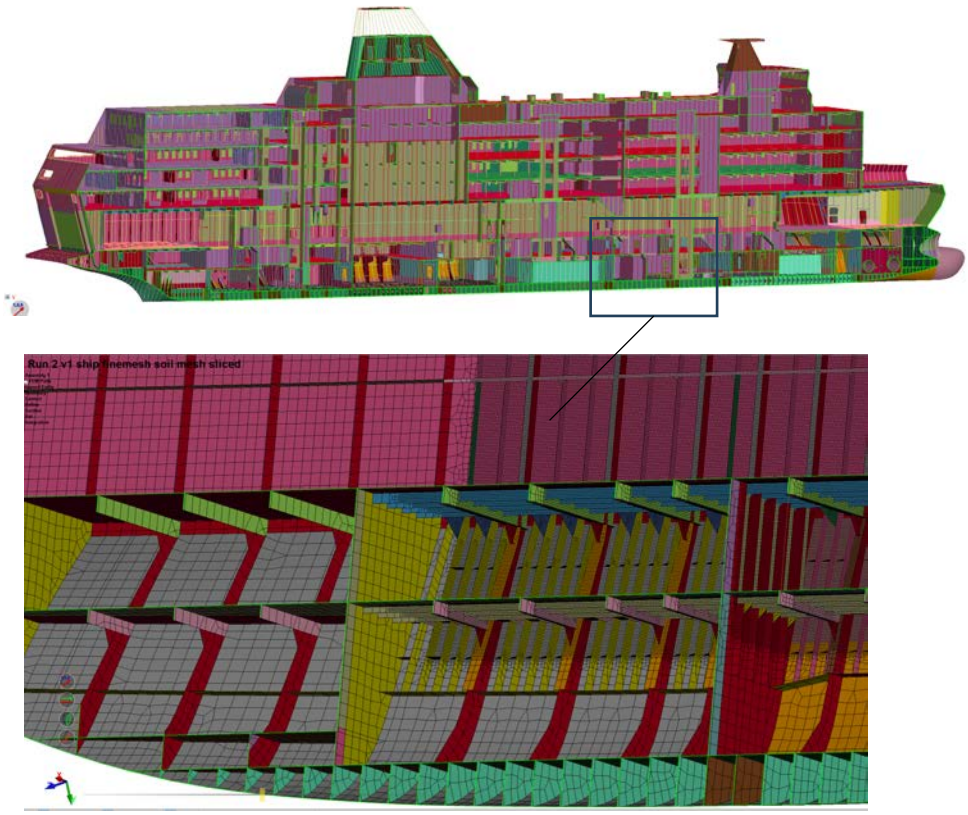

Figure 22. Modelling the stiffening elements

Nominal material properties used in modelling are show in Table 5. Material behaviour is described via true stress-strain relationship, see Figure 23.

Table 5. Material properties

Parameter	Value		Unit
	S235	S355	
Yield strength, R_{p02}	235	355	N/mm2
Ultimate strength, R_m	440	490-650	N/mm2
Elastic modulus, E	206 000	206 000	N/mm2
Density, r_s	7850	7850	kg/m3
Elongation, A_5	26	22	%

Possible material failure in plate elements is modelled using the thru thickness criteria, often referred to as Germanischer Lloyd criteria (Lehmann *et al.*, 2001). This criterion establishes an element thickness and dimension dependent critical thickness strain after which an element is removed from the simulation. To evaluate the critical thru thickness strain at the moment of fracture, an empirical criterion is presented by

$$\varepsilon_f(l_e) = \varepsilon_g + \varepsilon_e \frac{t}{l_e} \qquad (14)$$

where ε_g is the uniform strain and ε_e is the necking strain, t is the plate thickness and l_e is the individual element length. It is commonly recommended that the ratio l_e/t is not less than 5 for shell element. The values of uniform and necking strain achieved from thickness measurements related to the calculated stress states given in (Lehmann *et al.*, 2001) are 0.056 for the uniform strain and 0.54 for the necking strain in the case of shell elements.

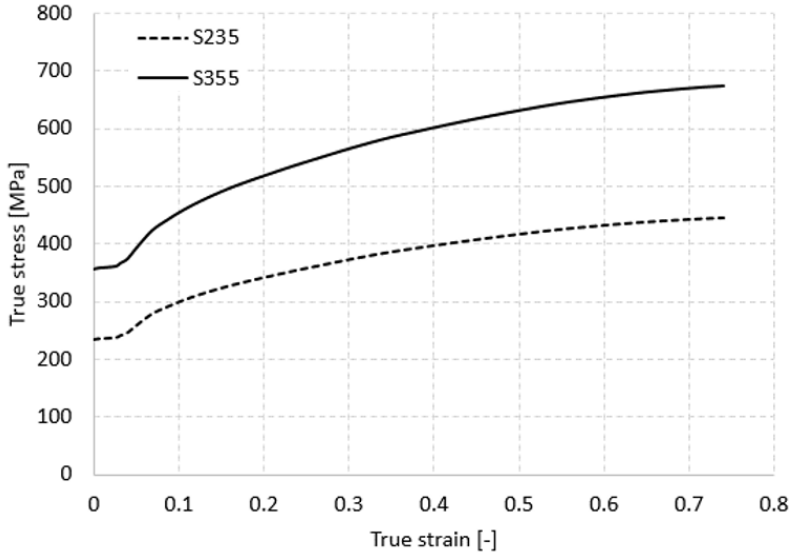

Figure 23. Plastic true stress-strain curves for steel S235 and S355.

6.2 Simulation setup and constraints

Numerical simulations are conducted at three stages:

1. The ship moves vertically downwards for the first 10 seconds and the aft of the ship penetrates into the soft sea bottom. Velocity of the downward speed is prescribed and the changes in ship orientation are constrained.
2. Angular motions towards the sea bottom. After the aft has penetrated into the sea bottom in stage 1 and the soil reaction force is equal to the apparent ship mass, the angular descent towards the sea bottom starts. Initially the angular velocity ω=0.6 deg/sec is prescribed to maintain the stability of numerical simulations and the allow for shorter simulation time.
3. After about 35 seconds, when the ship is close to the bottom, all the constraints are removed and ship is free to move towards the bottom and along the bottom under the gravitational acceleration of 1*g*.
4. At about 50 sec, sideways gravity of 0.125*g* is applied to force the ship to slide along the sea bottom. This is done to push the ship to its current reported position.

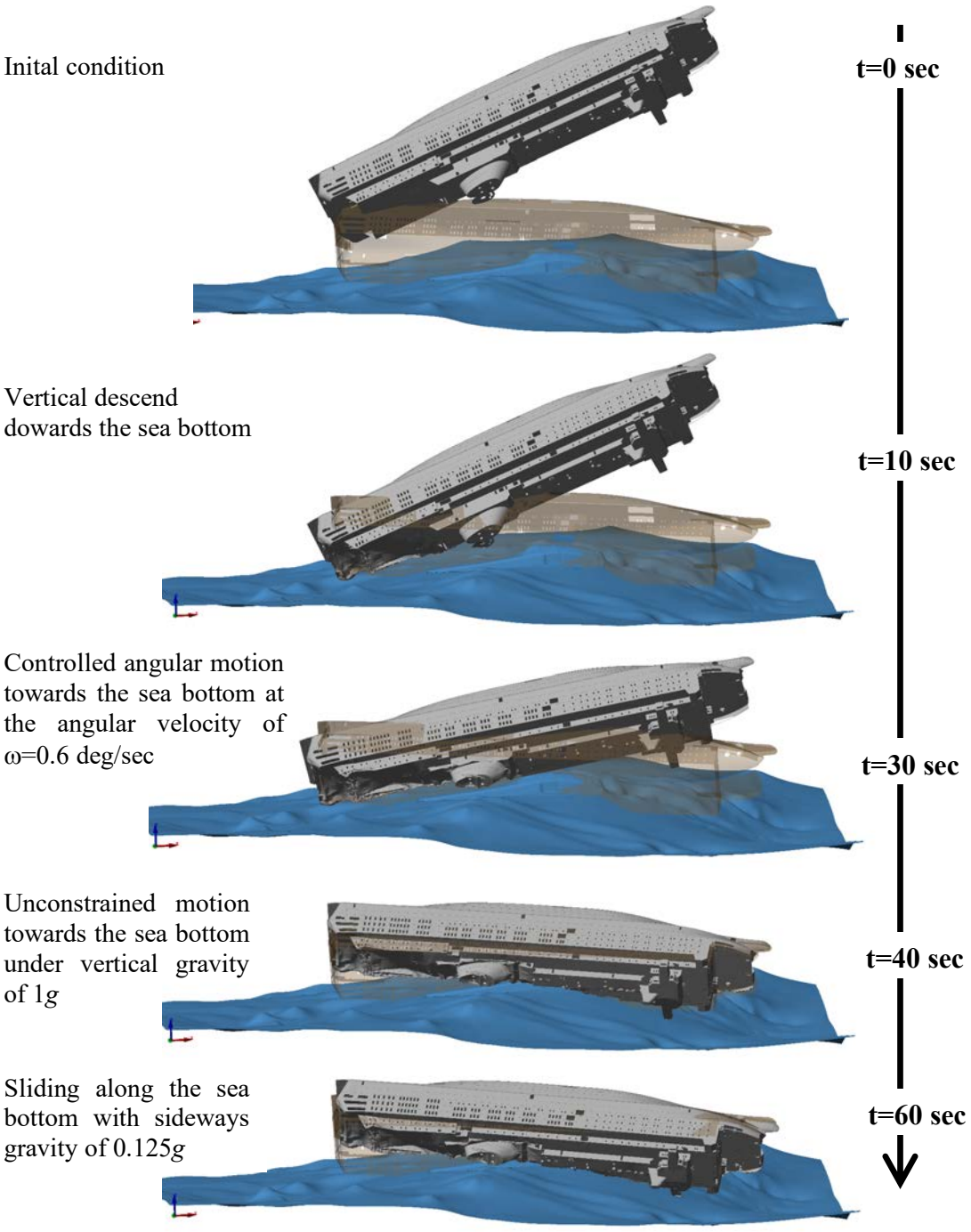

Figure 24. Stages of the numerical simulation (current position of the wreck is shown in transparent brown colour).

7. RESULTS OF NUMERICAL SIMULATION

Results of the numerical simulations are discussed. The simulated ship positions are compared to the current position and orientation of the shipwreck. The structural deformations obtained in different simulations are compared to those reported from the shipwreck.

7.1 Simulation matrix and computational resources

List of conducted numerical simulations is given in Table 6. The main simulation parameters such as ship's initial position, roll angle, ship mesh resolution and the bottom characteristics are provided.

A 64-core computer with AMD Razen Threadripper processor was used for the simulations. The simulations were typically conducted using 32 cores and single-precision Massively Parallel Processing (MPP) solver of LS-Dyna version R12.1 was used. Runtime for the simulations with coarse mesh models was about 10 days and for fine mesh models about 30 days. Due to long run times several parameters were only studied with coarse mesh models.

Table 6. Simulation matrix

ID	Ship mesh	Ship pos. in ΔY [m]	Roll angle [deg]	Bed-rock	Stiff soil	Soft soil
ID-5c	Coarse	4,3	133	v1	stiff_v3	soft_v2
ID-8c	Coarse	0,5	113	v1	stiff_v4	soft_v2
ID-10c	Coarse	4,3	133	v3	stiff_v3	soft_v2
ID-11c	Coarse	0,5	113	v3	stiff_v3	soft_v2
ID-12c	Coarse	4,3	133	v3	stiff_v3	soft_v3
ID-5f	Fine	4,3	133	v3	stiff_v5	soft_v3

7.2 Ship's final position with respect to the wreckage

The quality of the simulations is first assessed by comparing the simulated position and orientation to that of the shipwreck.

Both coarse mesh and fine mesh models resulted in very similar final position of the ship, even though there were some differences in structural deformations. Thus, only coarse mesh results are presented for comparison in Figure 25. Two roll angles are presented- 133 deg (ID10) and 113 deg (ID11). Roll angle 133 deg results in a ship position that is well comparable to the position of the wreckage. Ship's aft however remains higher compared to the wreckage. This suggests that the stiffer section of the soil (glacial clay) provides too strong support to the ship. Softer bottom would provide less support and would allow the ship aft to fall deeper and thus, closer to the position of the shipwreck.

With roll angle of 113 deg the differences are larger. Ship bow falls too deep and the aft remain too high. Also, the ship roll angle in its final position is different from the reported position. Further shift along the bottom would increase the roll, but would shift the ship too far to the South compared to the wreckage. In addition, softer glacial clay section would allow ships roll angle to increase. Simulations with softer glacial clay are still to be conducted.

Comparison of the final positions of the ship suggests that with initial roll angle of 133 deg the simulated ship position corresponds better to the current position of the shipwreck.

ID-10c (roll 133 deg) ID-11c (roll 113 deg)

a) isometric view

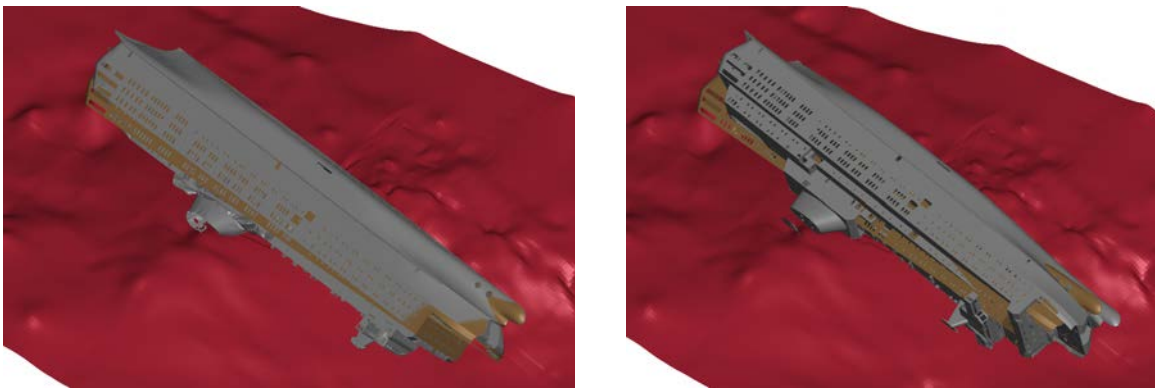

a) view from West

a) view from East

a) view from South

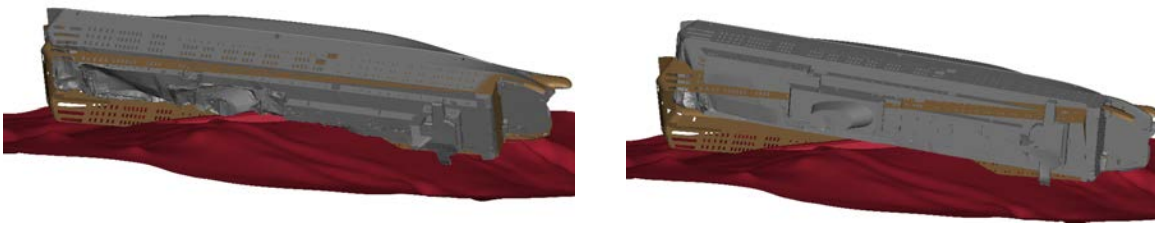

Figure 25. Simulated ship (*grey*) position with respect to the reported position of the wreckage (*brown*). Comparison of simulated ship position with initial roll angle of 133 deg (*left*) and 113 deg (*right*).

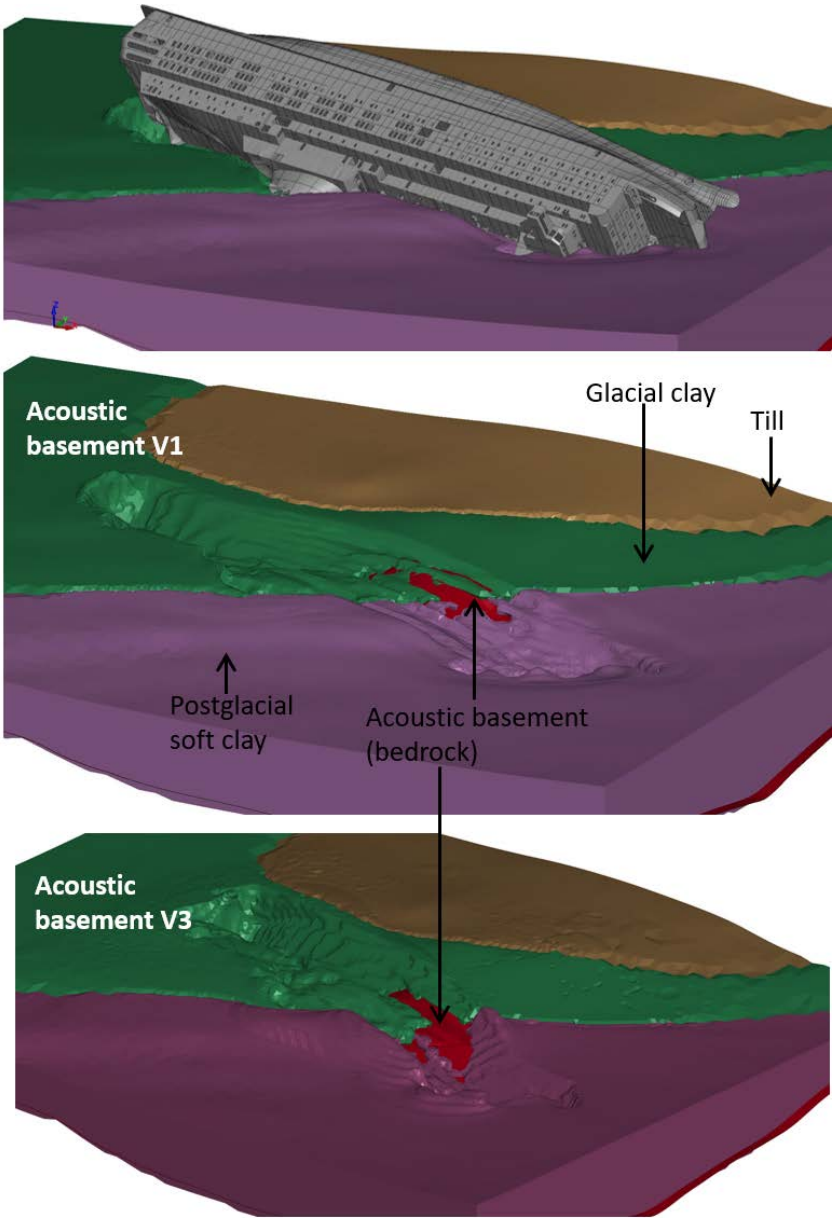

Figure 26. Ship final position (*above*) and the deformations of the sea bottom with two different acoustic basement shapes (*middle* & *below*). Simulation ID10c.

7.1 Deformation of the sea bottom

As the ship penetrates the soft sea bottom, the soil gets progressively compressed and the response from the soil increases according to curves in Figure 17. The support from the soft sea bottom is not sufficient to carry the full ship mass and the ship becomes to contact with the rigid acoustic basement (Figure 26). The support from the rigid acoustic basemen is strongest at the midships region, where the acoustic basement becomes clearly exposed as the soft soil is pushed away. Location and extent of this exposed acoustic bedrock corresponds well to the site measurements shown in Figure 7.

Ship trench at the soft bottom is clearly visible in the simulations, see Figure 26 and Figure 27. In the simulations the trench reaches less to the North compared to the site measurements shown at Figure 28. Narrower trench could indicate that in the simulations there was shorter horizontal ship shift towards South. However, as the ship's final position corresponds to the current position of the shipwreck, the longer shift along the bottom could only be achieved by

moving the initial contact location more towards North. These simulations are still to be conducted. However, the wider trench could also be due to the erosion of the soft soil over the years.

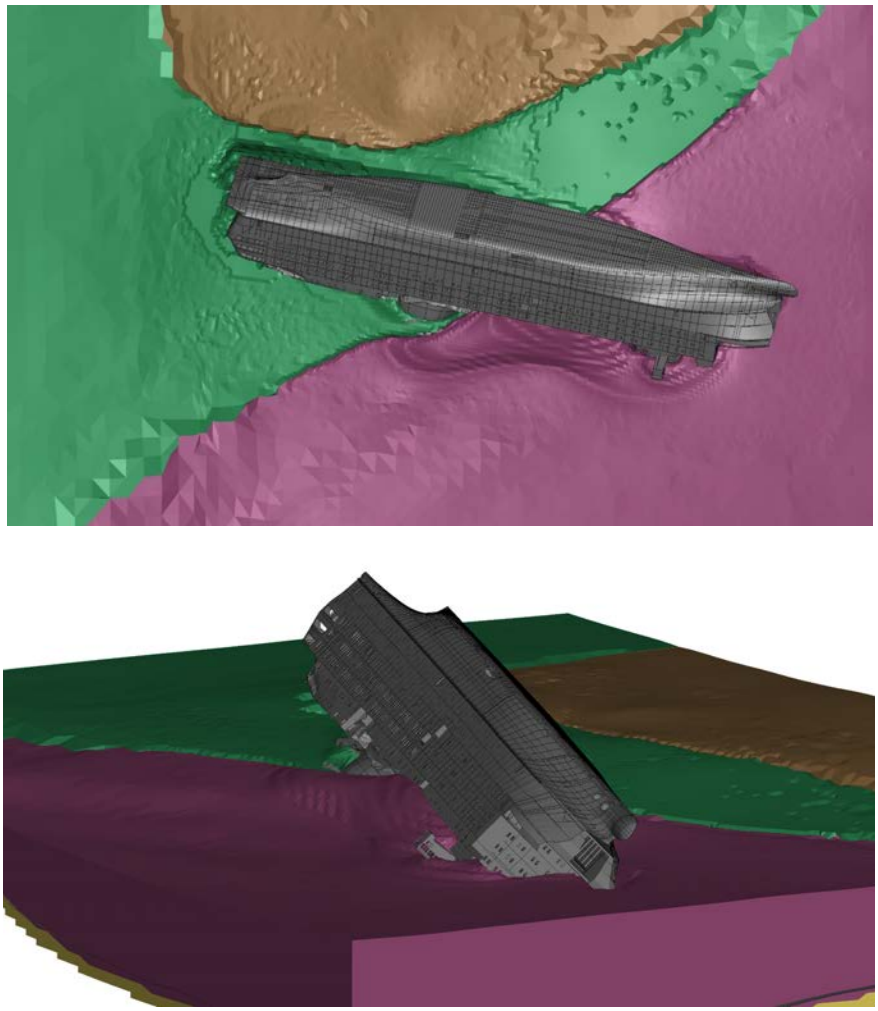

Figure 27. Ship's trench at the sea bottom. Simulation ID10c.

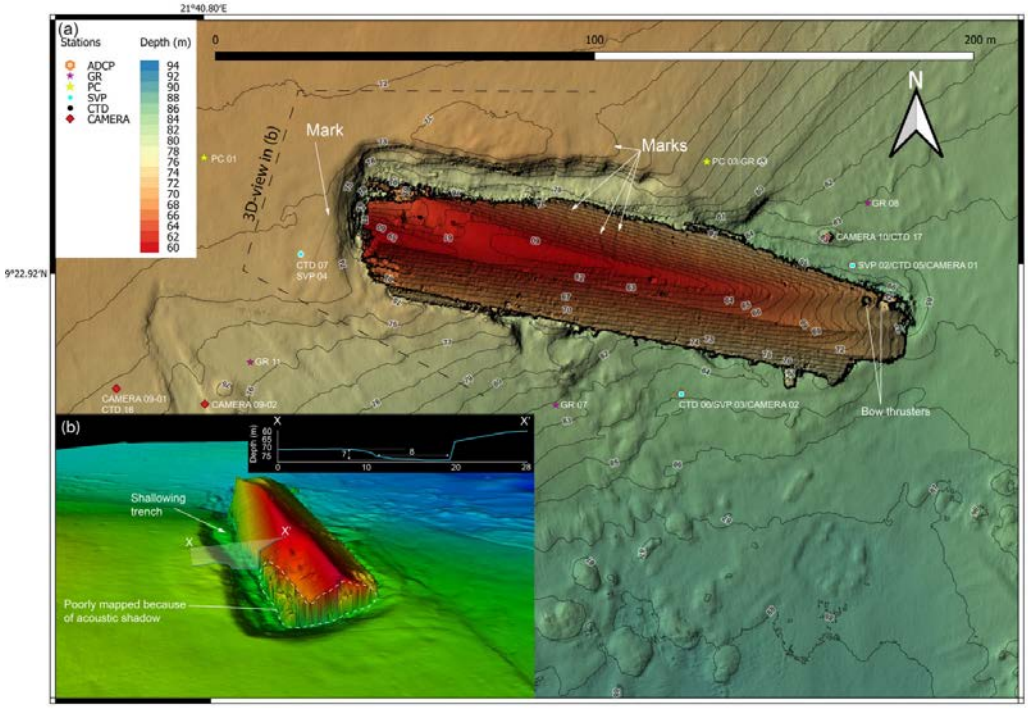

Figure 28. The shipwreck of MS Estonia portrayed with the detailed multibeam high-resolution grid. A 3D-view looking towards aft is shown in (b). This view clearly reveals the trench formed along the shipwreck. (Figure reproduced from Jakobsson *et al.*, 2021).

7.2 Ship structural damages

As a result of the descent to the bottom the ship achieves a position, where in the middle it is supported by the rigid acoustic bedrock while its bow is supported by post-glacial soft clay and the aft by glacial clay, see Figure 29. Under the hull, the soft soil is compressed several meters increasing the force response from the clay. Moreover, the support from the acoustic bedrock in the midship region is relatively local and thereby presents very hard local support surface for the ship.

Ships structural deformations in simulations ID10c (roll 133deg, acoustic bottom v3), ID11c (roll 113 deg, acoustic bottom v3) are presented in Figure 30 to Figure 35. Fringe levels in the figures show the permanent plastic deformations in the ship hull.

In both simulations, the extensive damage to the ship hull can be observed. With larger roll angle (ID10c), the upper decks of the ship are compressed from the ship aft until and beyond the midship region, see Figure 30. These deformations are mainly due to the contact with the soft sea bottom, which response increases as the soil gets compressed. In vertical direction, the damage extends from the uppermost decks until the fender guard (Figure 32). The starboard side of the bridge is clearly bent downwards.

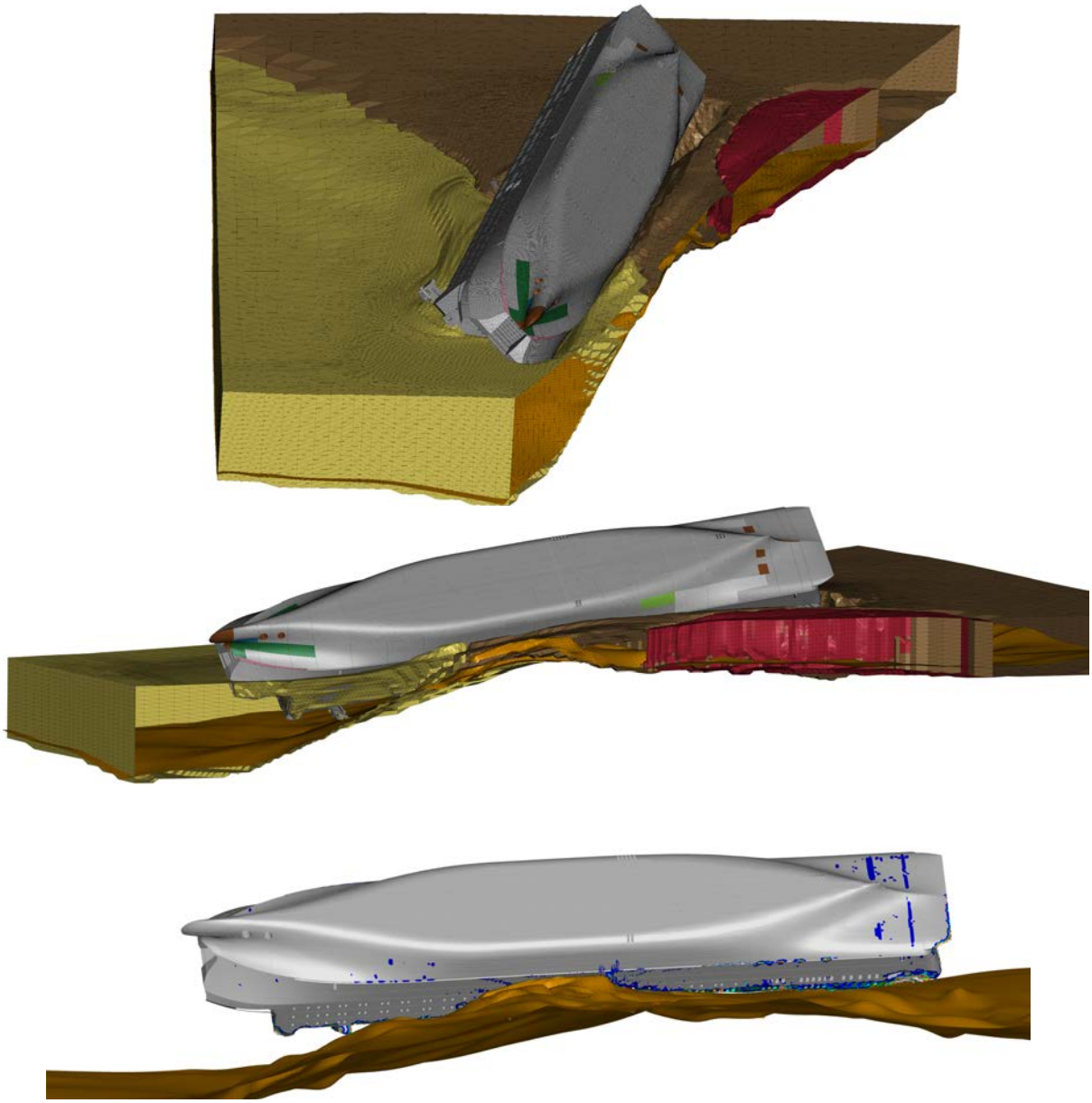

Figure 29. Ship's position at the bottom and the support from the soft clay and the acoustic basement (*above and middle*: deformations in soft soil are visualized*; bottom*: soft soil is removed for better overview).

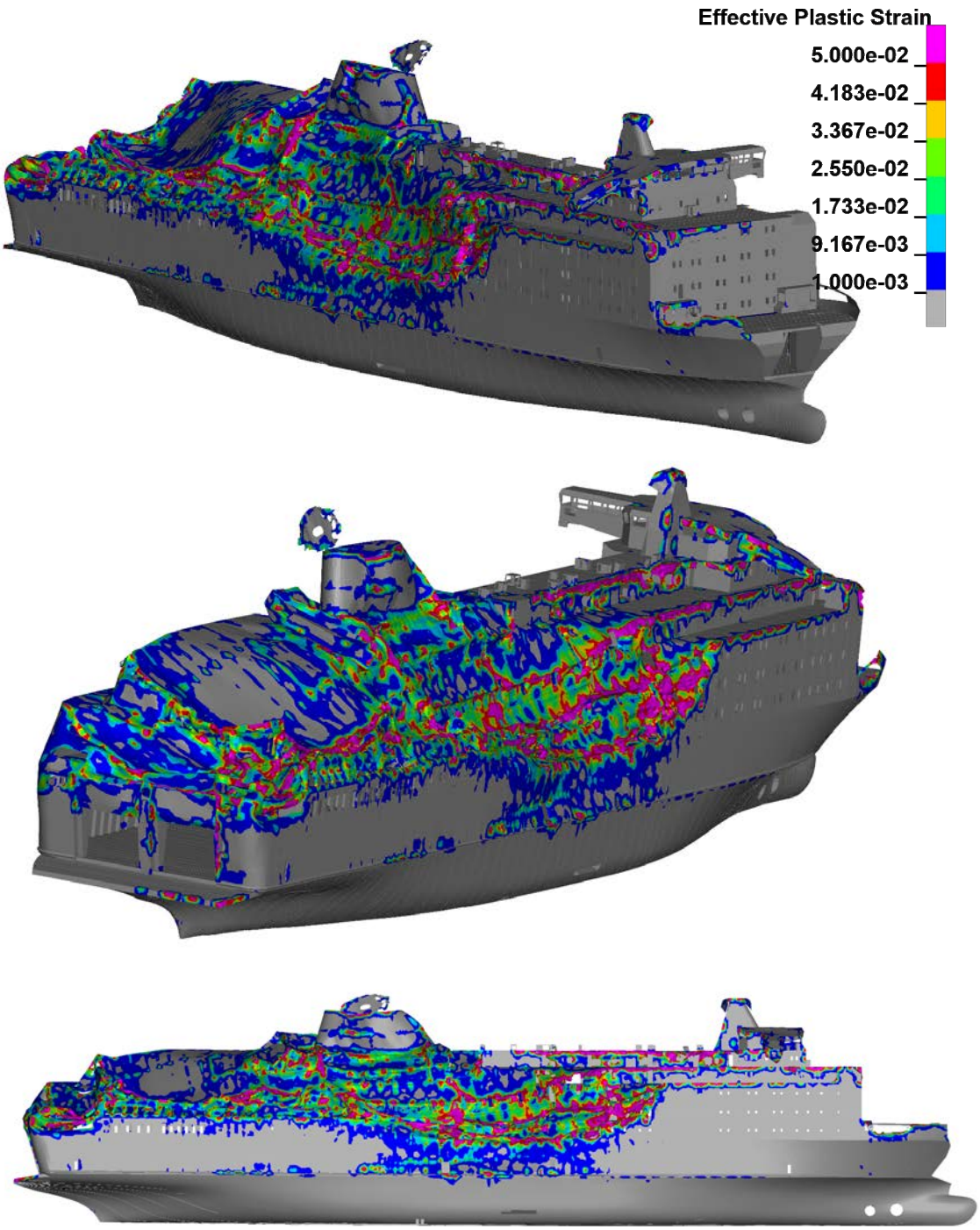

Figure 30. Deformation damage due to the bottom contact. Simulation ID10c (coarse mesh, roll 133 deg, acoustic bottom v3).

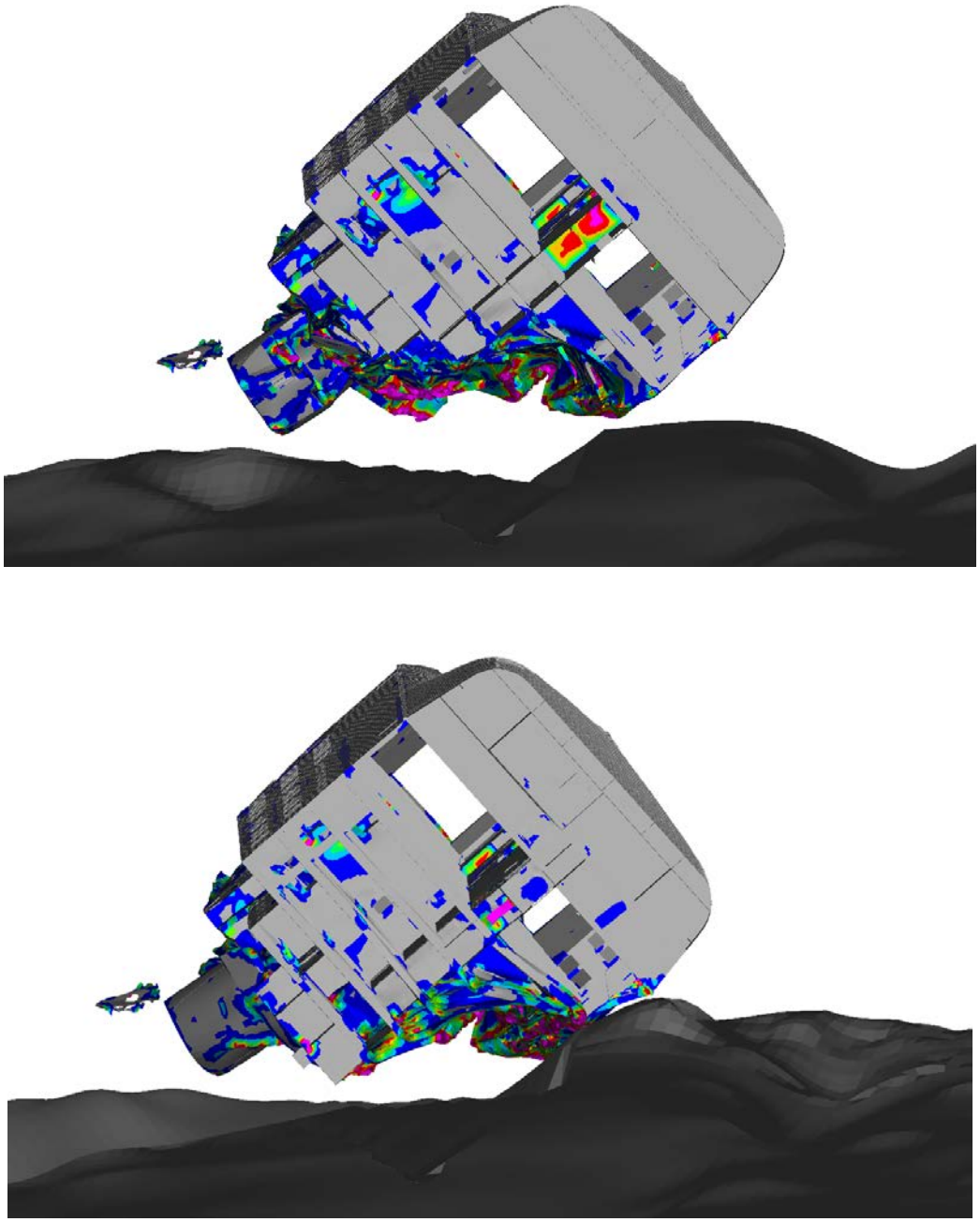

Figure 31. Deformation damage due to the bottom contact: view at the cross-section. Simulation ID10c (coarse mesh, roll 133 deg, acoustic bottom v3).

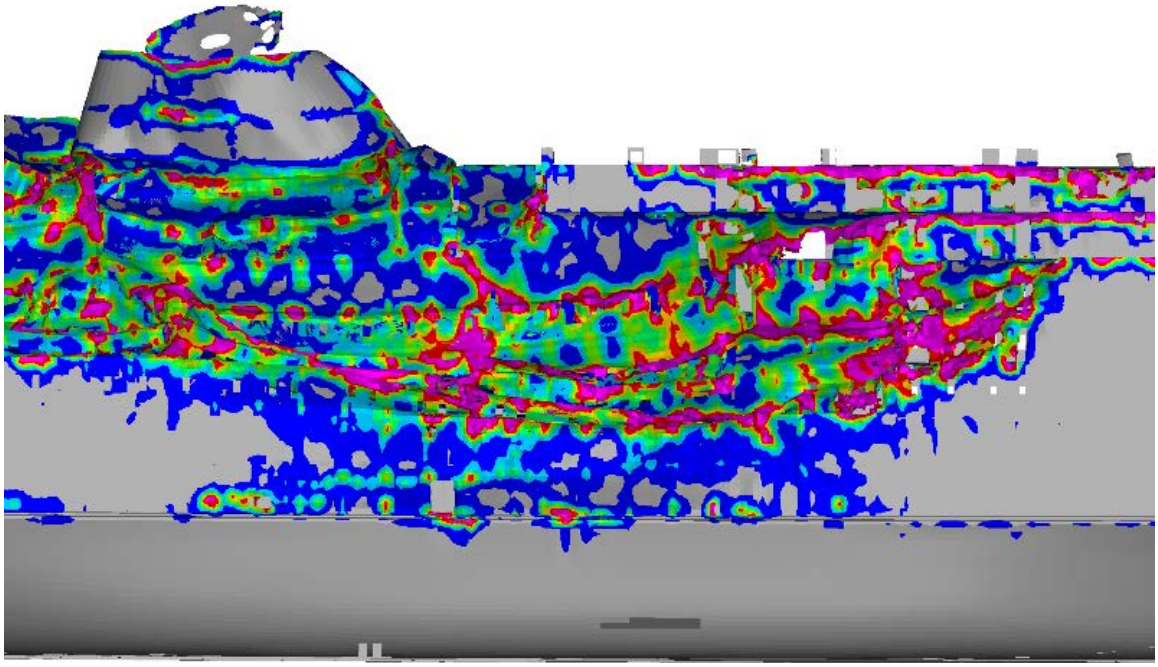

Figure 32. Deformation damage due to the bottom contact. Deformations at the ship side. Simulation ID10c (coarse mesh, roll 133 deg, acoustic bottom v3).

With smaller roll angle (113 deg, ID11c) the deformations to the upper decks are much less profound, and the side damage is more localized to the mid-ship region (Figure 33 to Figure 35). Starboard side of the upper decks at the aft of the ship are compressed, see Figure 33. The bridge is compressed at the starboard side. Due to more local contact, the deformation energy is focused to the midship region resulting in a long penetration damage as the ship side is thorn open, see Figure 35.

Vertically the deformation damage extends from below the fender guard until the upper deck, while the deformations in the upper decks are significantly lower compared to the simulations with larger roll angle of 133 deg.

From the deformations it can be concluded that as the ship becomes to the contact with the sea bottom in nearly statical manner, its mass is sufficient to cause severe structural damage. The damage pattern is sensitive to ships exact orientation with respect to the bottom. With larger roll angle (133 deg) significant portion of the deformation energy is absorbed by the crushing and folding of upper decks and less energy remains for the damage around the fender guard area. When the roll angle becomes smaller, the contact between the upper decks and soft soil is delayed and more energy is transferred through the contact between the rigid bottom and the ship, thus resulting in more localized and deeper deformation damage.

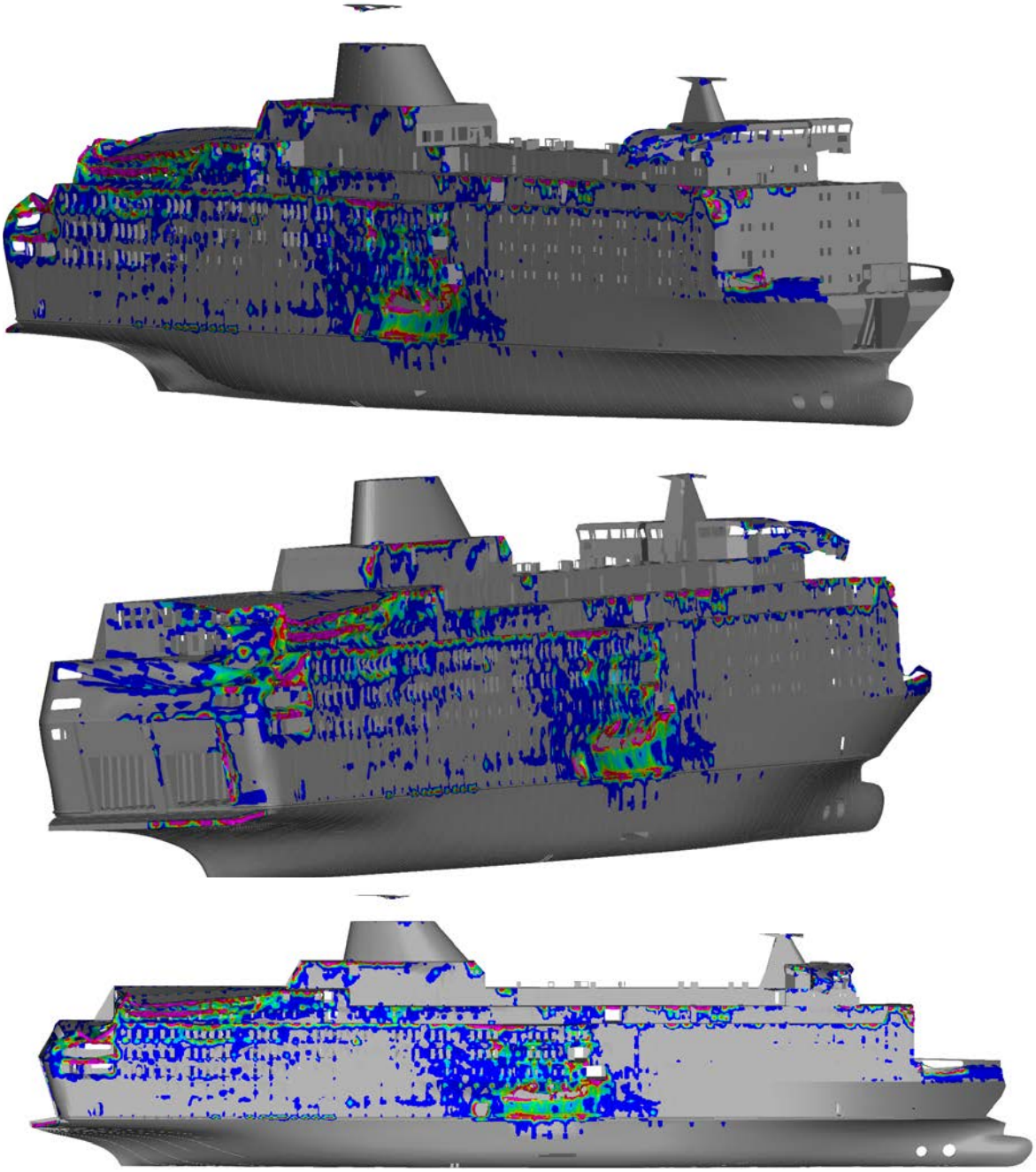

Figure 33. Deformation damage due to the bottom contact. Simulation ID11c (coarse mesh, roll 113 deg, acoustic bottom v3).

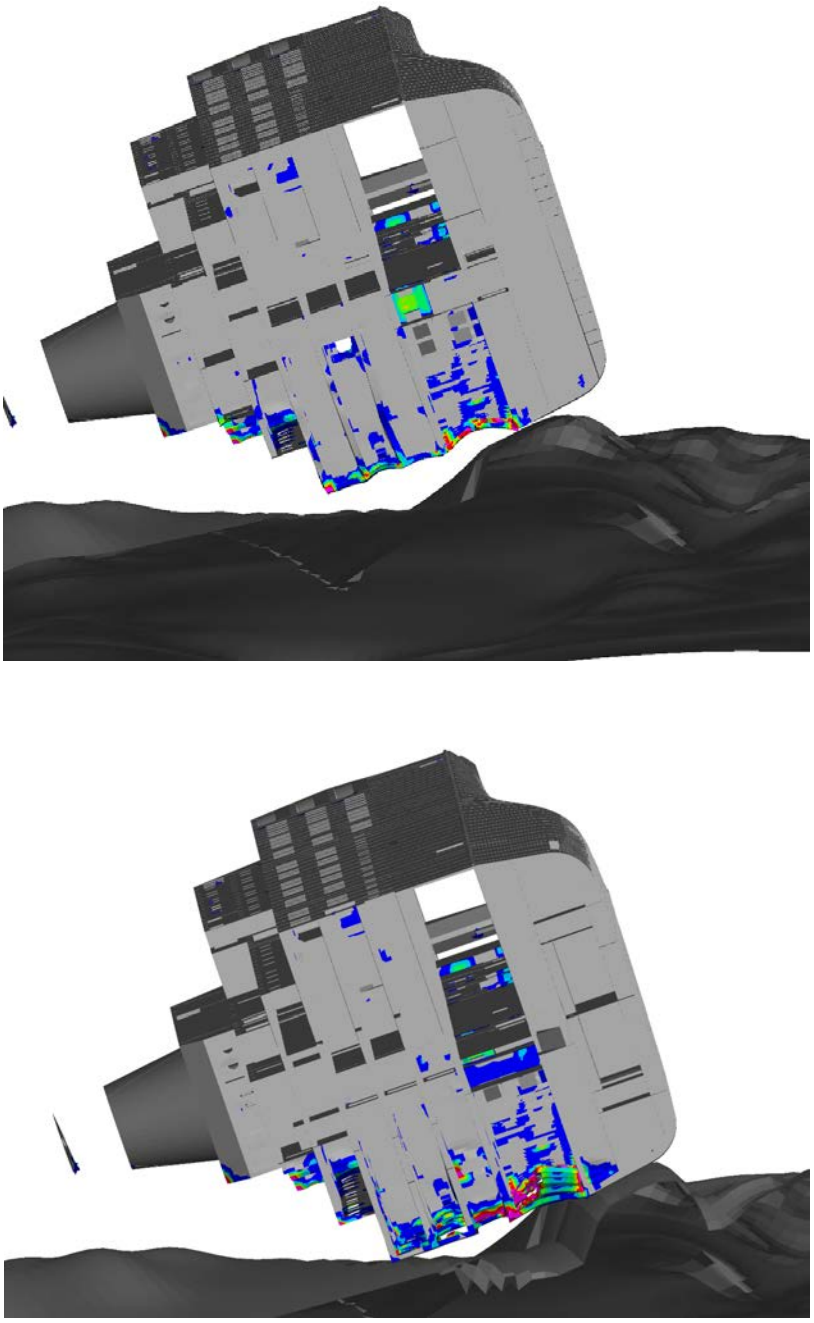

Figure 34. Deformation damage due to the bottom contact: view at the cross-section. Simulation ID11c (coarse mesh, roll 113 deg, acoustic bottom v3).

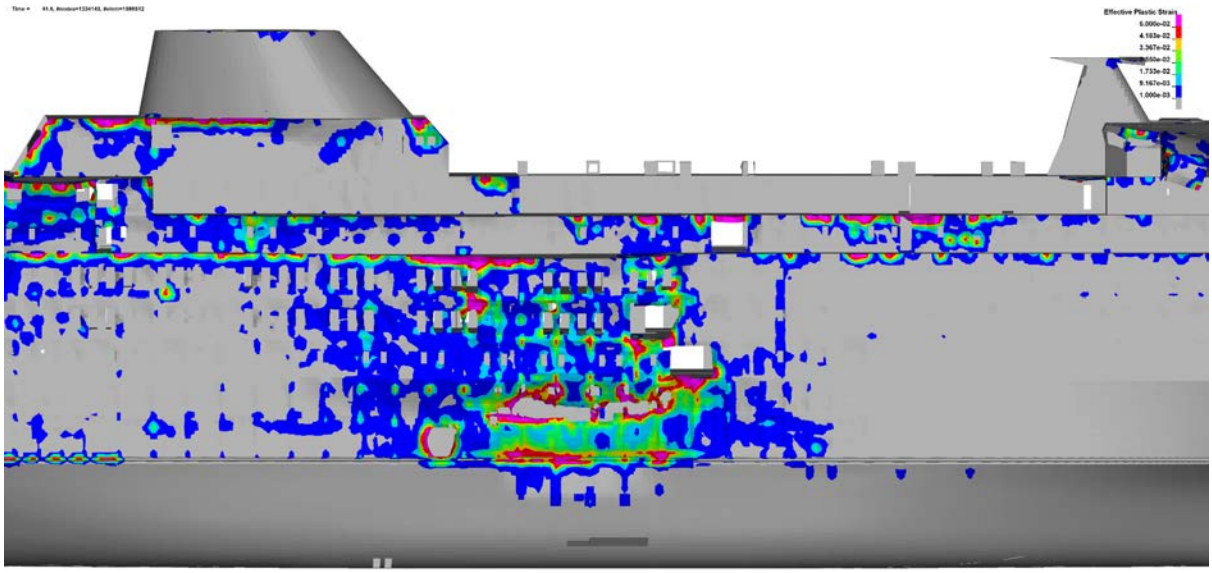

Figure 35. Deformation damage due to the bottom contact. Deformations at the ship side. Simulation ID11c (coarse mesh, roll 113 deg, acoustic bottom v3).

7.3 Comparison to the reported side damage openings

Simulated damages are compared to the damages reported at the shipwreck in Figure 36 to Figure 41. Fringe levels in the figures below present the permanent plastic deformations to characterize the structural deformations. The side damages recorded from underwater surveys are presented for comparison. The damage extent depicted at the profile of MS Estonia under the ESTLINE text is an input from Estonian Safety Investigation Bureau. The distance between the aft and the forward damage opening is about 25 m. As only part of the damage can be observed from the shipwreck, we compare the reported extent of the damage openings (red lines in the profiles of MS Estonia is subsequent figures) and compressions (orange lines in the profiles of MS Estonia is subsequent figures) in the shipwreck to the simulation results. From the shipwreck the structural damages are observed mainly at the level of the fence guard as the upper decks are hidden by the soft bottom.

In the simulations with roll angle of 133 deg and sharper acoustic bottom V3 (Figure 36 for coarse mesh model and Figure 37 for fine mesh model), the plastic deformations are concentrated to the midship region, while their extent slightly exceeds the visible damages in the shipwreck. In the case of coarse ship model in Figure 36 the simulated side damage openings in the hull roughly correspond to the reported damage openings in the shipwreck, even though they are positioned somewhat more towards the aft of the ship. For the fine mesh model in Figure 37 there is a small damage opening above the fence guard at the location of reported damage at the aft. There is no damage opening in the front, even though there is a clear deformation line forming that meets the fence guard at the location of the reported damage opening.

Deformed shape of the external hull plating above the fence guard is shown in Figure 38 for the coarse mesh model. The side plating is pushed in, and the damage openings occur adjacent to web-frames, which act as strong supports points initiating stress concentrations. The view from inside the ship is shown in Figure 39 for the fine mesh model. The buckling of the lower ends of the side stiffeners and web frames at the level of the car deck is clearly visible. Moreover, the fracture damage at the car deck next to the external hull can be observed.

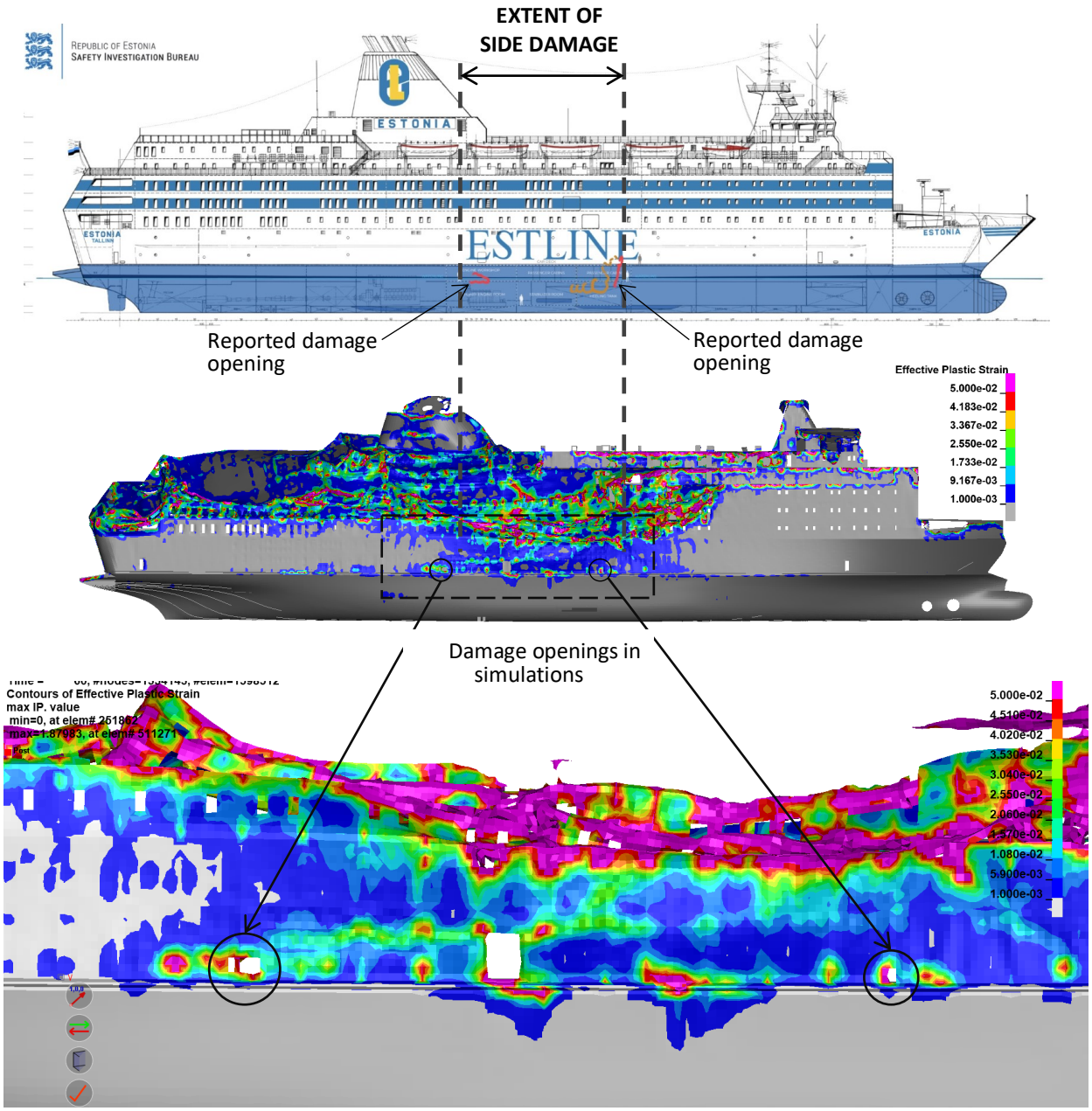

Figure 36. Comparison of side damages with respect to the reported damages. Simulation ID10c (coarse mesh, roll 133 deg, acoustic bottom v3).

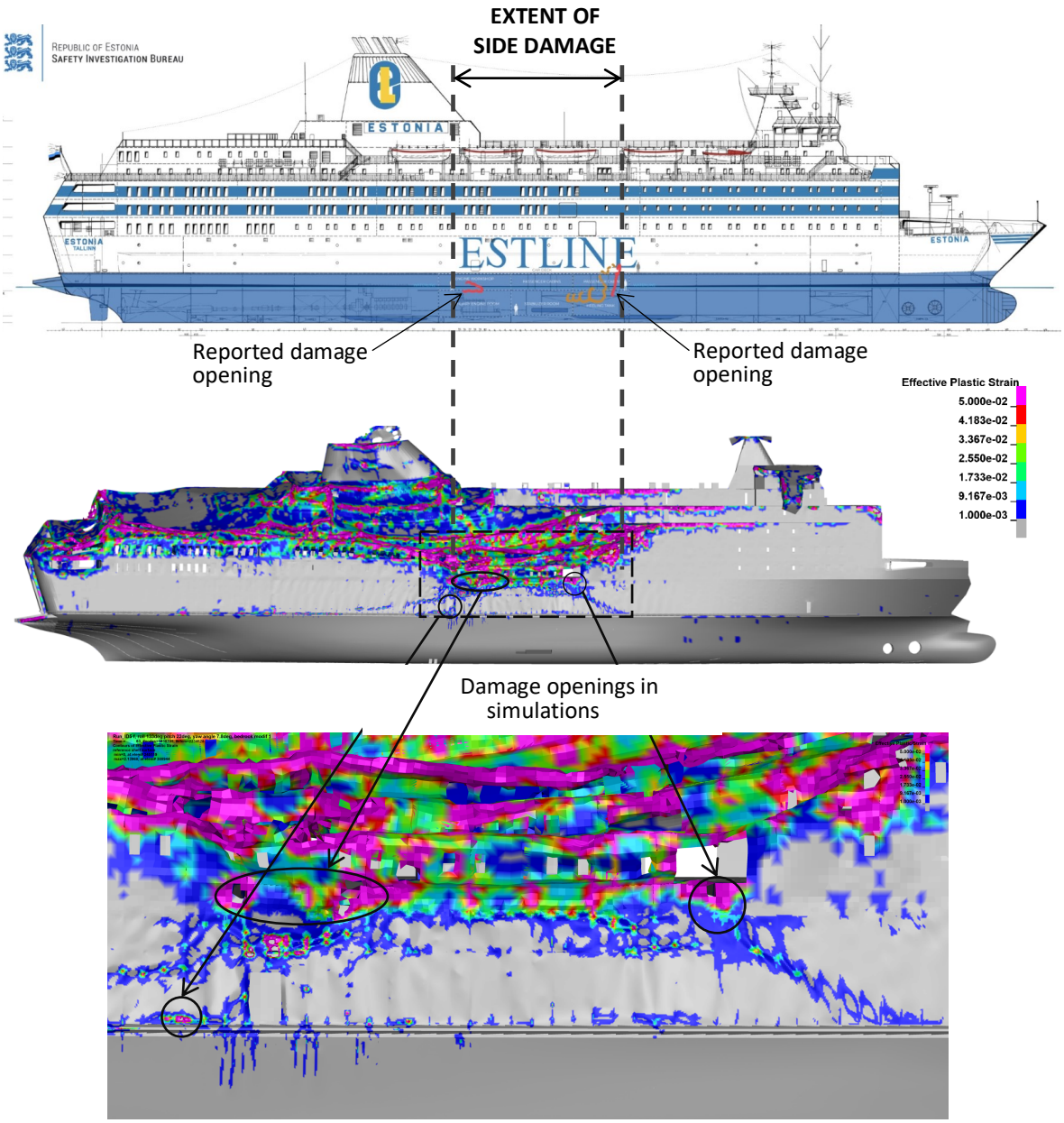

Figure 37. Comparison of side damages with respect to the reported damages. Simulation ID5f (fine mesh, roll 133 deg, acoustic bottom v3).

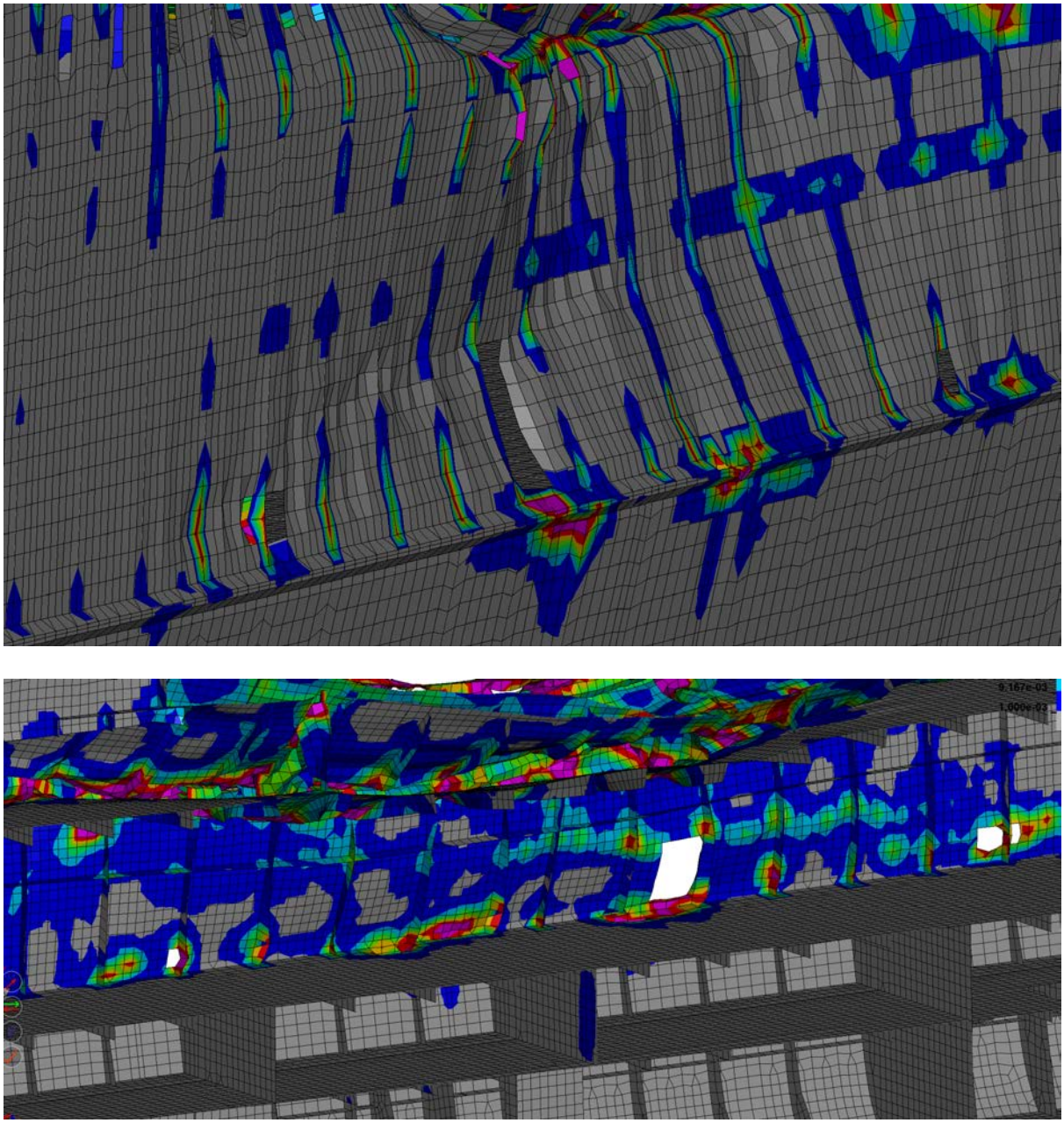

Figure 38. Deformed shape of the ship hull (*above*: a view from outside; *below*: a view from inside). Simulation ID10c (coarse mesh, roll 133 deg, acoustic bottom v3).

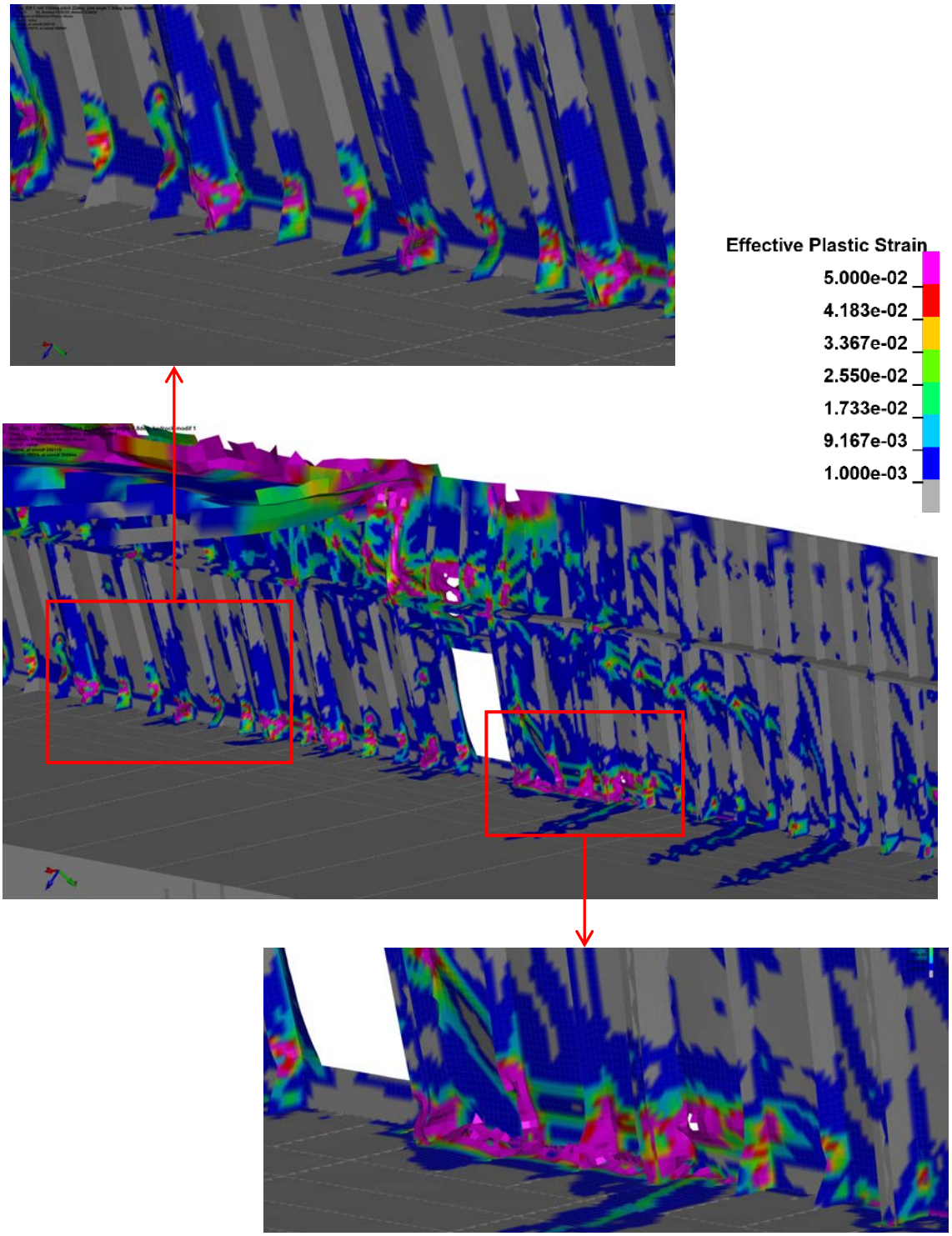

Figure 39. A view from inside above the car deck to visualize the deformation of the stiffeners and web frames, and the fracture damage at the car deck plating. Simulation ID5f (fine mesh, roll 133 deg, acoustic bottom v3).

For smaller initial roll angels in Figure 40 (acoustic bottom v3) and Figure 41 (acoustic bottom v1), the damage is more localized and contact results in rather long and large side opening. In both cases the side openings are within the boundaries of reported side damages of the

shipwreck. With smoother bottom v1, the damage extends further below the fender guard compared to the sharper bottom. Effect of the shape of the acoustic basement is discussed further in the next section.

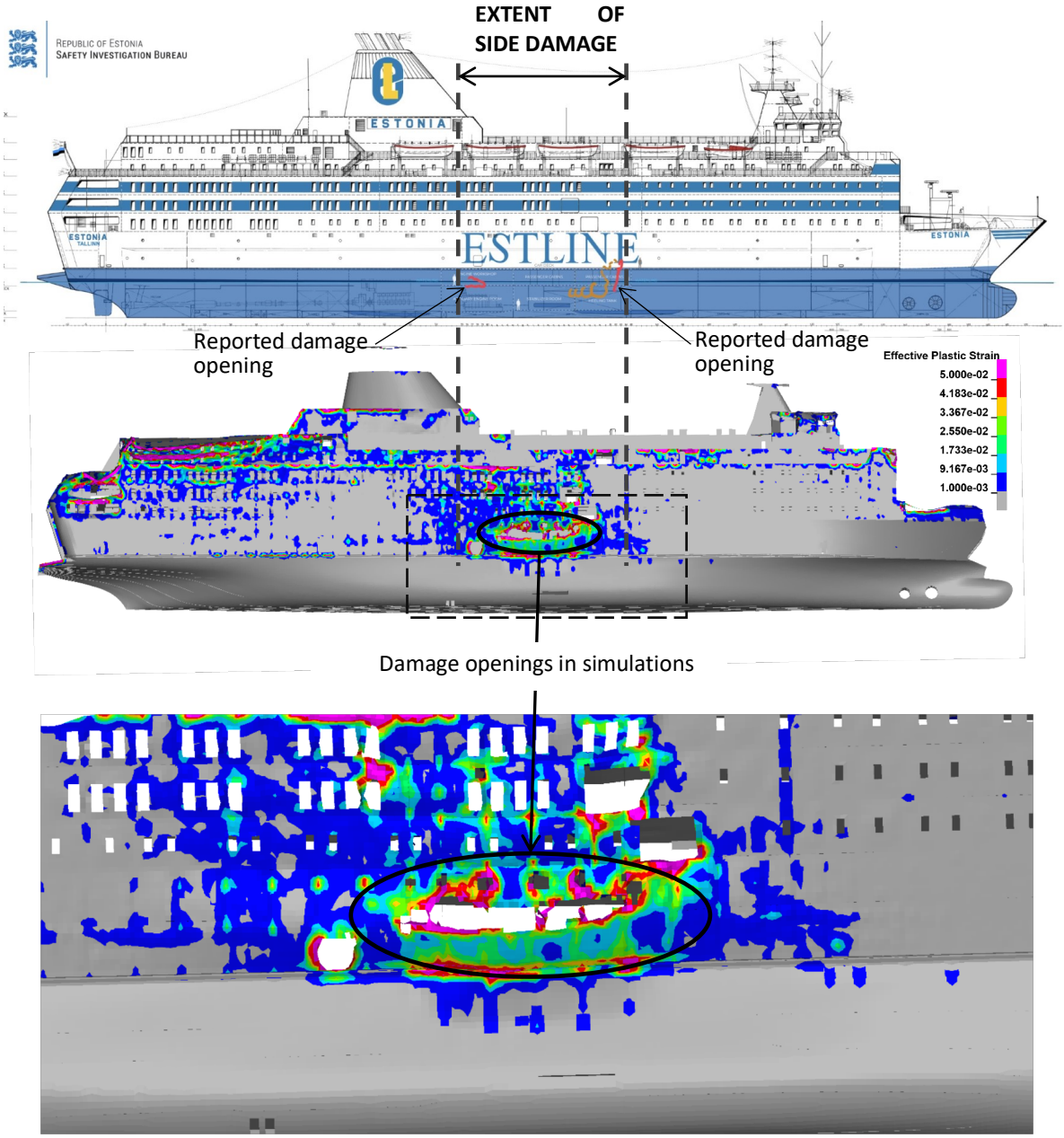

Figure 40. Comparison of side damages with respect to the reported damages. Simulation ID11c (coarse mesh, roll 113 deg, acoustic bottom v3).

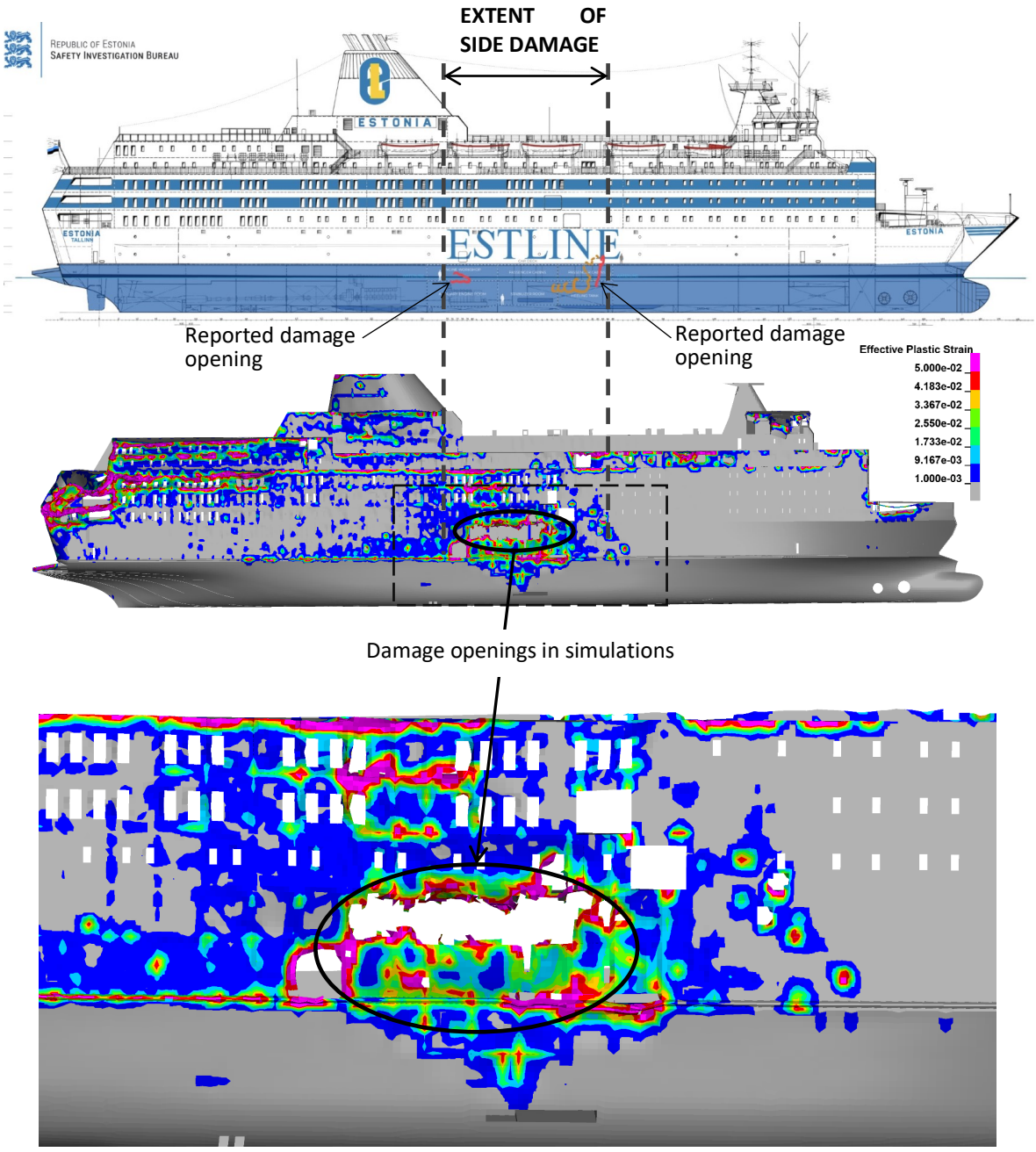

Figure 41. Comparison of side damages with respect to the reported damages. Simulation ID8c (coarse mesh, roll 113 deg, acoustic bottom v1).

7.4 Global deformations of the ship hull

To visualize the global deformations of the ship hull, the intact and undeformed ship model is overlayed with the photogrammetric model of the shipwreck by the Estonian Safety Investigation Bureau. Bilge keels are used as a reference to align the models.

The global deflection of the shipwreck is clearly visible in Figure 42 – the midship is pushed out of the original dimensions towards the port side and the bow and stern have deflected towards the starboard. Global deflection can also be observed when assessing the position of the bulbous bow and the ducktail. Both have deflected towards starboard and slightly towards upper decks.

It is hard to observe the global deformations from the numerical model as the deflections do not appear obvious without the reference surfaces, even though the attempt has been made in Figure 43. Parallel reference lines are drawn from the fence guard until the Deck 7. It can be seen that the deck levels deviate from the reference lines and the deviation increases for upper decks indicating slight bending of the hull. The bending increases for upper decks.

However, the loading condition of the ship hull girder becomes more obvious when looking at the longitudinal stresses in Figure 44. The port side of the ship is under tensile loads and the starboard side is under compressive loads (except the heavily deformed region above the fence guard, which is under tensile stresses). Such stress distribution indicates that the ship hull has been bent towards the starboard, similar to the condition indicated with the overlay in Figure 42.

Figure 42. Hull deflection at the port side (*above*) and at the bow (*below*). (Overlay of the intact ship with the photogrammetric model of the shipwreck in provided by Estonian Safety Investigation Bureau)

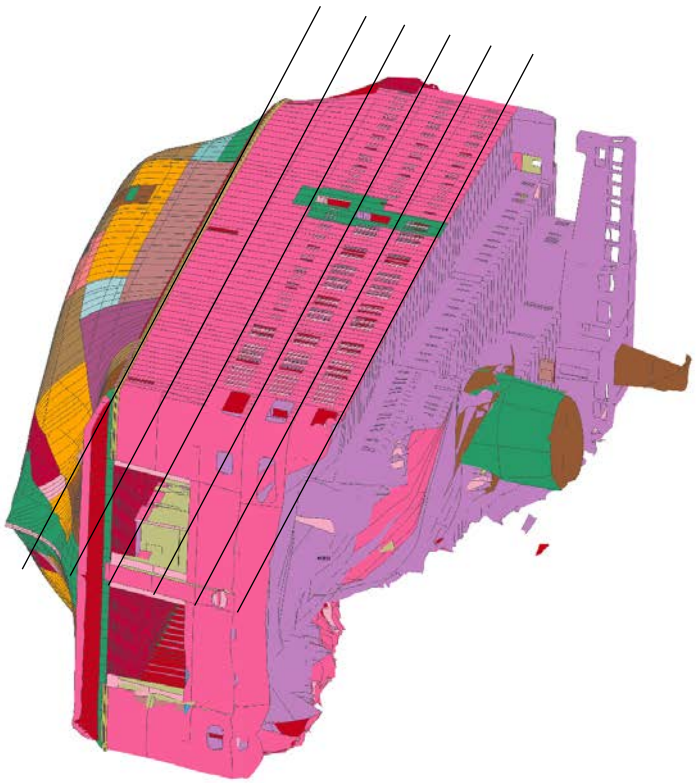

Figure 43. Global bending deformation of the ship hull (ID5f). Deviation of the deck levels from the reference lines. Simulation ID5f (fine mesh, roll 133 deg, acoustic bottom v3).

At the Deck 7, there is a clear outward bending of the external hull plating, see Figure 45. In simulations in Figure 46, this effect is barely noticeable even though there are clear strain peaks at the intersection between the deck girders and the external plating. The deformations at the aft of the ship are comparable to those observed at the shipwreck. Numerical simulations presented here are conducted with finite element models where the aft part of the ship is modelled using relatively coarse mesh. Thus, the response of the web frames in the aft ship region is too stiff to capture such relatively local phenomenon. A finite element model *Fine mesh model 2* has been developed (Figure 21) with the purpose to assess this damage. Finer mesh resolution at the upper decks would allow to capture such local effect. Such simulations are still to be conducted.

Deformation of the bridge at the port side can be observed from Figure 47. The port side of the bridge is pushed down indicating that the whole structure directly under the bridge has collapsed. Deformations in the starboard side cannot be observed as the bridge is hidden under the soft soil. In the simulations (below in Figure 47) there is extensive deformation at the starboard side of the bridge, while the collapse of the structure under the bridge has not occurred.

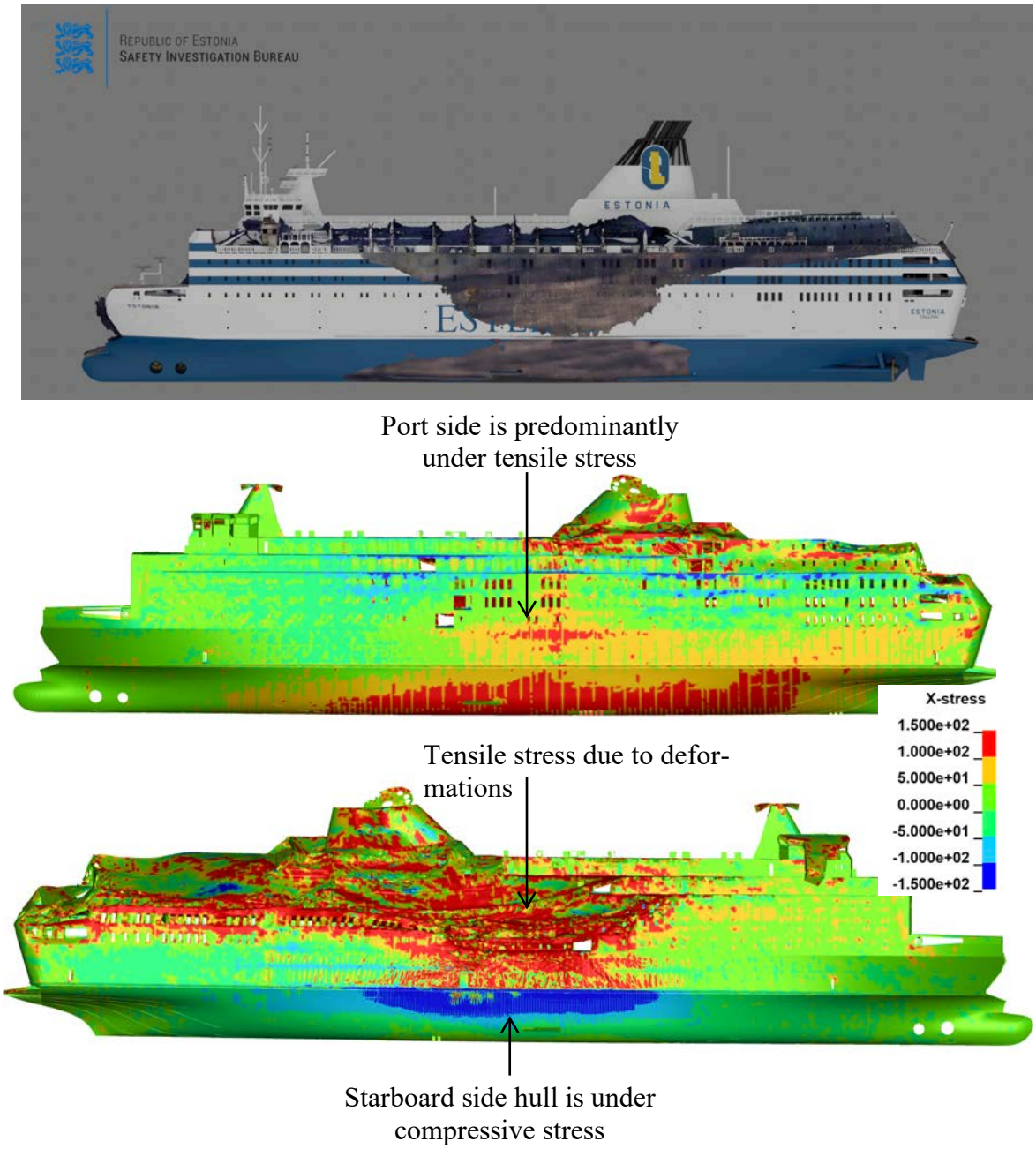

Figure 44. Longitudinal stresses in the ship hull (stresses in MPa, positive stress indicates tension and negative stress indicates compression). Simulation ID5f (fine mesh, roll 133 deg, acoustic bottom v3).

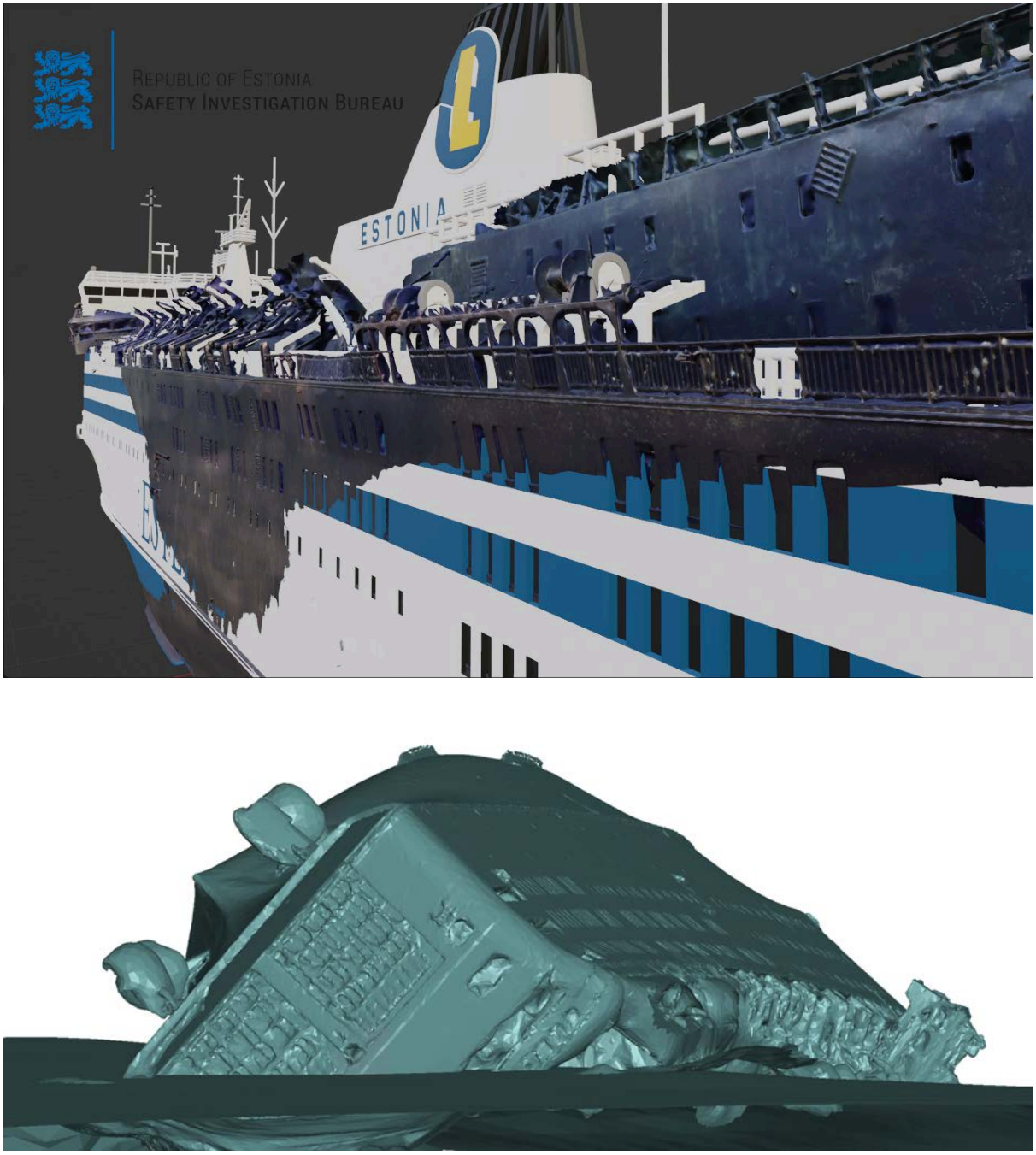

Figure 45. Outward deformation at the port side of Deck 7.

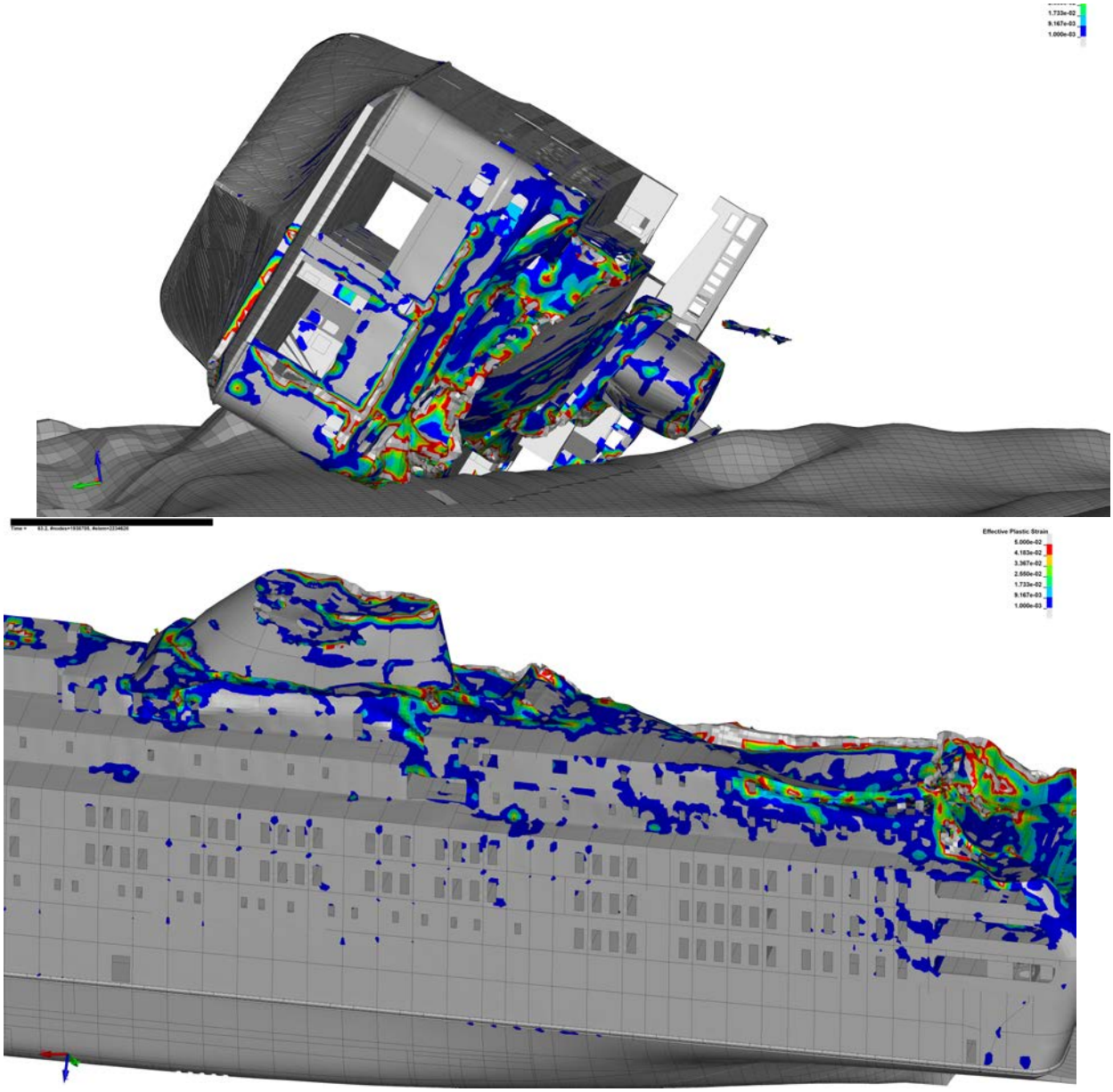

Figure 46. Simulated deformations of the aft section of the ship. Simulation ID5f (fine mesh, roll 133 deg, acoustic bottom v3).

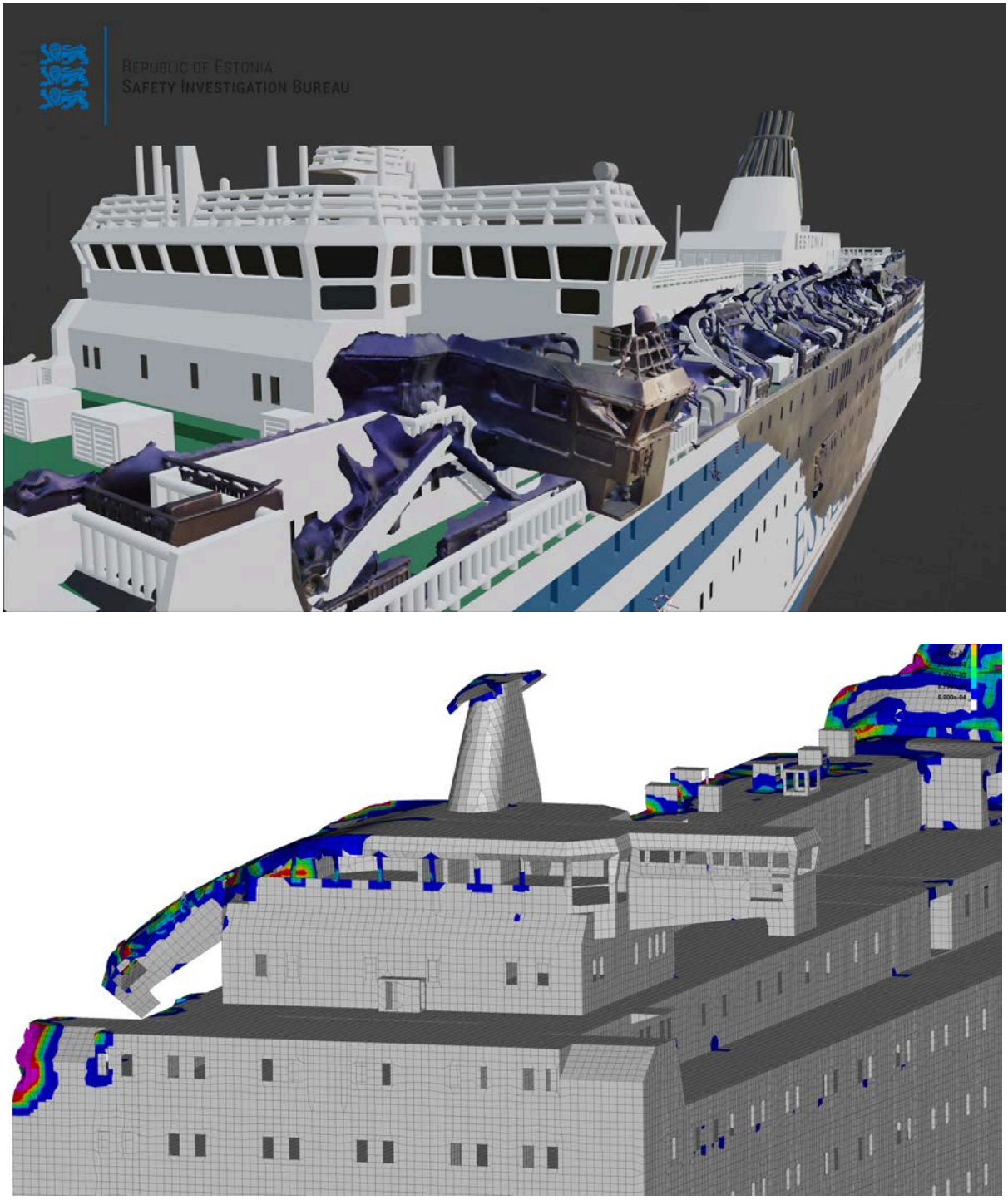

Figure 47. Deformations of the bridge (*above*: overlay; *below*: simulations). The port side of the bridge is bent downward. The structure directly under the bridge appears to be collapsed.

7.5 Effect of the shape of the acoustic bedrock on side damage

As discussed in Section 4.1, directly under the shipwreck there is no measured data about the shape of the acoustic bedrock and thus, two shapes are assumed as shown in Figure 10. The effects of these shapes are presented in Figure 48 and Figure 49.

As the ship slides over the protruding acoustic bedrock and as the cap between the ship and acoustic bedrock is filled with soft sea bottom, the effect of the shape of the acoustic bedrock

does not have remarkable influence on the ship's overall deformation damage (Figure 48). When looking at the local damages the differences are somewhat larger as the size of the damage openings is slightly different, see Figure 49 and Figure 50. Smoother bottom V1 results in slightly wider damage opening as the sharper shape V3 applies more localized pressure and thus, the results on more localized damage. Steeper and sharper bottom shape V3 allows larger rotation for the ship at the bottom and thus, results in more complex interaction between the ship, soft bottom consisting of glacial clay and the acoustic bedrock.

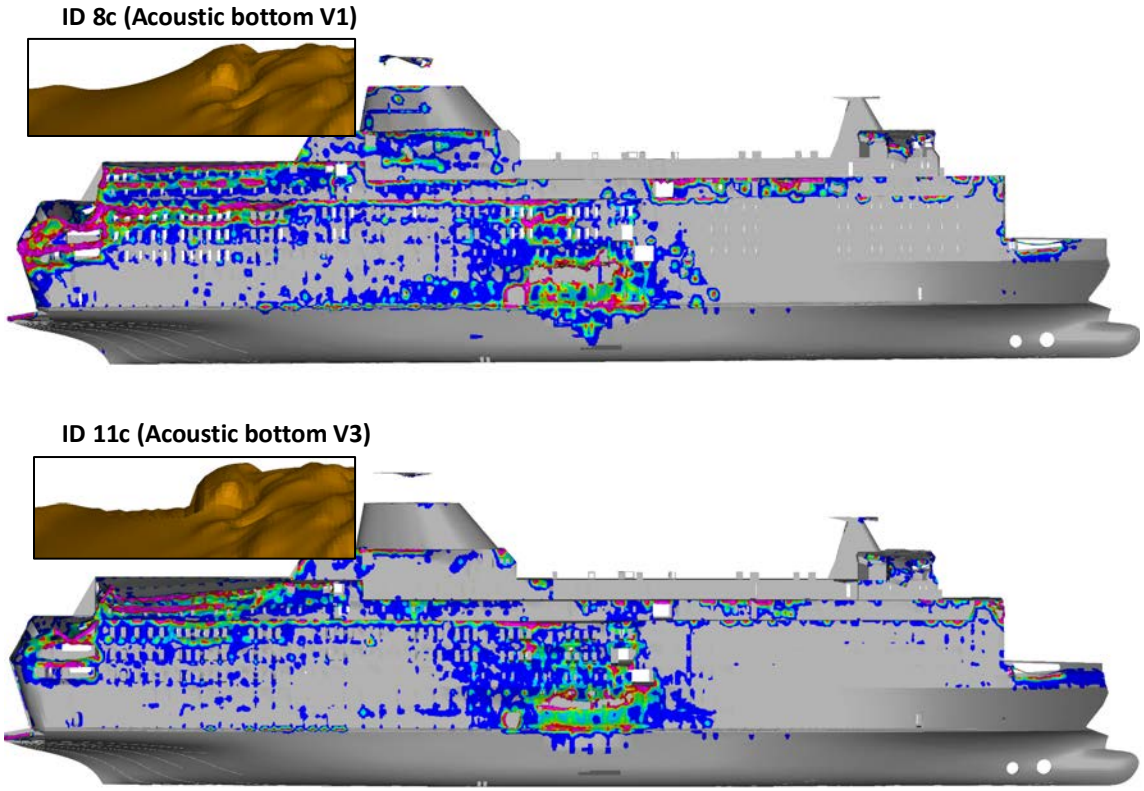

Figure 48. Effect of the shape of the acoustic bedrock on the side damage (ID8c vs ID11c).

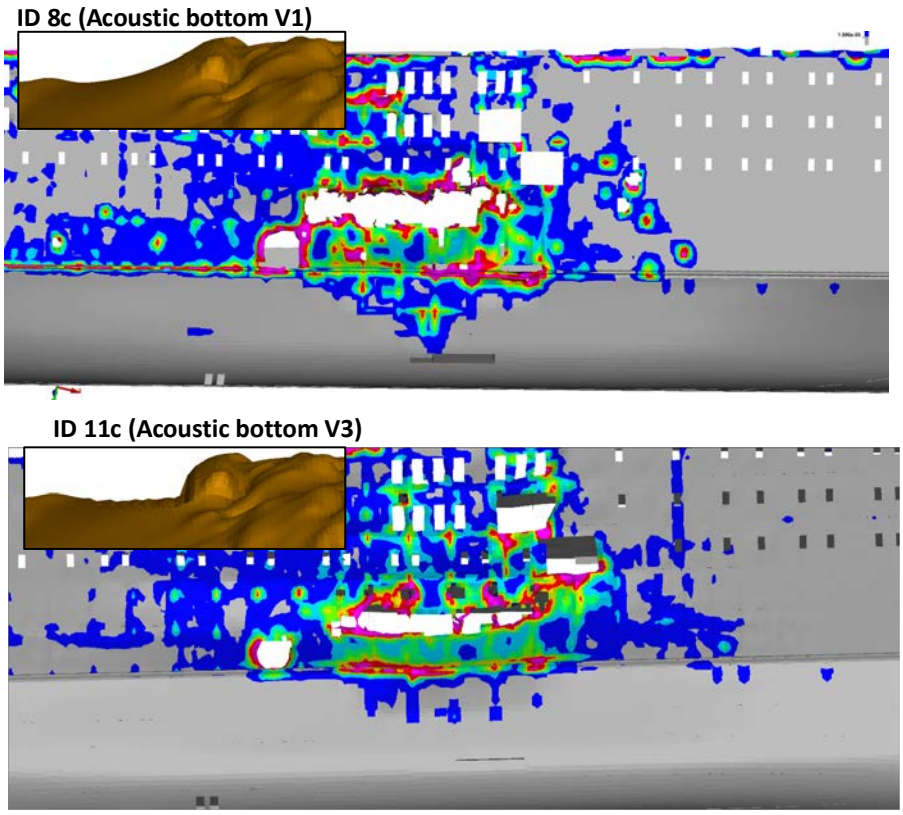

Figure 49. Effect of the shape of the acoustic bedrock on the side damage: size of the damage openings (ID8c vs ID11c).

From the deformations and damage openings it can be concluded that as the ship becomes to contact with the sea bottom in nearly statical manner, its mass is sufficient to cause severe structural damage. The damage pattern is sensitive to ships exact orientation with respect to the bottom. With larger roll angle (133 deg) significant portion of the deformation energy is absorbed by the crushing and folding of upper decks and less energy remains for the damage around the fender guard area. When the roll angle becomes smaller, the contact between the upper decks and soft soil is delayed and more energy is transferred through the contact between the rigid bottom and the ship, thus resulting in more localized and deeper deformation damage.

The shape of the acoustic basement has only local effect on the deformations and does not significantly affect the overall contact process.

With the ship supported by the acoustic bottom in the midship region, the simulated damages also achieve maximum in this region. The location of most extensive damages in the simulations corresponds well to the location of side damages at the shipwreck. Roll angle of the ship and its exact position with respect to the bottom defines the exact location on the ship hull where the deformation damage concentrated. Moreover, it is expected, even though not yet fully assessed, that the stiffness of the soft soil can influence the deformation pattern on the ship hull.

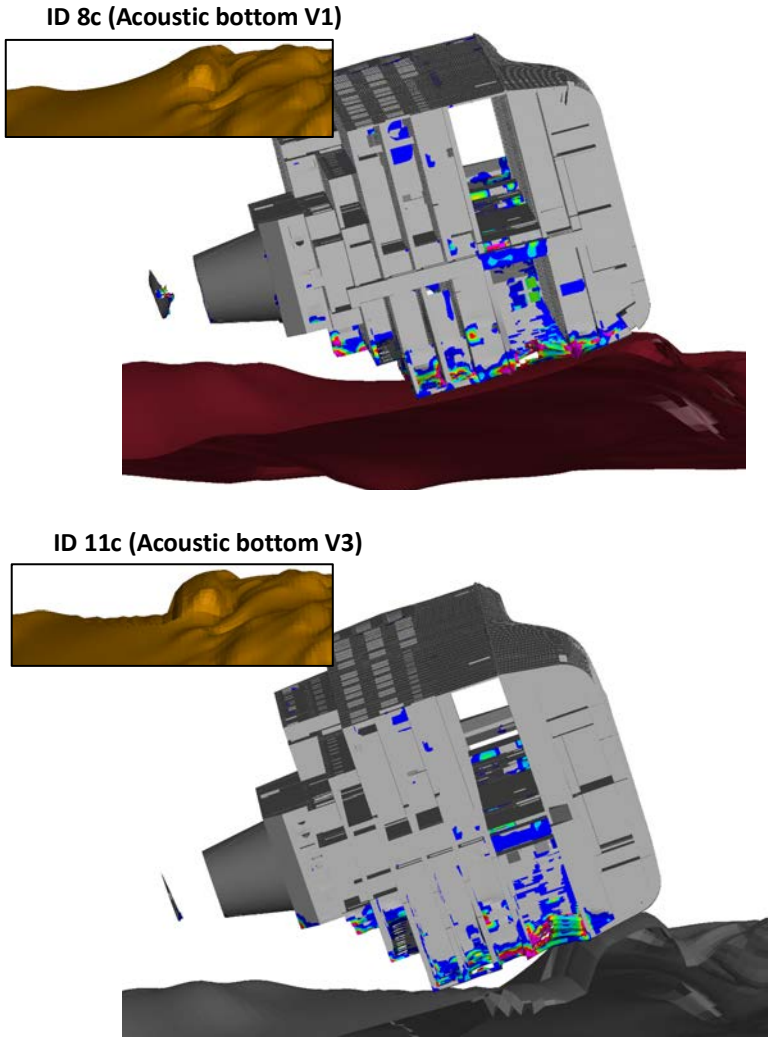

Figure 50. Effect of the shape of the acoustic bedrock on the side damage: deformations at the cross-section (Id8c vs ID11c).

8. ANALYSIS OF THE DEFORMATION AT THE FLAT BOTTOM OF THE SHIP

Underwater surveys have revealed a T-shape uniform deformation at the flat bottom of the shipwreck, see Figure 51. With current assumptions and initial conditions, this part of the ship never came to the contact with the sea bottom. Numerical assessment was conducted to explain the causes of this deformation damage.

The shape of the deformation is relatively uniform and has straight and clear boundaries. This suggests that the dent is due to the uniform (hydrostatic) pressure rather than due to the contact. This chapter studies the hypothesis, whether such deformation could occur due to increasing water pressure as the ship sunk towards the seabed.

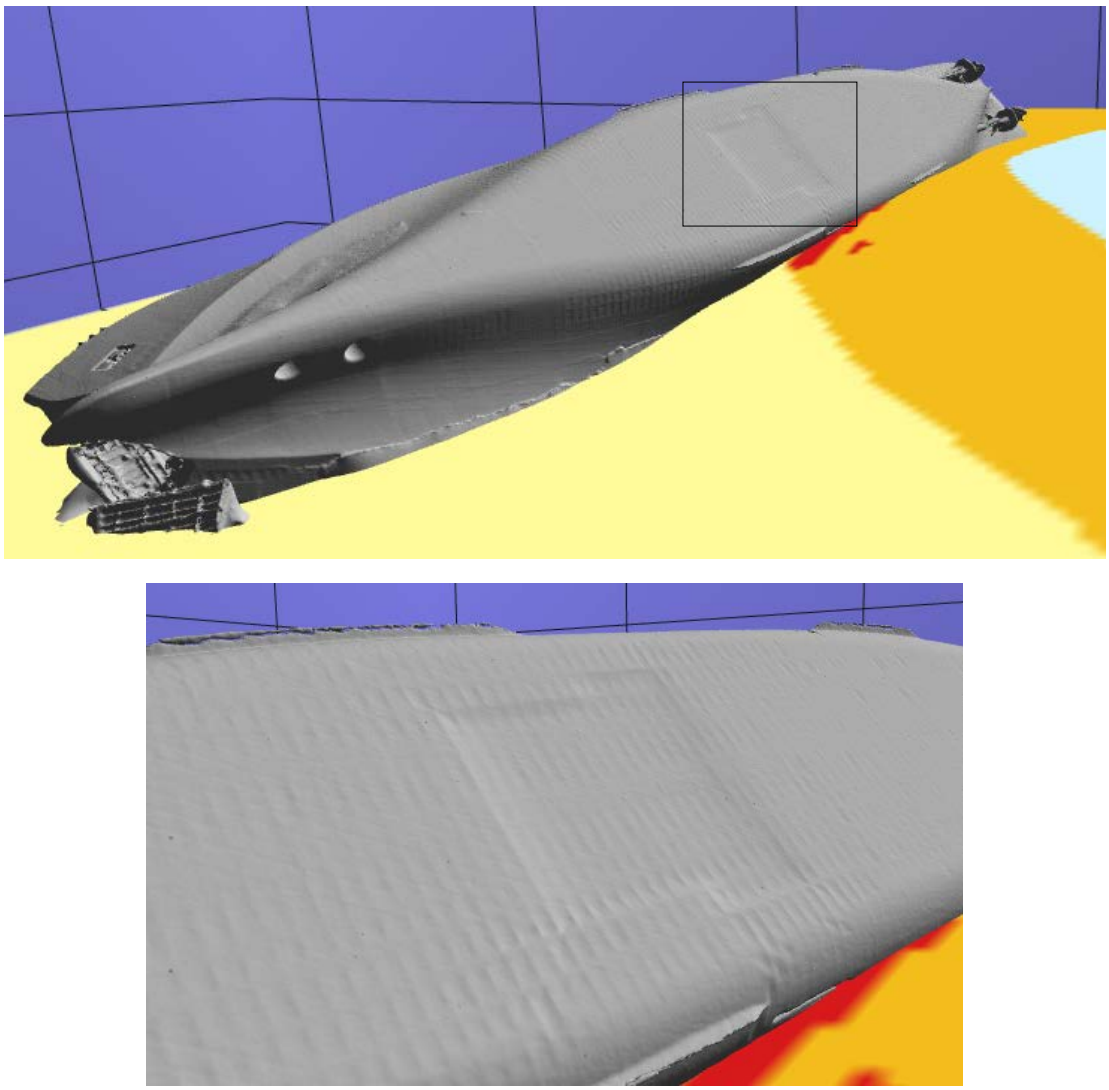

Figure 51. Flat bottom deformations of the shipwreck- a T-shaped dent in the mid-ship region.

8.1 FE analysis model

As the ship was still floating, it was already progressively flooded with seawater. In the analysis water pressure is applied to the bottom and to the Deck 1 (tween deck) of the ship, see

Figure 52. Pressure is applied over the whole compartment. This application of pressure mimics the situation, where the water has reached to the Deck 1, but in the studied compartment, the space between the Deck 1 and the ship bottom is still watertight and holds an air pocket.

The pressure is gradually increased until it reaches the maximum value 0.68 MPa -sea pressure at depth 68 m (wreckage depth). Increasing pressure simulates the increasing seawater pressure as the ship falls deeper towards the seabed. Plating thicknesses are shown in Figure 53.

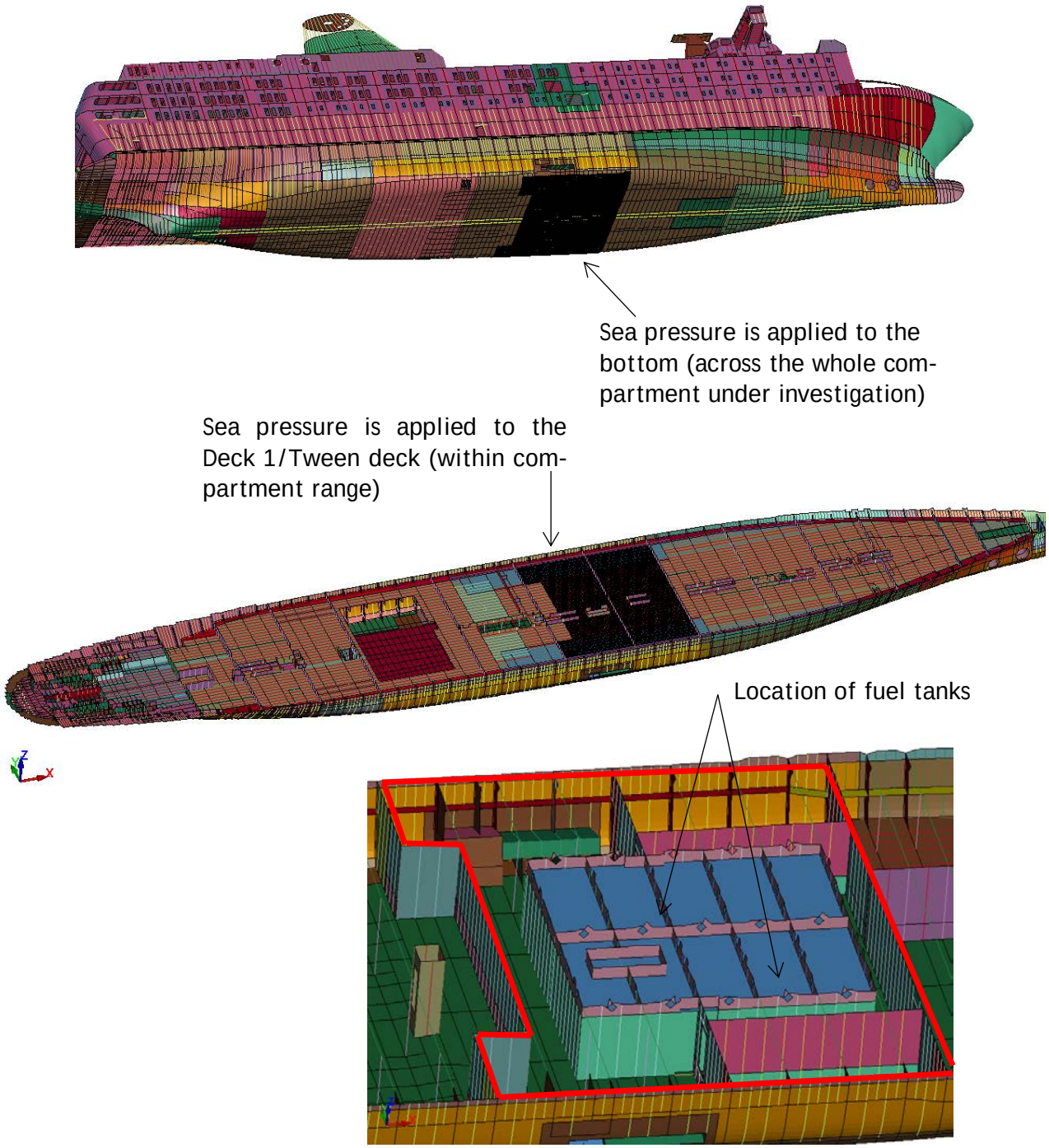

Figure 52. Pressure applied to the ship.

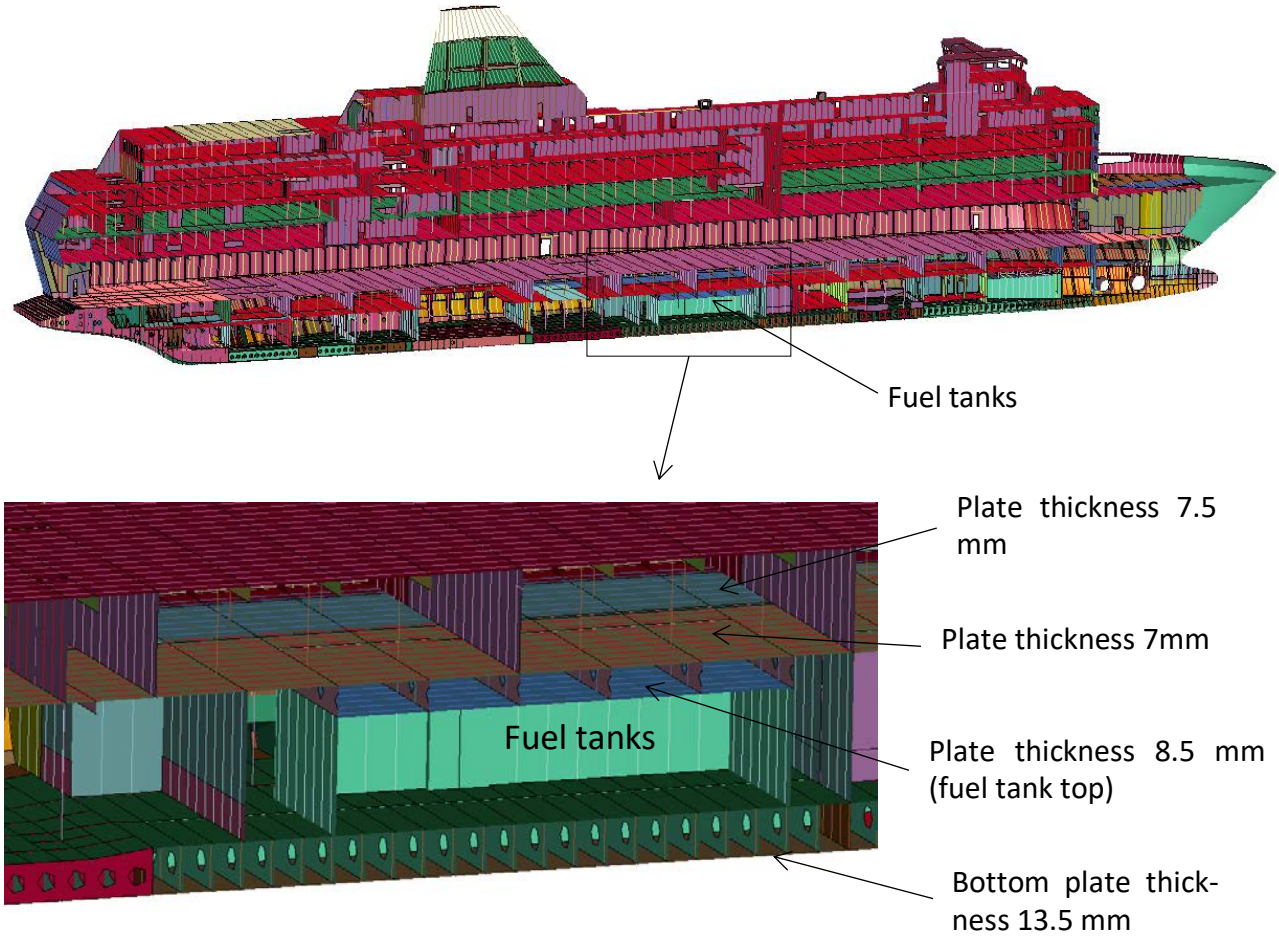

Figure 53. Plating thicknesses in the region of interest.

In the analysis model the nodes located on the outer edges of the car deck are set to fixed, i.e all degrees of freedom are constrained, see Figure 54.

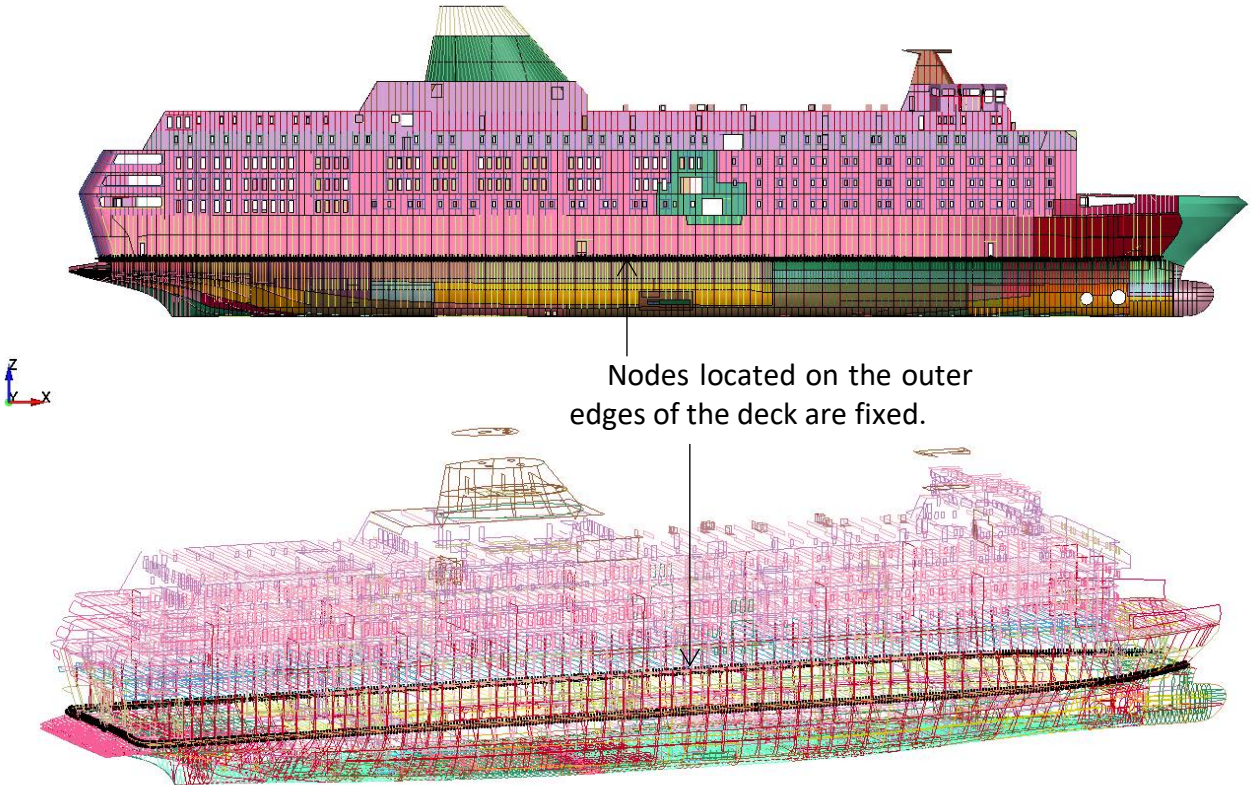

Figure 54. Boundary conditions.

8.2 Results of the bottom buckling assessment

In Deck 1, the material failure occurs when the sea pressure reaches to 0.35 MPa that corresponds to water depth of 35 m, see Figure 55. The bottom plating is still intact and barely deformed. The failure of the Deck 1 develops rapidly, and the material failure expands into several meters in less than a second, see Figure 56. Due to the failure, the structural elements between the Deck 1 and the bottom loose their load carrying capability due to buckling. The buckling of the outer bottom follows shortly as seen in Figure 56. The buckling shape at the bottom corresponds very well to the one observed at the wreckage. The time between the failure of Deck 1 plating and the buckling of the bottom plating is too short for the entrapped air to leave the compartment.

Thus, it can be concluded that the buckling shape is due to the external water pressure, and a compartment above this buckled region was still airtight and contained an air pocket at the water depth of about 35 m. The buckling of the outer plating followed shortly the failure of Deck 1 plating.

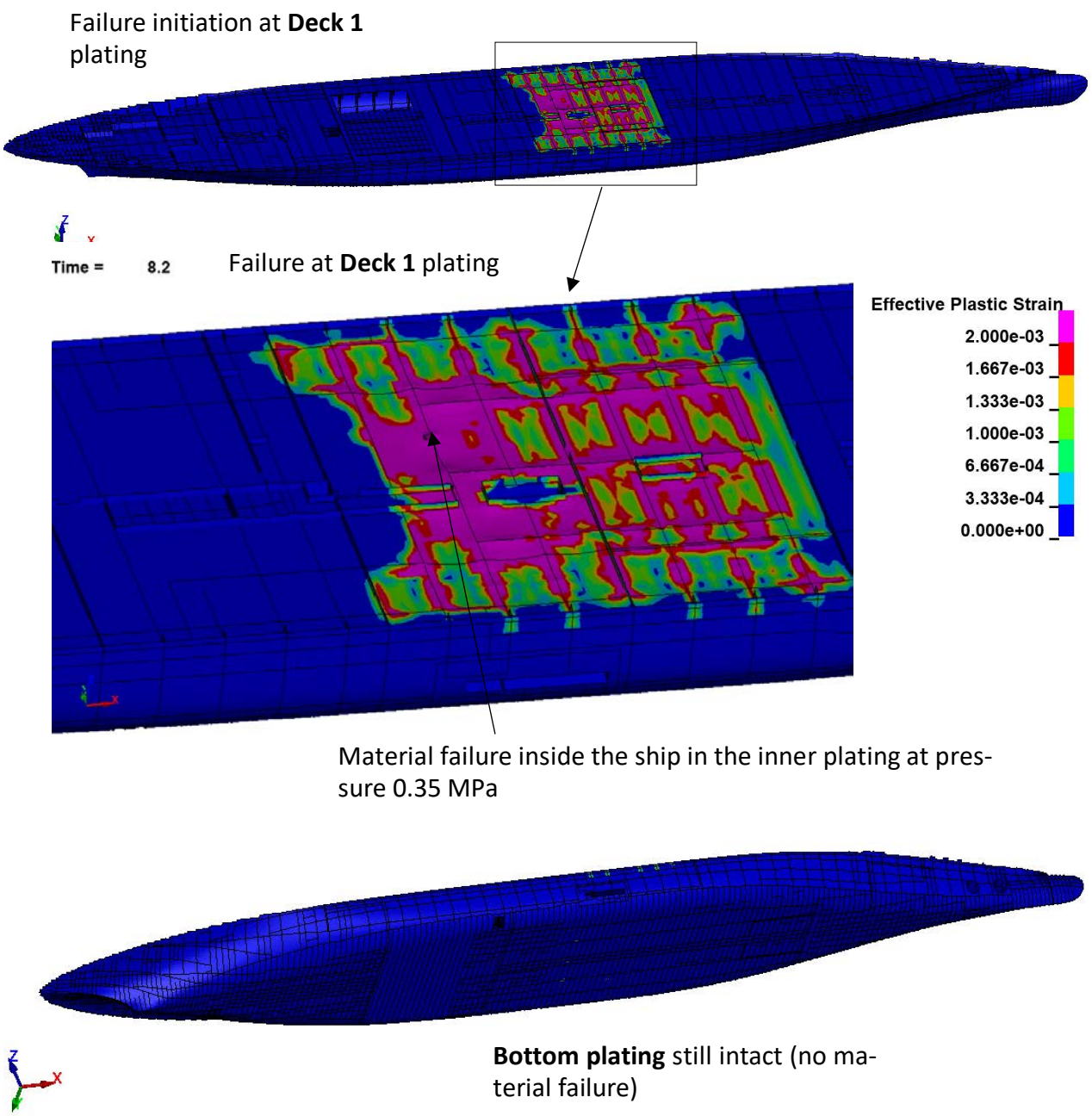

Figure 55. Material failure in Deck 1 plating at water depth of 35 m. Plastic deformations are shown.

Large-scale failure at **Deck 1** plating

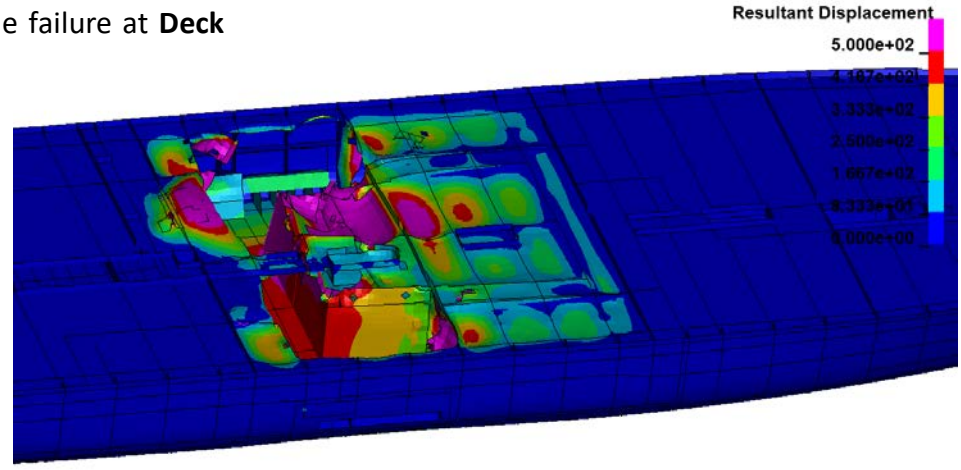

Buckling shape at the **Bottom plating**

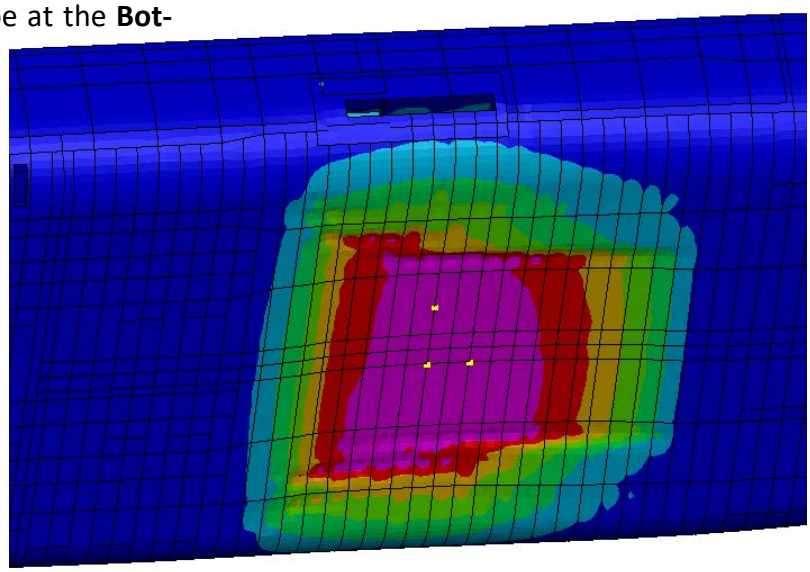

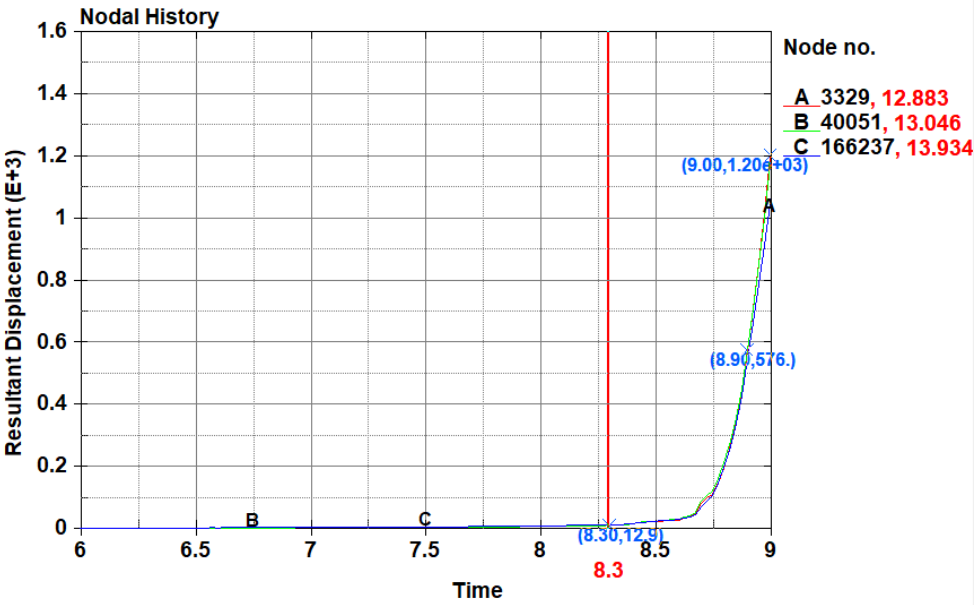

Figure 56. Failure of the Deck 1 plating and bottom deformations. Total translations shown.

9. CONCLUSION

Report presented the simplified model and the detailed numerical model that are used to simulate the descent and bottom contact of MV Estonia. Simplified model considers the significant hydromechanic loads as far as the level of simplifications allows. Simplified model provides a qualitative description of the ship descent towards the sea bottom. Main outcome of the simplified model are the ship motion dynamics during the descent.

Contact between the ship and the sea bottom is simulated in the detailed numerical model as precisely as the available input data allows. The model provides the description of ship's final position and structural deformations.

The following main conclusions are drawn:

- in the final position at the sea bottom the middle of the ship is supported by protruding bedrock, while its fore body is supported by post-glacial soft clay and the aft by glacial clay;
- under the ship hull the soft soil is compressed several meters increasing the force response from the clay;
- the ship experiences extensive structural damage due to the bottom contact, even when descending in a nearly statical manner;
- structural damage is caused both by the soft seabed and by the acoustic bedrock;
- most extensive structural damage occurs at the aft and at the midship region
- the location and the extent of the calculated side damage corresponds well to the location and extent of the reported damages;
- the reported visual damage has been formed on the edge of the extensive damage located under the wreck (above the fender line);
- the numerical simulations propose a highly probable scenario of the side damages occurring as a result of the contact between the ship and the sea bottom.

It is acknowledged that there are several uncertainties involved with the presented assessment. It has been shown that the ship roll angle has a significant effect on the side damage and on the final position of the ship. With larger roll angle (133 deg) a significant portion of the deformation energy is absorbed by the crushing and folding of upper decks and less energy remains for the damage around the fender guard area. When the roll angle becomes smaller, the contact between the upper decks and soft soil is delayed and more energy is transferred through the contact between the rigid bottom and the ship, thus resulting in more localized and deeper deformation damage.

In the simulations, the ship aft remains higher compared to the current position of the wreck. This indicates that the response of the soft soil might be too hard to allow the ship to achieve the position closer to the current position of the wreckage. On the other hand, lower position would mean heavier structural damages at the midship region. Thus, it is expected, even though not yet fully assessed, that the stiffness of the soft soil will influence the deformation pattern on the ship hull.

At the sea bottom the ship remains under relatively high stresses, where the global stresses in the hull reach up to 150 MPa. Thus, the structural deformations and fractures could further propagate due to material creep.

Considering above, there are number of potential combinations of ship roll angles, positions, soil properties etc to be studied to refine the simulation models and to study the sensitivity of input parameters.

10. **ACKNOWLEDGEMENT**

This work has been conducted as a part of investigation by Estonian Safety Investigation Bureau (contract no 1.9-8/22-457-1).

11. **REFERENCES**

Bakroon, M. *et al.* (2018) 'Multi-material arbitrary Lagrangian-Eulerian and coupled Eulerian-Lagrangian methods for large deformation geotechnical problems', *Numerical Methods in Geotechnical Engineering IX* [Preprint]. Available at: https://api.semanticscholar.org/CorpusID:197569407.

DNV (2020) 'DNVGL-CG-0127, Finite element analysis, 2020 Edition, November 2020'.

DNV (2021) *DNV-RP-C208, Determination of structural capacity by non-linear finite element analysis methods, 2019 Edition, September 2021*.

Jakobsson, M. *et al.* (2021) *EL21-Estonia : Report of the MS Estonia shipwreck site survey with RV Electra*.

Jakobsson, M. (2023) 'Bathymetry and sediment thickness at the MS Estonia shipwreck site'.

Jasinowski, A. and Vassalos, D. (2008) *Technical Summary of the Investigation on The Sinking Sequence of MV Estonia*. Available at: www.safety-at-sea.co.uk.

Kehren, F.-I. (2009) *The Sinking Sequence of MV Estonia*. Technische Universität Hamburg. Available at: https://doi.org/10.15480/882.485.

Krüger, S. (2007) *Research Study of Sinking Sequence of MV Estonia Mile Stone 1 (M1) 'Accident Scenario'*.

Krüger, S. (2008) *Research Study of Sinking Sequence of MV Estonia Work Package 7 (WP7-T7) 'Hydrostatic Analyses of the Later Phases of the Capsizing and the Sinking of MV ESTONIA'*.

Lehmann, E. *et al.* (2001) 'CALCULATION OF COLLISIONS WITH THE AIDE OF LINEAR FE MODELS', in.

Rudebeck, D. and Kennedy, H. (2021) 'The Vessel M / S Estonia Review of geotechnical investigations'.

Valanto, P. and Friesch, J. (2008) *Research Study on the Sinking Sequence and Evacuation of the MV Estonia-Final Report Client: VINNOVA*. Available at: www.hsva.de.

Wright, A. (2012) *Wright 2012 TYRE SOIL INTERACTION MODELLING WITHIN A VIRTUAL PROVING*. CRANFIELD UNIVERSITY. Available at: http://dspace.lib.cranfield.ac.uk/handle/1826/7904 (Accessed: 9 May 2023).

APPENDIX A: UNDRAINED SHEAR STRENGTH AND PRECONSOLIDATION PRESSURE OF SOFT SOIL

Currently, two geological measurements surveys have been conducted, where geotechnical parameters of the sediments are measured. In 1996 Delft Geotechnics collected sediment samples upper layers (from up to depth of 2.5 m) of the soil from 9 separate locations, eight of which were taken from the region with soft sediments (post-glacial clay) and one location (NMC-SA-9) were in stiff sediment area (glacial clay). The latest geological survey was conducted in 2021 by Stockholm University (Jakobsson *et al.*, 2021). Three core samples were taken from the wreckage site, samples PC01 and PC03 (sample depths 205 cm and 234 cm) were taken from glacial clay region and PC02 (sample depth 472 cm) was taken from post-glacial clay region. Sample locations of both surveys are shown in Figure A-1.

(Jakobsson et al., 2021) concluded that in upper meter of the post glacial clay layer the undrained shear strength ranges between 0.6 and 3 kPa, increasing slightly below. In case of stiffer glacial clay, the undrained shear strength ranged from 4.5 to 16.9 kPa (up to 2.34 meters in depth).

(Rudebeck and Kennedy, 2021) studied the samples taken from Delft Geotechnics and proposed formulas to calculate undrained shear strength separately for post glacial clay and for glacial clay. For small depths, the strength values of both clays predicted by the formulas fall within the ranges presented by Jacobsson. However, for stiffer glacial clay the formulas give much smaller strength value than the range maximum given in Jacobsson, 2023 (compared values at depth 2.34 m are 4.9 kPa and 16.9 kPa). This discrepancy shows how different the soil properties could really be and how difficult it is to give accurate strength value. Taking into consideration that Delft measurements were conducted before sand was dumped at wreckage site and also that Delft measurements included much more sampling locations, it is decided to choose undrained strength values according to the formulas given by (Rudebeck and Kennedy, 2021).

Another important parameter to describe soil behaviour is preconsolidation pressure (*pc*) which influences the stiffness of the soils in compression. As this parameter was not covered in previous studies then by using Delft survey measurements and existing empirical formulas its value was estimated through correlation between the undrained shear strength (*cu*) and preconsolidation pressure (*pc*), see Figure A-2. It was proposed that at the surface sediments the preconsolidation pressure is between 2.2-4.5 kPa for postglacial clays and 10.1-18.3 kPa for glacial clays. At maximum depth (3 meters) of the Delft data the preconsolidation pressure is between 15-26 kPa for post glacial clay and 27-52 kPa for glacial clay.

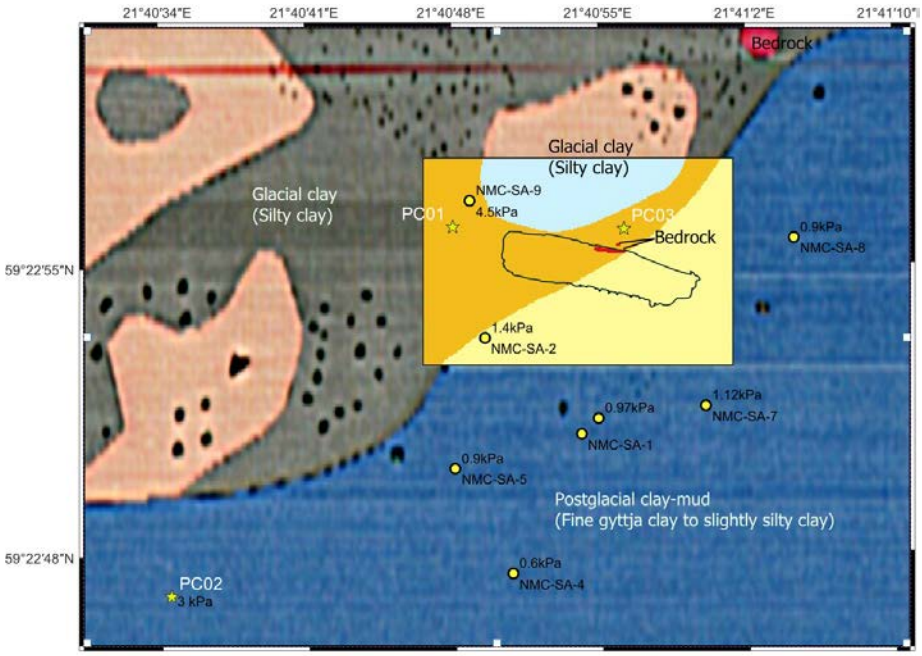

Figure A-1. Locations of the sampling/testing sites.

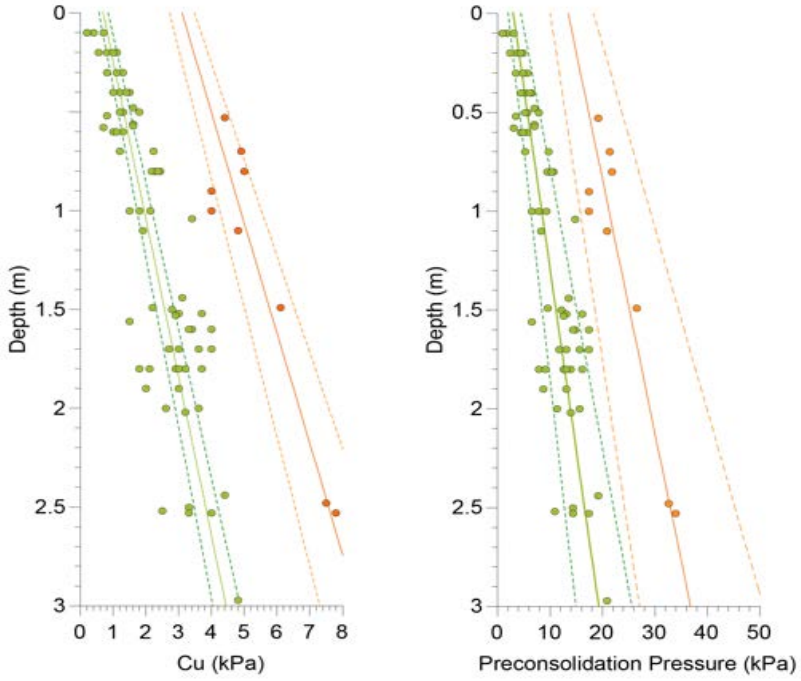

Figure A-2. Comparison of modelled (lines) and measured undrained shear strengths for postglacial (green) and glacial (orange) sediments. B. Calculated preconsolidation pressure from the laboratory/field measurements of shear strength (circles) and the regression models from A. (Input from Matthew O'Regan)